VISER
www.viserdata.com

RESEARCH AND APPLICATION OF MATERIALS SCIENCE

ISSN:2661-4464(online) 2661-4456(print)
Volume 3 No. 2 2021

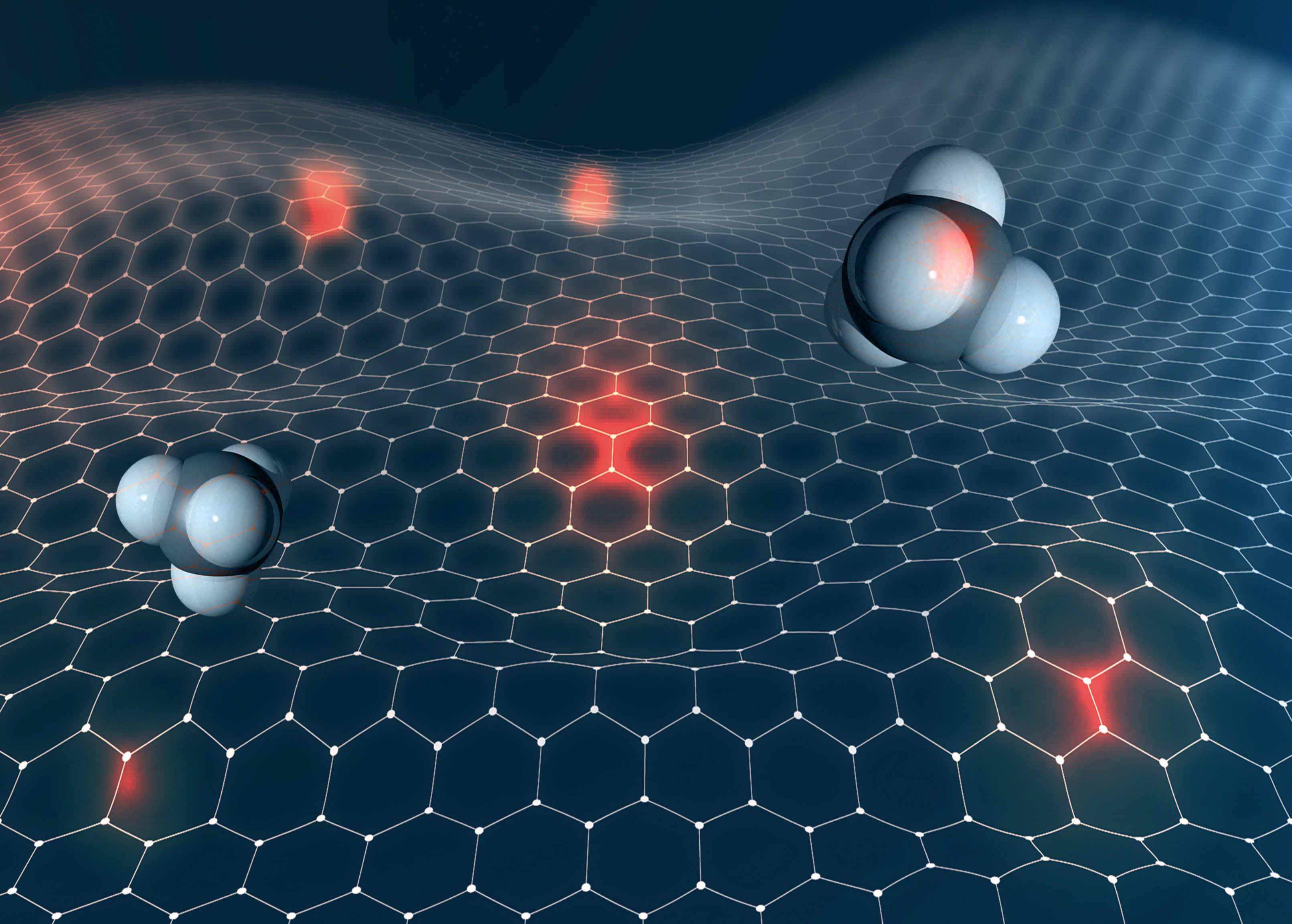

COMPANY INTRODUCTION

Viser Technology Pte. Ltd. was founded in Singapore with branch offices in both Hebei and Chongqing, China. Viser focuses on publishing scientific and technological journals and books that promote the exchange of scientific and technological findings among the research community and around the globe. Despite being a young company, Viser is actively connecting with well-known universities, research institutes, and indexation database, and has already established a stable collaborative relationship with them. We also have a group of experienced editors and publishing experts who are dedicated to publishing high-quality journal and book contents. We offer the scholars various academic journals covering a variety of subjects and we are committed to reducing the hassles of scholarly publishing. To achieve this goal, we provide scholars with an all-in-one platform that offers solutions to every publishing process that a scholar needs to go through in order to show their latest finding to the world.

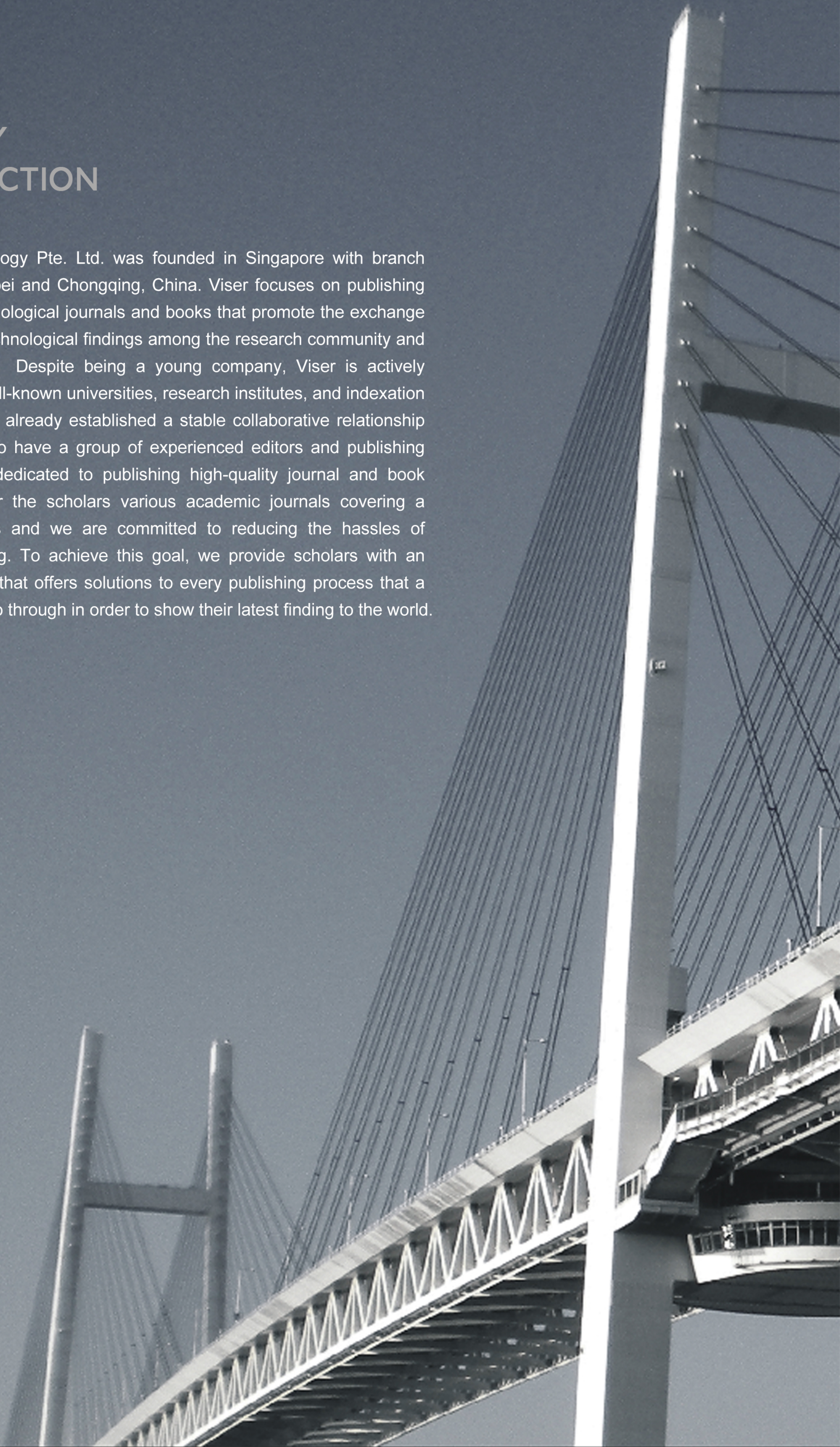

Research and Application of Materials Science

Publisher: Viser Technology Pte. Ltd.
ISSN: 2661-4464(online)
2661-4456(print)
Frequency: Semi-annual
Add.:21 Woodlands Close, #08-18
Primz Bizhub SINGAPORE (737854)
https://www.viserdata.com/

Editors:
Yajun Lian
John Wilson
Mart Chen
Debra Hamilton
Jennifer M Dohy
Edward Adam Davis
Yanli Liu
Nike Yough
Qiuyue Su
Xin Di
Xiuli Li
Liangjun Qiu
Designer: Anson Chee

Research and Application of Materials Science

Volume 3 No.2 (2021)

CONTENTS

Editor's message for the special issue on research on key materials in the development of electric vehicles

With the development of transportation energy power system, new energy vehicles will become the development direction of future vehicles under the pressure of energy and environmental protection. In recent years, scientists and researchers have made important contributions in the development of power batteries and lightweight key materials. The special issue of "Research and Application of Materials Science" on key materials in the development of new energy vehicles has deeply understood the research activities in this emerging field through six articles selected after strict review. Due to the large number of papers submitted and the limited space of a single journal, many high-quality papers cannot be accepted. The selected papers cover a wide range of research topics in this field, such as the properties of electrode materials for lithium-ion batteries and the mechanical properties and corrosion resistance of lightweight magnesium and aluminum alloys.

In terms of electrode materials, the paper "Toward high capacity and stable SnO_2 hollow nanosphere electrode materials: A case study of Ni-substituted modification" by Zhang et al afforded a new and facile strategy via Ni doping and the fabrication of hollow nanosphere enhancing the cyclic stability of SnO_2-based negative materials. The paper "An Effective Way to Prepare Submicron MoO_2 Anodes for High-Stability Lithium-Ion Batteries" by Li et al. prepared the novel MoO_2 submicrons wrapped in carbonouse layer with an attractive lithium storage ability, the outstanding capacity retention ratio and stability as well as rate capability compared to the commercial pure MoO_2. More interestingly, Qin et al. reported a Si@void@NC nanocomposite with a tunable nitrogen content in the carbon layer, where the capacity fading is inhibited with a suitable nitrogen addition in their paper "Preparation and electrochemical performance of Si@void@NC composite with a tunable nitrogen doping content in the carbon layer".

In the field of lightweight structure materials, the paper "Role of heat treatment temperatures on mechanical properties and corrosion resistance properties of Mg-10.16Li-8.14Al-1.46Er alloy" by Zou et al. reported the comprehensive tensile properties of Mg-10.16Li-8.14Al-1.46Er alloy under different conditions, where the best property achieved after heat treatment at 400℃ attributed to solution strengthening and second phase strengthening. To address the issue on the easy oxidation of Mg and its alloys, the paper "Oxidation resistance of magnesium alloyed by different elements: a brief review" by Liu et al. briefly reviewed the effects of alloying elements (Al, Zn, Ca, Sr, La, Ce, Nd, Y, Gd and Er) on the oxidation resistance of Mg and Mg alloys and provide some measures to improve this shortcoming by tailoring the alloying elements and the suitable fabrication parameters. Besides these, He et al. studied the influence of Mn and Mg contents on mechanical properties of the die-casting HL-111 Al alloy through the different thickness plates under heat treatments in their paper "Influence of Mn and Mg contents on mechanical properties of the die-casting aluminum alloy HL-111".

Yongfu Zhu, professor in Jilin University. He got his bachelor degree from Jilin University in July 1995, and master degree from Changchun Institute of Optics, Fine Mechanics and Physics in Sept. 1999. In Oct. 1999, he began his PhD study in Tohoku University in Japan and was entitled the PhD degree in Feb. 2003. From March 2003 to Feb. 2006, he pursued his postdoc research in Hongkong Polytechnic University, Akita University and Tohoku University. In March 2006, he began to work as a full-time staff in Jilin University based on the talent plan of Jilin University. He is mainly engaged in the research of energy materials and metal oxidation and protection. He has published nearly 90 SCI papers, and some research results have been published in high impact journals, such as Coordination Chemistry Reviews, ACS Nano, Adv. Funct. Mater., J. Phys. Chem. C, Appl. Phys. Lett., and so on.

Ting Zhu graduated with a BSc in Materials Chemistry (2007) and MSc in Biomedical Engineering (2010) from Sichuan University (Chengdu, China). He obtained his PhD degree in Nanyang Technological University (Singapore) in 2014. Upon completion of PhD, he worked as a postdoctoral researcher in National University of Singapore till 2017. He then joined Central South University (Changsha, China) in 2017 to 2021 as a professor. Since December of 2021, he transferred to Yunnan Normal University (Kunming, China) as a full-time research professor. His research interests focus on the development of nanostructured functional materials for energy storage and conversion, such as lithium/sodium ion batteries, supercapacitors, and photo/electro-catalysis. So far, he has authored over 60 research papers in international journals including Adv. Energy Mater., InfoMat, Nano Energy, Small, Solar RRL., J. Mater. Chem. A and so on with a total citation over 5000 times and an H-index of 31.

About the author

Hong Guo is a Professor at Yunnan Key Laboratory of Micro/Nano Materials and Technology, School of Materials Science and Engineering, Yunnan University, China. He received his Ph.D. from University of Science & Technology Beijing in 2008. His research interests are focused on advanced materials for electrochemical energy storage and conversion, including electrode and solid-state electrolyte materials for sodium-ion battery.

Yanyang He worked as an engineer in Ningbo Heli Mold Technology Co., Ltd. from 1998 to 2009 after obtaining bachelor's degree, mainly engaged in mold design and production. Then from 2009 to 2022, he worked in Ningbo Heli Technology Co., Ltd. as the general manager of the business division, mainly engaged in the research and development of automotive parts manufacturing and applied aluminum alloy. Mr. He has unique insights and rich working experience in the development and design of new aluminum alloys.

Haizhu Sun (1977.12—) Female, Place of Birth: Changchun, Prof. Dr.Haizhu Sun currently is a professor of the College of Chemistry at Northeast Normal University. She received her PhD in Polymer Chemistry and Physics in 2008 at Jilin University. Her research interests are related with design, synthesis, and properties of new energy materials that can find appications in photo-electric conversion, energy storate and photocatalysis, etc. She has coauthored over 150 papers published with H-index 23.

About the author

Guojun Liu received the Ph.D. degree in materials science and engineering from Jilin University, Changchun, China. He is currently a Senior Engineer with the School of Materials Science and Engineering, Jilin University. His main field of research is magnesium alloys with high strength, toughness, and excellent oxidation resistance. His research interests also involve metallic material, corrosion, as well as friction and wear of materials.

Yun Zou (1989—) obtained a doctor degree of engineering at Harbin Engineering University in 2016. Currently, she is an associate professor and master supervisor of School of Mechanical and Power Engineering, Zhengzhou University, China. At present, she has presided about 5 projects including the National Natural Science Foundation projects of China, Key Research Project of the Higher Education Institutions of Henan Province, and Special Research and Promotion Project of Henan Province, China, etc. Her research focuses on deformation mechanisms and mechanical properties of magnesium alloys, deformation mechanisms and strengthening and toughening mechanisms of gradient nanostructured materials, and corrosion and protection of magnesium alloys, etc. Moreover, she published about 30 papers, including 20 in SCI and EI.

Guodong Jiang obtained his Ph.D. degree in 2011 from Huazhong University of Science & Technology. He is currently an associate professor in School of Material and Chemical Engineering at Hubei University of Technology. His research interest focuses on high performance energy materials for lithium ion batteries and various energy storage systems.

Viser Technology Pte. Ltd.
Research and Application of Materials Science
DOI: 10.33142/rams.v3i2.6729

Research Article Open Access

Toward High Capacity and Stable SnO_2 Hollow Nanosphere Electrode Materials: A Case Study of Ni-substituted Modification

Yannan ZHANG [1], Peng DONG [1], Yingjie ZHANG [1], Hong GUO [2*]

1 National and Local Joint Engineering Laboratory for Lithium-ion Batteries and Materials Preparation Technology, Yunnan Provincial Laboratory for Advanced Materials and Batteries Application, Faculty of Metallurgical and Energy Engineering, Kunming University of Science and Technology, Kunming 650093, Yunnan, PR China
2 School of Materials and Energy, Yunnan Key Laboratory for Micro/Nano Materials and Technology, Yunnan University, Kunming 650091, China

***Corresponding Author:** Hong GUO, No. 2, Green Lake North Road, Kunming 650091, China; guohong@ynu.edu.cn (H. Guo)*

Abstract:
To develop the urgent requirement for high-rate electrodes in next-generation lithium-ion batteries, SnO_2-based negative materials have been spotlighted as potential alternatives. However, the intrinsic problems, such as conspicuous volume variation and unremarkable conductivity, make the rate capability behave badly at a high-current density. Here, to solve these issues, this work demonstrate a new and facile strategy for synergistically enhancing their cyclic stability by combining the advantages of Ni doping and the fabrication of hollow nanosphere. Specifically, the incorporation of Ni^{2+} ions into the tetragonal rutile-type SnO_2 shells improves the charge transfer kinetics effectively, leading to an excellent cycling stability. In addition, the growth of surface grains on the hollow nanospheres are restrained after Ni doping, which also reduces the unexpected polarization of negative electrodes. As a result, the as-prepared Ni doped electrode delivers a remarkable reversible capacity of 712 mAh g^{-1} at 0.1 A g^{-1} and exhibits outstanding capacity of 340 mAh g^{-1} at 1.6 A g^{-1}, about 2.58 times higher than that of the pure SnO_2 hollow sample.

Keywords: *Tin oxide; Negative materials; Nickel doping; Hollow nanospheres; Lithium ion batteries*

1 Introduction

Lithium-ion batteries (LIBs) have attracted considerable attention as wide applications in smart grids devices, portable devices and hybrid electric vehicles [1-3]. However, the commercial graphite negative electrodes used at present exhibit a poor theoretical specific capacity (372 mA h g^{-1}) and limited rate capability [4-6]. Therefore, it is important to explore other negative electrodes with high mass energy density. As promising negative electrode candidate for contemporary LIBs, tin dioxide (SnO_2) has attracted huge amount of interest because of its remarkable theoretical capacity (1492 mAh g^{-1}), nontoxicity, abundant tin resource, and favorable processability. Unfortunately, the SnO_2 based LIBs are restricted by huge volume expansion (approximately 240%) during lithiation/delithiation process, leading to agglomeration, structure collapse and finally electrochemical inactivation for the active material [7-10]. In addition, the low electrical conductivity also limits the extensive commercial application of the tin-based LIBs [11-13].

In order to overcome the poor durability and enhance the long-term cycling stability, SnO_2-based materials with special nanostructures are designed and synthesized, such as core-shell particles[14-15], nanotubes[16-20], and nanosheets [21-23]. Among them, porous hollow nanospheres have attracted much attention since they can provide much more cushion space during the lithiation/delithiation process and deliver better cycling stability than other nanostructured materials [24-27].

The electrochemical performance of SnO_2 hollow nanospheres could be further enhanced by elevating their electrical conductivity. One of the most commonly reported strategies is to combine the nano-scaled SnO_2 with conductive carbonaceous materials [28-30]. Another effective approach is to enhance the intrinsic conductivity through introducing transition metal dopant into the SnO_2 structure, the substitution of Sn by cations, such as Sb^{5+}, Co^{3+}, $Fe^{3+}$and Mo^{6+}can also stabilize the structure of SnO_2 and restrain the tremendous initial capacity loss [31-33]. Ma et al. prepared Co-doped nanoparticles, which exhibited a favorable specific capacity of 493 mAh g^{-1} under 100 mA g^{-1} after 50 cycles, almost the 2 times than the undoped one [34]. Zhao et al. synthesized Pd-doped graphene SnO_2

Received on October 15, 2021; Accepted on December 6, 2021

nanocomposite through electroless plating method, the as-prepared SnO_2 nanoparticles delivered high reversible capacity and promising rate capability [35].

Hence, the doping cations properties play an important role in determining the comprehensive performance of the SnO_2, especially for processes of nanostructure, grain growth and internal Li-ion transport in the tetragonal rutile structure. Understanding these effects is important. To the best of our knowledge, Ni^{2+} and Sn^{4+} have the same radius (0.069 nm), Ni^{2+} ions are easily introduced into the SnO_2 lattice. Herein, by combining the strengths of hollow nanostructure and doping element, we report a comparative investigation of pure SnO_2 hollow nanospheres and a series of Ni-doped SnO_2 (NTO) with different dopant contents, focusing on the influence of the dopant concentration on the nanostructure, surface chemical properties as well as electrochemical performance. The results reveal that the Ni^{2+} dopant ratio not only affects the surface chemical properties, but moreover also plays an important role on the electrochemical performance.

2 Experimental

2.1 Material Synthesis

The Ni-doped SnO_2 (NTO) hollow spheres were prepared by following a combined template process and sol-gel process: (1) SiO_2 nanospheres were synthesized by the well-known Stöber method, which was reported in our previous work [36]. (2) 3 g $SnCl_2 \cdot 2H_2O$ was added into a flat bottom boiling flask and then heated to 80℃, after that, the obtained molten $SnCl_2$ and 2 g SiO_2 nanospheres (prepared in the previous step) were dispersed in 200 mL deionized water by ultrasound for 50 min, and the resulting gel was continuously stirred for 36 h at 80℃. (3) Subsequently, several groups with different proportions of $NiSO_4$ were added into the mixture, the Sn: Ni molar ratio used is 40:0, 40:1, 40:2, and 40:3, respectively. (4) Then, the resulting gel was continuously stirred for 36 h at 80℃ to enable the infiltration of tin precursor into the pores of the SiO_2 nanospheres. (5) Ultimately, the four collected products were calcinated at 500℃ for 6 h under an nitrogen flow, and then etched by an HF solution (10%, 100 mL), the four group of Ni-doped SnO_2 (NTO) samples with different dopant contents were obtained (denoted as NTO-0, NTO-1, NTO-2, and NTO-3). The flowchart for the preparation of NTO hollow nanospheres is shown in Figure 1.

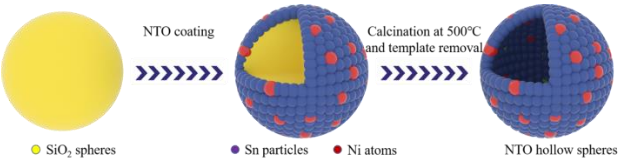

Figure 1 Flowchart for the preparation of nickel doped SnO_2 hollow nanospheres (NTO)

2.2 Material Characterization and electrochemical measurements

The crystalline structure of the as-prepared NTO-x (x=0, 1, 2, and 3) hollow nanospheres were accomplished by X-ray diffraction (XRD, Rint-2000, Japan) using Cu-Kα radiation (1.5412 Å). The surface morphologies and the samples were observed through a field emission scanning electron microscopy (FESEM, Zeiss Supra 55VP), and the elemental distribution was recorded with an energy-dispersive X-ray spectroscopy (EDS, PHI5000 Versa probe-II). The determination of surface elements of the as-prepared powers was carried out by an X-ray photoelectron spectroscopy (XPS, PHI5000 Versaprobe-II). The crystalline microstructures of the obtained powers were further confirmed by the transmission electron microscopy (TEM, FEI Tecnai F20). The electrochemical properties of the as-prepared four samples were further evaluated using CR2025-type coin cells with a multi-channel current static system (LAND CT2001D, China). In addition, the cyclic voltammetry (CV) and the electrochemical impedance spectroscopy (EIS) results of the electrodes were recorded on an electrochemical workstation (PGSTAT302N, Switzerland). The button battery assembly process and the detailed electrochemical analysis procedures were performed according to our previous report [37-38].

3 Results and Discussion

Figure 2a plots the XRD patterns of the four different nickel doped as-prepared NTO samples. Noticeably, All of the NTO samples are well crystallized. The diffraction peaks of four samples can be identified as tetragonal rutile SnO_2 (JCPDS card No. 41-1445) [39-40], and no obvious other impurities are detected, revealing that the Ni^{2+} are favorably integrated with the surface of the SnO_2 shells, and may diffuse only a few nanometers into the tetragonal rutile structure during high temperature post calcination. The magnified diffraction peaks of (110) are exhibited in Figure 2b, it can be clearly observed that the position shifts to a positive degree and the diffraction peaks of (110) deliver a wider half-peak width after Ni-doping. According to Scherer's formula, the thickness of single grain (d) is inversely proportional to half of peak width (B), which reveals that the average lattice parameter is decreased after Ni-doping. The initial particle size of NTO-1、NTO-2、NTO-3 are 9.3 nm 8.6 nm，7.5 nm，and 7.1 nm respectively. This is because even though Ni^{2+} and Sn^{4+} have the same radius (0.069 nm), the incorporation of Ni^{2+} into the lattice of SnO_2 will produce some new defects such as dislocations and vacancies, and the vacancy formation energy and the surface energy of SnO_2 nano-particles are also increased, which can effectively restrain the growth of the crystal to some extent. This phenomenon is further confirmed by the TEM images and in very good agreement with the previous studies on Fe/Zn/Co-doped tin oxide[41-44].

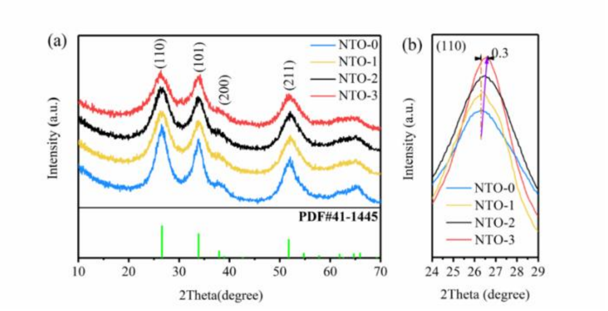

Figure 2 XRD patterns of NTO powder samples (a) and the enlarged (110) peaks (b)

The chemical compositions of the as-prepared hollow nanospheres were further explored by XPS analysis. The full-scan spectra of NTO-0 and NTO-2 samples are exhibited in Figure 2a. Compared with the NTO-0, besides the Sn 3d, O 1s, and C 1s peaks, a couple of weak peaks of Sn 2p can be observed in the spectra of NTO-2 sample. Figure 3b plots the Sn3d spectra of sample NTO-0 and sample NTO-2. The two remarkable shake-up peaks located at 485.6 and 494.4 eV can be assigned to Sn $3d_{5/2}$ and Sn $3d_{3/2}$ levels, respectively[45-46]. A positive shift with approximately 0.4 eV in the sample of NTO-2 indicates the multi-electrons may have transferred from Sn to the doped Ni. Furthermore, the Ni 2p spectra of NTO-2 is illustrated in Figure 3c. Two characteristic peaks at approximately 854.8 eV and 873.2 eV are attribute to Ni $2p_{3/2}$ and Ni $2p_{1/2}$ levels, and two shake-up satellites are located at 861.8 eV and 880.1 eV, respectively, which are attribute to the multi-electron transitions. The binding energy between these characteristic peaks is approximately 18.4 eV. The results show that the nickel element doped into the crystal lattice of SnO_2 exists in the form of Ni^{2+} ions [47-48].

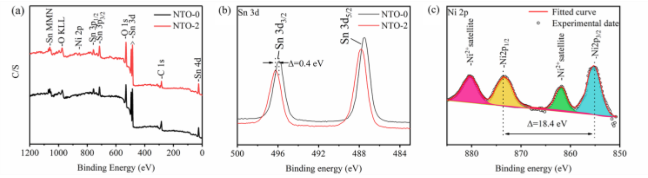

Figure 3 XPS spectra of NTO-0 and NTO-2 sample: (a) Survey spectrum, (b) Sn 3d5/2, (c) Ni 2p

The morphology and particle size of as-synthesized SiO_2 nanoparticles was investigated by scanning electron microscopy (SEM). As shown in Figure 4a. The obtained SiO_2 exhibits a regular spherical structure with an average diameter of 500-580 nm. Figure 4b displays the SEM images of NTO samples with different Ni doping content, and the magnified image of NTO-2 sample is displayed in Figure 4c, clearly revealing that the presence of a hollow structure for the as-prepared materials. The diameter of SnO_2 spheres with different doping content possess similar values of approximately 550 nm, which in consistent with the size of nano SiO_2 templates. The elemental distribution of the as-prepared NTO-2 sample was further detected by EDS test (Figure 4d). The uniform distributions of Sn, O, and Ni elements over the whole hollow spheres indicates that the Ni is homogeneously and continuously coupled with the SnO_2 shells.

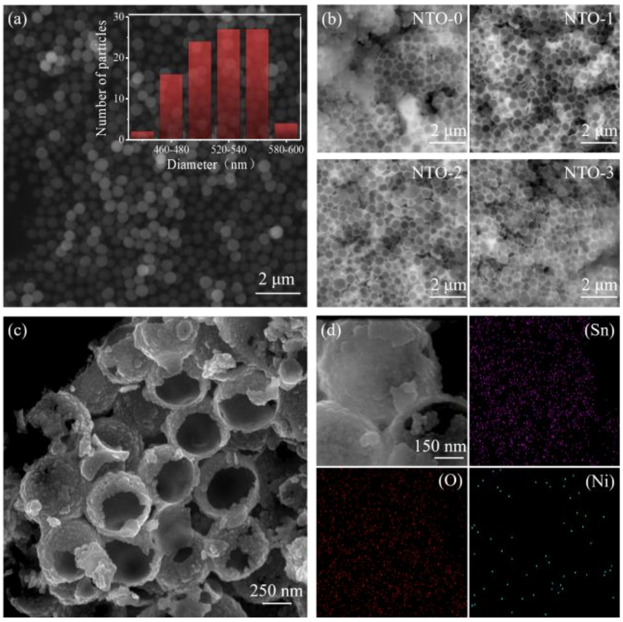

Figure 4 SEM images of (a) SiO_2 nanoparticles; (b) SEM image of NTO samples with different Ni doping content; (c) magnified image of NTO-2;(d) EDS mapping images of NTO-2

TEM images of as-prepared products are displayed in Figure 5. The spherical morphology of SiO_2 exhibits regular and clear surface profiles, as shown in Figure 5a. The TEM images in Figure 5 (b-f) were captured to further confirm that the as-synthesized SnO_2 samples exhibit hollow nanosphere structures. It can be clearly seen that spherical morphology of $SnO_2@SiO_2$ can be well maintained after etching of the SiO_2 exhibits a shell thickness of approximately 42 nm (Figure 5b). However, after Ni doping, the shell thickness of the NTO-2 sample is decreased to approximately 28 nm through the same process (Figure 5c). Furthermore, Figure 5d-e clearly exhibit the high-resolution TEM (HRTEM) images of the lattice fringes and particle size of the two samples. The grain diameters of NTO-0 and NTO-2 are approximately 5-7 nm and 8-9 nm, respectively, which coincides well with the previous XRD calculation results. This is because the crystallization and ripening process of the SnO_2 primary particle particles may be effectively restrained by the sequential accumulation of Ni^{2+}, which is similar to the process of the crystal surface energy model. The selected-area electron diffraction (SAED) pattern of NTO-2 with the diffraction rings from inside to outside can be indexed to (110), (101), (200), (211), and (311) of tetragonal rutile SnO_2, as illustrated in Figure 5f [49]. This result reveals that expect for the suppression of the particles growth, the Ni doping does not cause any changes in the tetragonal rutile structure of SnO_2.

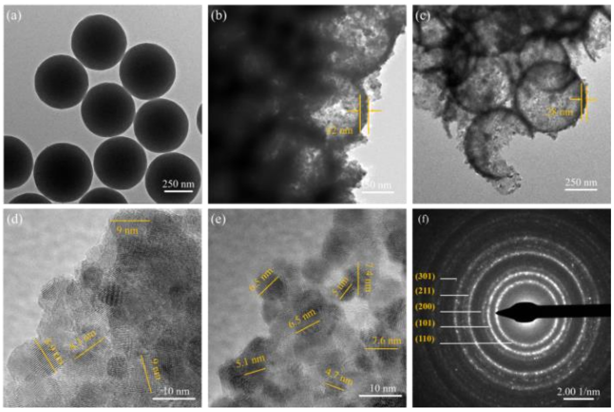

Figure 5 TEM images (a) SiO_2 nanoparticles, (b) NTO-0, and (c) NTO-2, respectively；high-resolution TEM image of (d) NTO-0, and (e) NTO-0;(d) the selected-area electron diffraction (SAED) pattern of NTO-2 sample

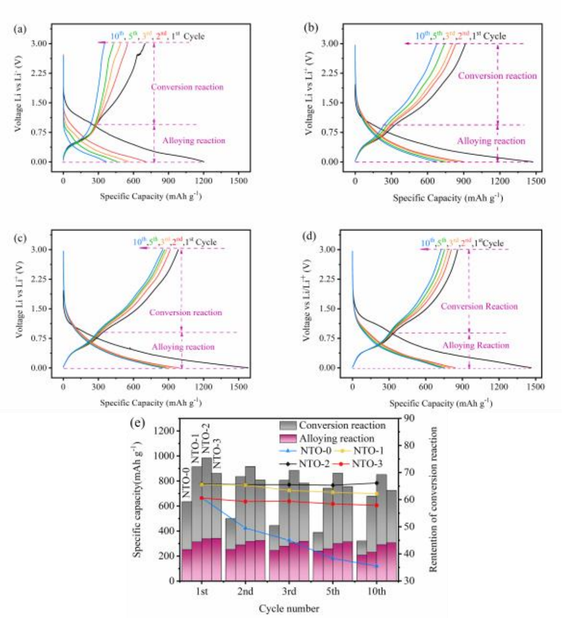

Figure 6 The charge-discharge test curves of the NTO negative electrodes: (a) NTO-0; (b) NTO-1; (c) NTO-2;(d) NTO-3; (e) the relationship between capacity retention for the conversion reaction and the total specific charge capacities of all the samples

Figure 6a-d display the charge-discharge curves of the prepared four NTO samples at a current density of 100 mA g^{-1} between 0.01 V and 3.0 V. The initial discharge and charge-specific capacities of the NTO-0, NTO-1, NTO-2, and NTO-3 samples are1203 mAh g^{-1}、1470 mAh g^{-1}、1581 mAh g^{-1}, and 1463 mAh g^{-1}, and the initial coulombic efficiency of these sample are 61.6%，62.0%，62.5%, and 58.8%, respectively. All the samples suffer serious capacity losses in the early cycles, which is attribute mainly to the SEI film formation and the production of Li_2O [35]. NTO-2 exhibits the best charge-specific capacity of 850 mAh g^{-1} after 10th cycles even with a rather moderate initial coulombic efficiency, which is almost twice of the undoped NTO-0 sample (466 mAh g^{-1}). Figure 6e shows the relationship between capacity retention for conversion reaction and the total specific charge capacities of the four samples. It can be clearly seen that the capacity ratio of the conversion reaction of Ni doped samples are significantly higher than that of the undoped one. After the 10th cycles, the capacity ratio of conversion reaction for the NTO-0 sample is only 35.5%, while the capacity ratio of the NTO-2 is increased up to 66.1%. Thus, we conclude that the Ni doping could facilitate the conversion reaction between Sn and Li_2O, which results in the remarkable conversion reaction capacity [50].

$$SnO_2 + 4Li^+ + 4e^- \rightarrow Sn + 2Li_2O \quad \text{(Conversion reaction)}$$

$$Sn + yLi^+ + ye^- \leftrightarrow Li_ySn(0 \le y \le 4.4) \quad \text{(Alloying reaction)}$$

To evaluate the cycling performance of NTO hollow sphere with different Ni doping content, a range of cyclic tests were carried out at the current density of 100 mA g^{-1} in the voltage range of 0.01-3.0V, as presented in Figure 7a. After 100 cycles, the capacity of the NTO-0 decays rapidly to 236 mAh g^{-1} with a deteriorating capacity retention of 32.0%, whereas the NTO can still maintain promising capacity retention of 73.1% (712 mAh g^{-1}) with a nearly perfect coulombic efficiency (approximately 100%), except during the first cycle. In addition, the NTO-1 and NTO-3 also can deliver the moderate charge capacity of 485 and 653 mAh g^{-1}. Based on these results, we conclude that the electrochemical performance of the SnO_2 nano hollow spheres are improved by the Ni doping.

Furthermore, the rate capabilities of these four samples were also investigated by applying different specific currents, i.e., 0.05, 0.1, 0.2, 0.4, 0.8, and 1.6 A g^{-1}, as shown in Figure 7b. As increasing the current density, compared with the sample NTO-0, all of the samples deliver significantly improved charge capacities after doping under each current density (0.05-1.6 A g^{-1}). Notably, sample NTO-2 exhibits the best rate performance, its charge capacity can remain up to 340 mAh g^{-1}even at 1.6 A g^{-1} current density, and exhibit a promising charge capacity of 651 mAh g^{-1} when the current density is recovered to 0.1 Ag^{-1}, whereas the pristine sample NTO-0 deliver the limited rate performance. The results of the cyclic and rate performances are consistent with our previous corresponding charge and discharge profiles.

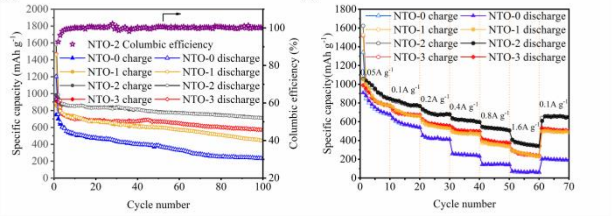

Figure 7 (a) Cycling performance of NTO samples at a current density of 100 mA g^{-1}; (b) rate performance of NTO samples.

For better understanding the kinetic process of lithium insertion/extraction into/from the 3D Ni doped SnO_2 hollow spheres, cyclic voltammetry (CV) tests between 0.01-3.0 V at different scanning rates (0.1-0.8 mV s^{-1}) were performed for the samples NTO-0 and NTO-2. Two characteristic pairs of redox peaks can be clearly observed in Figure 8a. The first pair located at 0.10 and 0.82 V (*a* site) are ascribed to the of Li_xSn ($0 < x < 4.4$) alloying and de-alloying process. The second dominant anodic peak located at 1.58 V (*c* site) is related to the partial conversion of Sn to Sn^{4+}, while the cathodic peak observed at 1.13 V is attributed to the irreversible formation of a SEI film and the reduction reaction of SnO_2 by Li. NTO-0 exhibits a large peak shift and obvious polarization at different scanning rates.

For the sample of NTO-2, the shape of the CV profiles (Figure 8b) is similar to that of the NTO-0 sample. It is worthy to note that the initial anodic peaks shift to 0.8 and 1.54 V, respectively. The redox potential difference related to the Li_xSn alloying/de-alloying process is lower than that of the undoped one. Moreover, the peak displacement of sample NTO-2 is decreased, and the cyclic voltammetry profiles remain unchanged as the increase of the scanning rate, revealing the reduced polarization and improved reversibility.

The Li^+ diffusion coefficient change of electrodes can be obtained from Randles-Sevcik equation (1):

$$I_p = 2.69 \times 10^5 n^{3/2} A D^{1/2} v^{1/2} C_0 \qquad (1)$$

in which D, I_p, n, A, v , and C_0 represents the diffusion coefficient of Li^+, the oxidation peak current (*a* and *c* site in Figure 9a-b), the amount of electrons transferred per SnO_2 molecule in the electrochemical reaction, the area of the electrode, scanning rate, and the concentration of Li^+. Since the area, charge transfer number, and the Li^+ concentration of the two samples are approximately identical, the ratio of the Li^+ diffusion coefficient between the two sample is proportional to the value of $(I_p/v^{1/2})^2$, as shown in Figure 8c. Consequently, the D_{NTO-2}/D_{NTO-0} at *a* and *c* site are 1.31 and 1.33, respectively, indicating that Ni^{2+}doping can effectively enhance the Li^+ diffusion.

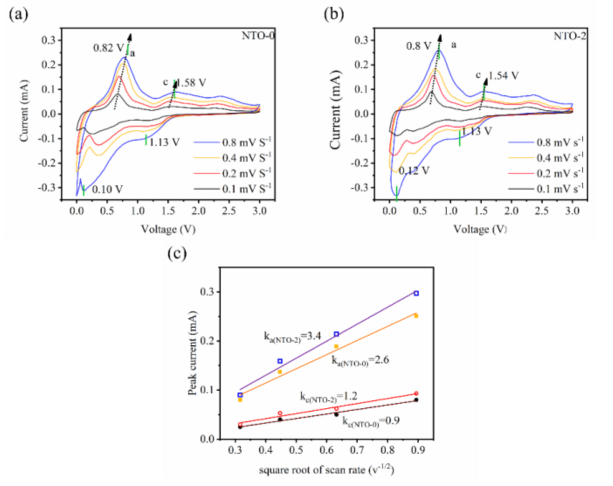

Figure 8 Cyclic voltammograms curves of NTO-0 (a), NTO-2 (b) at different scanning rates; (c) anodic peak against root of scan rate for NTO-0 and NTO-2

To further explore the beneficial effect of Ni doping on the electrochemical properties, electrochemical impedance spectroscopy (EIS) measurements were conducted to analyze the reaction dynamics. The Nyquist plots of four NTO samples after 5 cycles are shown in Figure 9. The semicircles in the high and high-middle frequency regions represent the solid electrolyte interface (SEI) resistance (Rf) and the charge transfer resistance (R_{ct}), whereas the inclined line in the low-frequency region corresponds to the Warburg impedance (Z_w) [51-52]. The diameter of the semicircle corresponding to the three doped sample are obviously smaller than that of the pristine one. Notably, the calculated he SEI resistance (R_f) of NTO-2 is 5.1Ω, which is lower than that of the NTO-0 (7.2 Ω), revealing that Ni doping can alleviate the thickness increase of the solid electrolyte interface membrane. The charge-transfer resistance (R_{ct}) of NTO-2 is simulated as 51.2 Ω, which is obviously lower than that of the NTO-0 (129.5Ω), indicating the charge transfer efficiency of SnO_2 hollow spheres is significantly improved. The favorable reversible specific capacity, enhanced cycling stability and remarkable rate capability of the NTO-2 sample could be attributed to the following two factors:(1) A certain amount of Ni^{2+}incorporates with SnO_2 can not change the integrity of the original tetragonal rutile structure but change the kinetics of SnO_2 negative materials, the charge transfer impedance is significantly decreased, resulting in the accelerated charge transfer kinetics. (2) The crystallization and ripening process of the primary particles is restrained by the Ni doping, and the shell thickness is also reduced, which effectively facilitate the Li^+ diffusion and internal electron transport in the active materials.

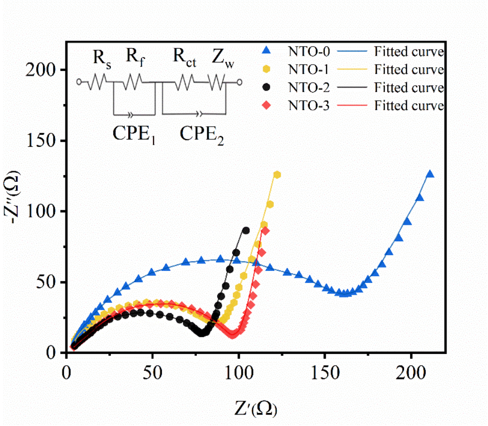

Figure 9 The Nyquist plots of the NTO samples

4 Conclusion

In summary, the SnO_2 hollow nanospheres with three different nickel dopant ratios were successfully synthesized through combined the template with the hydrothermal strategies and applied in LIBs as a negative material. XPS profiling with EDS mapping results reveal that the nickel dopant is uniformly distributed and well incorporated into SnO_2 shells among the hollow materials. The dopant concentration does not only have an influence on the on the surface chemistry property, but moreover on the electrochemical performance. Electrochemical measurement results indicate that the electrodes doped with 5% (wt%) can deliver an outstanding rate performance and excellent cycling performance (exhibit a favourable reversible capacity of 712 mAh g^{-1} at 100 mA g^{-1} after 100 cycles and deliver 340 mAh g^{-1} at 1.6 A g^{-1}). Without carbon coating, this hollow structural fabrication combined with rational dopant ratios will illuminate the path for developing other negative materials for solving the problems of low rate capability and poor cyclic stability.

Acknowledgements: The authors acknowledge financial support provided by the National Natural Science Foundation of China (Grant No: 52164031), and Yunnan Natural Science Foundation (No: 202101AT070449, 202101AU070048).

References

[1] Ma D, Li Y, Mi H, et al., Robust SnO_{2-x} nanoparticle-impregnated carbon nanofibers with outstanding electrochemical performance for advanced sodium-ion batteries, Angew. Chem. Int. Ed. 57 (2018): 8901-8905.

[2] Tan L, Feng S.H, Li X H, et al., Oxygen-induced lithiophilicity of tin-based framework toward highly stable lithium metal anode. Chem. Eng. J. 394 (2020): 124848.

[3] N. Mahmood, Tang T Y, Hou Y L. Nanostructured anode materials for lithium ion batteries: progress, challenge and perspective, Adv. Energy Mater. 6 (2016): 1600374.

[4] Wang L, Y. Leconte, Feng Z, et al., Novel preparation of N-doped SnO_2 nanoparticles via laser-assisted pyrolysis: demonstration of exceptional lithium storage properties. Adv. Mater. 29 (2017): 1603286

[5] V.M.H. Ng, Wu S Y , Liu P J, et al., Hierarchical SnO_2-graphite nanocomposite anode for lithium-ion batteries through high energy mechanical activation, Electrochim. Acta 248 (2017): 440-448.

[6] Zhang F, Yang C K, Gao X, et al., SnO_2@PANI core – shell nanorod arrays on 3D graphite foam: a high-performance integrated electrode for lithium-ion batteries, ACS Appl. Mater. Interfaces 9 (2017): 9620-9629.

[7] Tian Q, Zhang F, Yang L. Fabricating thin two-dimensional hollow tin dioxide/carbon nanocomposite for high-performance lithium-ion battery anode. Appl. Surf. Sci. 481 (2019): 1377-1384.

[8] Shi S.J, Deng T T, Zhang M, et al., Fast facile synthesis of SnO_2/graphene composite assisted by microwave as anode material for lithium-ion batteries, Electrochim. Acta 246 (2017): 1104-1111.

[9] Zhang L, Jiang L, Yan H, et al., Mono dispersed SnO_2 nanoparticles on both sides of single layer graphene sheets as anode materials in Li-ion batteries. J. Mater. Chem. 20 (2010): 5462-5467.

[10] Lou X, Deng D, Lee J, et al., Preparation of SnO_2/carbon composite hollow spheres and their lithium storage properties. Chem. Mater. 20 (2008): 6562-6566.

[11] Zhu Z, Wang S, Du J, et al., Ultrasmall Sn nanoparticles embedded in nitrogen-doped porous carbon as high-performance anode for lithium-ion batteries, Nano Lett. 14 (2014): 153-157.

[12] Yi L G, Liu L, Guo G X, et al., Expanded graphite@SnO_2@polyaniline composite with enhanced performance as anode materials for lithium ion batteries, Electrochim. Acta 240 (2017): 63-71.

[13] Hou C C, S. Brahma, Weng S C, et al., low temperature synthesis of SnO_2/reduced graphene oxide nanocomposite as anode material for lithium-ion batteries, Appl. Surf. Sci. 413 (2017): 160-168.

[14] Zhu Z, Wang S, Du J, et al., Ultrasmall Sn nanoparticles embedded in nitrogen-doped porous carbon as high-performance anode for lithium-ion batteries, Nano Lett. 14 (2014): 153-157.

[15] Hong Y, Mao W, Hu Q, et al., Ai, Nitrogen-doped carbon coated SnO2 nanoparticles embedded in a hierarchical porous carbon dramework for high-performance lithium-ion battery anodes, J. Power Sources 428 (2019): 44-52.

[16] Zhou X, Yu L, Lou X W D. Formation of uniform N-doped carbon-coated SnO_2 submicroboxes with enhanced lithium storage properties, Adv. Energy Mater. 6 (2016): 1066451.

[17] Zhang L, Wu H B, Liu B, et al., Formation of porous SnO_2 microboxes via selective leaching for highly reversible lithium storage, Energy Environ. Sci. 7 (2014): 1013-1017.

[18] Huang B, Li X, Pei Y, et al., Novel carbon-encapsulated porous SnO_2 anode for lithium-ion batteries with much improved cyclic stability, Small 12 (2016): 1945-1955.

[19] D. Kim, D. Lee, J. Kim, et al. Electrospun Ni-added SnO_2-carbon nanofiber composite anode for high-performance lithium-ion batteries, ACS Appl. Mater. Interfaces 4 (2012): 5408-5415.

[20] Li H Z, Yang L Y, Liu J, et al., Improved electrochemical performance of yolk-shell structured SnO_2@void@C porous nanowires as anode for lithium and sodium batteries, J. Power Sources 324 (2016): 780-787.

[21] Chang L, Yi Z, Wang Z, et al., Ultrathin SnO2 nanosheets anchored on graphene with improved electrochemical kinetics for reversible lithium and sodium storage, Appl. Surf. Sci. 484 (2019): 646-654.

[22] Ding S, Luan D, F Boey, SnO_2 nanosheets grown on graphene sheets with enhanced lithium storage properties, Chem. Commun. 47 (2011): 7155-7157.

[23] Wei W, Du P, Liu D, et al., Facile mass production of nanoporous SnO_2 nanosheets as anode materials for high performance lithium-ion batteries, J Colloid Interf. Sci. 503 (2017): 205-213.

[24] Luo G E, Liu W J, Zeng S S, et al., Hierarchal mesoporous SnO_2@C@TiO_2 nanochains for anode material of lithium-ion batteries with excellent cycling stability, Electrochim. Acta 184 (2015): 219-225.

[25] Wu P, Du N, Zhang H , et al., Self-templating synthesis of SnO_2-carbon hybrid hollow spheres for superior reversible lithium ion storage, ACS Appl. Mater. Interfaces 3 (2011): 1946-1952.

[26] Hong Y J, Son M Y, Kang Y C. One-pot facile synthesis of

double-shelled $SnO_{(2)}$ yolk-shell-structured powders by continuous process as anode materials for Li-ion batteries, Adv. Mater. 25 (2013): 2279-2283, 2250.

[27] Ma D Q, Dou P, Yu X H, et al., Novel hollow SnO_2 nanosphere@TiO_2 yolk–shell hierarchical nanospheres as anode material for high-performance lithium-ion batteries, Mater. Lett. 157 (2015): 228-230.

[28] Yi L G, Liu L, Guo G X, et al., Expanded graphite@SnO_2@polyaniline composite with enhanced performance as anode materials for lithium ion batteries, Electrochim. Acta 240 (2017): 63-71.

[29] Hu L L, Yang L P, Zhang D, et al., Designed synthesis of SnO_2-C hollow microspheres as an anode material for lithium-ion batteries, Chem. Commun. 53 (2017): 11189-11192.

[30] Liu Q, Dou Y, Ruan B, et al., Carbon-Coated Hierarchical SnO_2 hollow spheres for lithium ion batteries, Chem. Eur. J. 22 (2016): 5853-5857.

[31] Wang Y, I. Djerdj, B. Smarsly, et al., Antimony-doped SnO_2 nanopowders with high crystallinity for lithium-ion battery electrode, Chem.Mater. 2009, 21: 3202-3209.

[32] Yan Y, Du F, Shen X, et al., Large-scale facile synthesis of Fe-doped SnO_2 porous hierarchical nanostructures and their enhanced lithium storage properties. J. Mater. Chem. A 2 (2014): 15875-15882.

[33] Wang X K, Li Z Q, Zhang Z W, et al., Mo-doped SnO_2 mesoporous hollow structured spheres as anode materials for high-performance lithium ion batteries, J. Mater. Chem. A 2 (2015): 3604-3613.

[34] Ma Y.J, Ma Y, U. Ulissi, et al., Influence of the doping ratio and the carbon coating content on the electrochemical performance of Co-doped SnO_2 for lithium-ion anodes, Electrochim. Acta 277 (2018): 100-109.

[35] Zhao P, Yue W B, Yuan X, et al., Exceptional lithium anodic performance of Pd-doped graphene-based SnO_2 nanocomposite. Electrochim. Acta 225 (2017): 322-329.

[36] W. Stöber, A. Fink, E. Bohn, Controlled growth of monodisperse silica spheres in the micron size range, J. Colloid and Interf. Sci. 26 (1968): 62-69.

[37] Wang S, Yu X H, Liu J X, et al., Encapsulation of SnO_2 nanoparticles between the hollow TiO_2 nanosphere and the carbon layer as high-performance negative materials for lithium-ion batteries, J. Alloy. Compd. 814 (2020): 152342-152349.

[38] Zhang Y N, Zhang Y J, Rong J, et al., Design and controllable synthesis of core-shell nanostructured Ni-P particles with an ionothermal strategy, J. Alloy. Compd. 795 (2019): 177-186.

[39] Wang Y, Guo W B, Yang Y Q, et al., Rational design of SnO_2@C@MnO_2 hierarchical hollow hybrid nanospheres for a Li-ion battery anode with enhanced performances, Electrochim. Acta 262 (2018): 1-8.

[40] Cui D M, Zheng Z, Peng X, et al., Fluorine-doped SnO_2 nanoparticles anchored on reduced graphene oxide as a high-performance lithium ion battery anode, J. Power Sources 362 (2017): 20-26.

[41] F. Mueller, A. Gutsche, H. Nirschl, et al., Iron-doped ZnO for lithium-ion anodes: impact of the dopant ratio and carbon coating content, J. Electrochem. Soc. 164 (2017): A6123-A6130.

[42] F. Mueller, D. Bresser, V.S.K. Chakravadhanula, S. Passerini, Fe-doped SnO_2 nanoparticles as new high capacity anode material for secondary lithium-ion batteries, J. Power Sources 299 (2015): 398-402,

[43] P. Nithyadharseni, K.P. Abhilash, S. Petnikota, et al., Synthesis and lithium storage properties of Zn, Co and Mg doped SnO_2 nano materials, Electrochim. Acta 247 (2017): 358-370,

[44] D. Bresser, F. Mueller, M. Fiedler, et al., Transition-metal-doped zinc oxide nanoparticles as a new lithium-ion anode material, Chem. Mater. 25 (2013): 4977-4985.

[45] J.Y. Cheong, C. Kim, J.-W. Jung, et al., Incorporation of amorphous TiO_2 into one-dimensional SnO_2 nanostructures as superior anodes for lithium-ion batteries, J. Power Sources 400 (2018): 485-492.

[46] Pan L, Zhang Y, Lu F, et al., Exposed facet engineering design of graphene-SnO_2 nanorods for ultra-stable Li-ion batteries, Energy Storage Mater. 19 (2019): 39-47.

[47] T.I. Koranyi, Z. Vit, D.G. Po et al.duval, R. Ryoo, H.S. Kim, E.J.M. Hensen, SBA-15-supported nickel phosphide hydrotreating catalysts, J. Catal. 253 (2008): 119-131.

[48] Y. Okamoto, Y. Nitta, T. Imanaka, et al., Surface characterisation of nickel boride and nickel phosphide catalysts by X-ray photoelectron spectroscopy, J. Chem. Soc. 75 (1979): 2027-2039.

[49] Zhu C R, Xia X H, Liu J L, et al., TiO_2 nanotube@SnO_2 nanoflake core–branch arrays for lithium-ion battery anode, Nano Energy 4 (2014): 105-112.

[50] Cheng Y Y, Huang J F, Qi H, et al., Adjusting the chemical bonding of SnO_2@CNT composite for enhanced conversion reaction kinetics, Small 13 (2017): 1700656.

[51] Wang X L, Li J Z, Chen Z, et al., Hierarchically structured C@SnO_2@C nanofiber bundles with high stability and effective ambipolar diffusion kinetics for high-performance Li-ion batteries, J. Mater. Chem. A 4 (2016): 18783-18791.

[52] Wang H M, Yan Y, Chen G. The effects of confinement on TiO_2@SnO_2@TiO_2 hollow spheres for high reversible lithium storage capacity, J. Alloy. Compd. 778 (2019): 375-381.

Viser Technology Pte. Ltd.
Research and Application of Materials Science
DOI: 10.33142/rams.v3i2.6730

Research Article **Open Access**

Influence of Mn and Mg Contents on Mechanical Properties of the Die-casting Aluminum Alloy HL-111

Yanyang HE*, Gang XU, Xiguang YU

Ningbo Heli Mould Technology Co., Ltd. Ningbo, Zhejiang, China

***Corresponding Author:** *Yanyang HE, Ningbo Heli Mould Technology Co., Ltd. Ningbo, Zhejiang, China; yanyang.he@Helimould.com**

Abstract:

In this study, four groups of thin plate samples with a wall thickness of 2.2mm, 2.5mm, 2.7mm, and 3.0mm are prepared by ultra-high vacuum die casting. The effects of Mn, Mg, and Mn/Mg ratio on the microstructure and mechanical properties of samples with different wall thicknesses are obtained by different test and analysis methods. The results show that as the content of Mn is 0.4% ～ 0.65%, the content of Mg is 0.17% ～ 0.5%, and the Mn / Mg ratio reaches 1.69 ～ 1.90, the tensile strength, yield strength, and elongation of HL-111 alloy with a wall thickness of 2 ～ 3mm can reach more than 280MPa, 120MPa and 10% respectively, and the mechanical properties of the material are greatly improved. In addition, the tensile strength, yield strength, and elongation of HL-111 alloy after T5 heat treatment at 165℃ for 510min reach 302.36 MPa, 190.32 MPa, and 8.42%. The precipitated phase of Mg_2Si leads to changes in strength and elongation.

Keywords: *HL-111 alloy; Mn/Mg element ratio; Microstructure; Mechanical properties*

1 Introduction

Al-Si alloys (such as Magcimal-59, Castasil-37, and Silafont-36) are widely used in ultra-high vacuum and high-pressure casting of conventional parts because of their good casting properties [1]. With the continuous improvement of automobile lightweight technology, Silafont-36 alloy has high strength and elongation, which is particularly favored in the manufacture of structural parts with high requirements for safety performance, such as car body frame and shock absorber [2-3]. Especially, the continuous innovation of ultra-high vacuum pressure casting technology, the increasing maturity of large die casting machine technology, and the needs of new energy vehicles make Silafont-36 alloy shine in the application of die casting large-size, complex structure, and ultra-thin wall thickness structural parts [4-6].

Due to the large size and complex structure of structural body parts, they usually have extremely high requirements for wall thickness. Take the application of Silafont-36 alloy in the shock tower as an example, its functional area wall thickness is in the range of 2～3 mm. However, Silafont-36 alloy is usually subjected to T7 heat treatment during the high-pressure casting production process in order to ensure the high strength and high toughness of the structural parts, which is prone to different degrees of unpredictable deformation after the T7 heat treatment, and the resulting rework correction and scrap rate are great costs. At the same time, T7 heat treatment will also make the production costs significantly increased. These increases of upstream manufacturing cost will aggravate the improvement of downstream industry cost, which will lead to the enterprise being invisible in the heavy burden forward. Therefore, it is imperative to find a way to maintain the high toughness and high strength of Silafont-36 alloy after die-casting, so as to reduce the manufacturing cost by eliminating the T7 heat treatment.

The main methods to improve the strength of the alloy mainly include fine-grain strengthening, dispersion strengthening, etc. Therefore, the strength of the alloy can be improved by controlling the strengthening phase in the alloy. It is well known that Mg_2Si is a common strengthening phase in aluminum alloys because of its high strength, but when the magnesium element is excessive, it will cause the coarsening of the Mg_2Si phase, which will reduce the strength of the alloy, so reasonable control of the magnesium element content in the alloy will be beneficial to enhance the strength of the alloy. On the contrary, the dispersion strengthening of Mg_2Si can improve the strength of the alloy, but it will also reduce the plasticity and toughness of the alloy, so we should take measures to improve the plasticity and toughness of the alloy at the same time. One of the most effective methods is to refine the grain of the alloy. Manganese is one of the strengthening elements of aluminum alloy, which can reduce the size of recrystallized grains and

Received on October 20, 2021; Accepted on December 26, 2021

improve the strength, plasticity, and toughness of the alloy. Therefore, proper adjustment of the Mn/Mg element ratio in the alloy can achieve the purpose of improving the strength and toughness of the alloy at the same time to replace the T7 heat treatment.

Ningbo Heli Technology Co., Ltd. has several years of practical production experience in the die-casting Silafont-36 alloy, focusing on the improvement of part qualification rate and the control of production cost. Based on Silafont-36, the company has reasonably allocated alloy elements and obtained an HL-111 alloy product with different wall thicknesses. The as-cast mechanical properties of HL-111 alloy fully meet the requirements of high strength and high toughness of the original Silafont-36 alloy after T7 heat treatment, which can omit the T7 heat treatment process of parts and eliminate all costs brought by the whole process.

2 Experimental

The molten aluminum was melted in a 300 kg resistance furnace. When the temperature was set at 720℃, the refining degassing time was 50 min. In the degassing process, the modifier Al-10Sr master alloy [7-8] and super refiner TCB seed alloy [9-10] were added, during which the degassing was uninterrupted. After the refining degassing was qualified, stand for 10 min, and transferred the molten aluminum to the side furnace of 300T-Buhler small die casting machine after the temperature of the molten aluminum was stabilized at 710℃. Then HL-111 die casting samples with a wall thickness of 2.2 mm, 2.5 mm, 2.7 mm, and 3 mm and corresponding element ratio were carried out successively, the physical drawing of the casting is shown in Figure 1. After the preparation of castings, HL-111 die-casting samples were prepared by wire cutting according to the requirements of GB / T 228 standard. After that, the HL-111 die-casting samples with the best performance were selected and subjected to T5 heat treatment at 155℃, 165℃, and 175℃ for 120 min, 240 min, and 510 min respectively to obtain HL-111 heat-treated samples.

Figure 1 The physical drawing of HL-111 casting

During the test, the alloy chemical composition of the HL-111 die-casting sample was analyzed by SPECTRO MAXx07-F element direct reading spectrometer. Wipe the sample surface and the spark table of the direct-reading spectrometer with absolute ethanol to avoid impurities affecting the analysis results. Select the brand of Silafont-36 alloy for spectral analysis. Combined with the actual element percentage of four Mn/Mg ratio levels, the element composition was obtained when the alloy wall thickness was 2 ～ 3 mm, as shown in Table 1.

Table 1 Table of optimum alloy elements with a wall thickness of 2 ～ 3mm

Element	Si	Fe	Mn	Mg	Cu
Count (%)	9.5～11.5	≤0.15	0.4～0.65	0.17～0.5	＜0.05
Element	Sr	Zn	Ti	Other	Al
Count (%)	0.02～0.03	0.07～0.1	≤0.2	＜0.15	Other

CMT5205 electronic universal testing machine was used to carry out the tensile test on two kinds of samples to measure their mechanical properties. The microstructure of the sample was analyzed by OLYMPUS GX53 metallographic microscope and scanning electron microscope (SEM, Nova SU-70, Hitachi). The metallographic diagrams of Silafont-36 alloy and HL-111 alloy with different wall thickness can be seen in Figure 2. The transmission electron microscope samples of HL-111 alloy were prepared by Gatan 695 ion thinning instrument. The transmission electron microscope patterns of HL-111 alloy were measured by FEI Talos F200X.

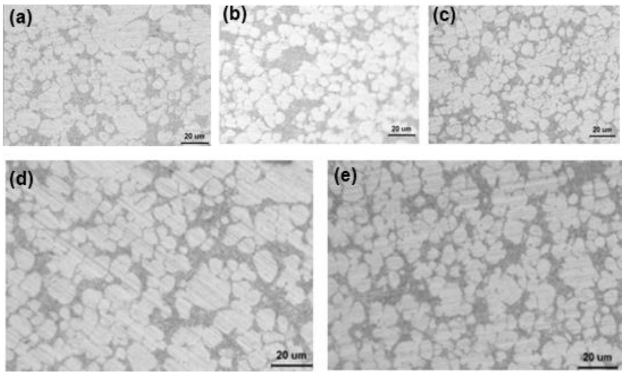

Figure 2 (a) Metallographic diagram of Silafont-36 alloy. (b-e) Metallographic diagram of HL-111 sample with a wall thickness of 2.2 mm (b), 2.5 mm (c), 2.7 mm (d), and 3.0 mm (e)

Table 2 The number of HL-111 die casting samples

Num	Wall thickness (mm)	Mn/Mg
1	2.2	1.65
…		
12		1.90
13	2.5	1.65
…		…
24		1.90
25	2.8	1.65
…		…
36		1.90
37	3.0	1.65
…		…
48		1.90

Tensile test design of HL-111 die-casting specimen: adopting four kinds of die-casting specimens with a length of 200 mm, a width of 40 mm, and thickness of 2.2 mm, 2.5 mm, 2.8 mm, and 3.0 mm. The Mn/Mg ratio of the specimens with different thicknesses is adjusted to 1.65, 1.69, 1.71, 1.73, 1.75, 1.77, 1.79, 1.81, 1.83, 1.85, 1.88, and 1.90 respectively, and the serial numbers are numbered 1, 2, 3..., 47 and 48, as shown in Table 2.

3 Results and Discussions

3.1 Analysis of chemical composition and microstructure of HL-111 alloy

The microstructure of the sample was analyzed by 500X optical microscope. During the crystallization process of Silafont-36 alloy, α_1-Al phase will be precipitated first, and the liquid aluminum alloy reaches aluminum-silicon eutectic composition. As the temperature decreases, the eutectic silicon phase in the liquid alloy will grow coupled with α_2-Al phase until complete solidification. As shown in Figure 2a, it can be seen that in the as-cast structure of the original Silafont-36 alloy, the white coarser organization is the primary α_1-Al phase. The fine and round white structure is the secondary α_2-Al phase. The irregular growth of the α-Al phase can inhibit the growth of the eutectic silicon phase and thus constantly change the growth direction, which eventually generates relatively closed clusters [11-13], which reduces the coupling degree with other phases. The length of the α_1-Al phase is greater than 27.09 μm, the diameter of α_2-Al phase is 7.41 μm, the proportion of eutectic silicon is 36.91%. This non-uniform distributed organization will lead to uneven stress distribution in the process of stressing the alloy, causing damage to the weak phases in the alloy and reducing the overall mechanical properties.

By comparing the microstructure distribution differences between HL-111 die-casting specimens with four different wall thicknesses and the original silafont-36 alloy, Figure 2b-d indicated that as the Mn / Mg ratio reached the range of 1.73 ～ 1.89, the primary phase and second phase of α-Al were not obvious. In addition, the eutectic silicon was fully coupled to grow, and the overall distribution was relatively uniform, which is conducive to enhancing the toughness and strength of HL-111 alloy. The size of the α-Al phase was calculated by the software, the maximum length of the α_1-Al phase was only 16.43 μm, the diameter of the secondary phase was 7.40 μm, and the percentage of eutectic silicon was reduced to 26.62% ～ 30.02%.

Mg_2Si phase will precipitate after T5 heat treatment at 165℃ for 510 min in the HL-111 die-casting sample. Firstly, the element distribution of the ion milling sample is analyzed by X-ray energy dispersive spectrometer (EDS) through the transmission electron microscope (TEM), as shown in Figure 3a. The yellow area in the figure is the possible location of the precipitated phase. Then, implementing spot measurement to the yellow area by EDS of TME to further determine the location of the Mg_2Si precipitated phase, as shown in Figure 3a, b. To further prove that there was precipitation of Mg_2Si phase in the HL-111 sample after T5 heat treatment, the area circled in Figure 3a is analyzed by selected-area electron diffraction and high-resolution transmission electron microscope (HRTEM). By calibrating the diffraction pattern and lattice spacing of the precipitated phase (Figure 3e, f), it is completely consistent with the PDF card (#65-9365) of Mg_2Si, which fully demonstrated that the Mg_2Si phase was precipitated after T5 heat treatment of HL-111. The morphology of Mg_2Si is shown in Figure 3c, d. Through the analysis of the Mg_2Si precipitated phase and its surrounding elements by high-angle annular dark-field (HAADF), there were evenly dispersed aluminum atoms around Mg_2Si precipitated phase, indicating that the precipitated phase is distributed on Al substrate. The Mg_2Si phase could hinder the dislocation movement and was conducive to improving the yield strength of HL-111 alloy, as shown in Figure 3g-j.

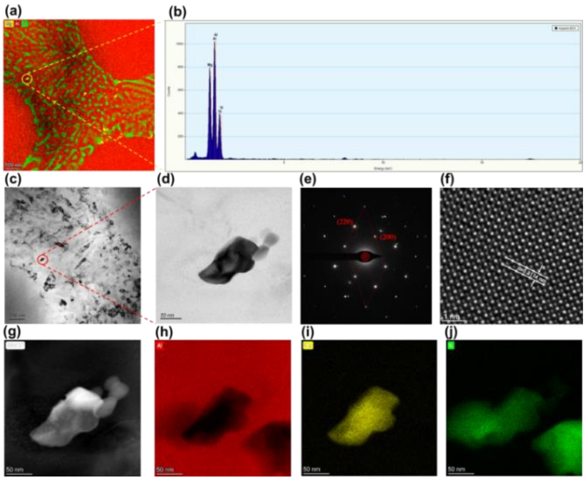

Figure 3 (a) The EDS mapping of HL-111alloy. (b) EDS point measurement in the area within the yellow circle. (c) TEM image of HL-111 after T5 heat treatment. (d) TEM morphology of Mg_2Si precipitated phase. (e) Selected-area electron diffraction (SAED) pattern of Mg_2Si precipitated phase. (f) The HRTEM image of Mg_2Si. (g-j) The HAADF diagram (g) and element distribution diagram of Mg_2Si precipitated phase: Al element (h), Mg (i), and (Si).

3.2 Mechanical property test

The dimensions of tensile specimens are shown in Figure 4. The operation and parameters of the tensile experiment are as follows. Remove the oil stain from the surface of the standard specimen. Set the test parameters of the universal testing machine according to GB/T228 standard [14]: the tensile speed was 4 mm/s, the extensometer was YYU-10/50, then input the cross-sectional area of the sample, and the tensile test is carried out. The tensile test results of HL-111 die-casting samples with different wall thicknesses are shown in Table 3 The tensile test results of the HL-111 sample with a wall thickness of 2.7 mm after different T5 heat treatments are shown in Table 4.

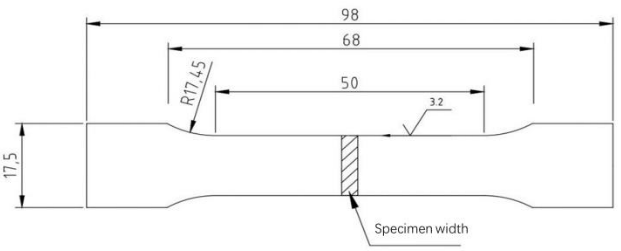

Figure 4 Schematic diagram of tensile specimen

Table 3 The mechanical properties of HL-111 die-casting samples with different wall thickness

Specimen thickness (mm)	Tensile strength (MPa)	Yield strength (MPa)	Elongation (%)
2.2	284.58	122.21	11.06
2.2	288.82	124.4	11.77
2.5	287.82	127.25	10.67
2.5	280.14	120.05	12.43
2.7	291.04	129.86	11.93
2.7	283.93	122.92	10.34
3	295.14	123.83	11.24
3	299.21	125.72	10.4

Table 4 The mechanical properties of HL-111 after different T5 heat treatments

Heat treatment parameters (℃/min)	Tensile strength (MPa)	Yield strength (MPa)	Elongation (%)
155℃/120min	294.05	182.30	5.84%
155℃/240min	296.34	184.52	5.63%
155℃/510min	299.50	188.47	5.72%
165℃/120min	295.28	184.23	5.76%
165℃/240min	297.44	186.48	5.83%
165℃/510min	302.36	190.32	8.42%
175℃/120min	296.32	186.23	5.53%
175℃/240min	299.62	189.24	5.73%
175℃/510min	305.32	192.93	5.62%

The elongation of the original Silafont-36 alloy after T7 heat treatment is generally 10%, the tensile strength is 200 MPa, and the yield strength is 120 MPa. As can be seen from Table 3, controlling the relationship between wall thickness and composition, the elongation of HL-111 as-cast samples without heat treatment exceeded 10% and the yield strength was stable above 120 MPa. More importantly, the tensile strength was significantly improved and could reach more than 280 MPa. According to the Hall-Petch formula, with the decrease of grain size, the number of large-angle grain boundaries of the alloy will increase [15]. When the alloy is subjected to external stress, the dislocations in the grain cannot cross the grain boundary and accumulate on it. When the external stress increases, the dislocation source of adjacent grains will move and start plastic deformation [16]. Therefore, HL-111 alloy with smaller grains would have a greater strength [17]. At the same time, the grain distribution of HL-111 alloy was more uniform. When the alloy had plastic deformation, the plastic deformation could be more evenly distributed in each grain, which was not easy to produce stress concentration, so HL-111 alloy could withstand more deformation and have a good plasticity. Compared with Silafont-36, the proportion of eutectic silicon in HL-111 is reduced. The reduction of the proportion of eutectic silicon can not only reduce the strength reduction caused by eutectic silicon but also improve the yield strength of HL-111 alloy.

After T5 heat treatment at 165℃ for 510 min, the tensile strength of HL-111 was 290-310 MPa, the yield strength was 180-220 MPa, and the elongation was higher than 8%, while the elongation after heat treatment at other temperature and time was less than 6%. Because the HL-111 alloy will precipitate the Mg_2Si phase at the grain boundary after T5 heat treatment at 165 ℃ for 510min. The precipitation of Mg_2Si phase would form Cottrell atmosphere at the grain boundary and lead to the pinning effect, which could hinder the dislocation slip in the HL-111 alloy and increase the strength of the metal, especially the yield strength. Moreover, the yield ratio of HL-111 alloy will also increase, which will make the metal difficult to plastic deformation, which will lead to the decrease of elongation. The time and temperature of heat treatment will affect the precipitation and distribution of Mg_2Si. When the heat treatment time is too long or short, the plasticity of HL-111 will significantly decrease.

3.3 Fracture dimple analysis

The fracture morphology of the original Silafont-36 alloy is shown in Figure 5a, b, and the fracture morphology of the HL-111 sample after adjusting the Mn/Mg ratio is shown in Figure 5c-h. The size of the fracture dimples mainly includes the average size and depth, which is closely related to the plasticity and fracture mode of the material. The parts with deeper fracture dimples break later in the fracture process, so the aluminum alloy with deeper fracture dimples has better plasticity. By comparing the dimple size of HL-111 alloy with different wall thickness and the original Silafont-36 alloy, as Mn/Mg reaches the range of 1.73-1.89, the dimple size and number of the HL-111 alloy are larger than Silafont-36 alloy. Therefore, the HL-111 alloy has excellent plasticity, and the elongation can reach more than 10%. This is because the proportion of eutectic silicon decreases while the α-Al phase increases after adjusting the Mn/Mg ratio, and brittle fracture occurs first at the eutectic silicon during the tensile process, however, the increase of α-Al phase can increase the plasticity of the HL-111 alloy.

After T5 heat treatment, the dimple size and depth on the fracture surface of HL-111 alloy become smaller, and the fracture surface locally presents the rock shape with a few tear lines, which shows the plasticity of the T5 heat-treated HL-111 alloy is less than that of as-cast alloy [18]. The fracture mode of T5 heat-treated HL-111 alloy in the tensile test is between brittle fracture and ductile fracture. Because the Mg_2Si precipitated from HL-111 alloy after heat treatment is brittle and distributes on the grain boundary. Under the action of stress, there will be some microporous cracks, which make the alloy brittle.

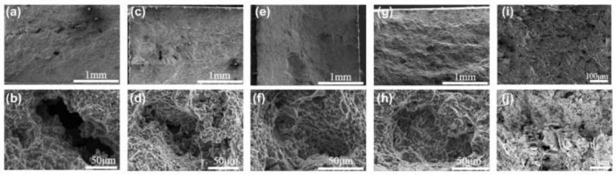

Figure 5 The SEM images of the fracture surface of Silafont-36, HL-111 with different wall thickness and T5 heat-treated HL-111 alloy. (a-b) Tensile fracture morphology of Silafont-36 as-cast alloy; (c-h) Tensile fracture morphology of HL-111 alloy die-casting specimen. (i-j) Tensile fracture morphology of HL-111 sample after T5 heat treatment(165℃/510min)

4 Conclusion

Based on the element content of the Silafont-36 alloy, the tensile strength, yield strength, and elongation of HL-111 alloy with different wall thickness can reach more than 280 MPa, 120 MPa, and 10% respectively by adjusting Mn/Mg ratio. More importantly, as the Mn/Mg ratio reaches 1.73 ～ 1.89, the as-cast HL-111 alloy with a wall thickness of 2-3 nm can replace the T7 heat treatment process of the original Silafont-36 alloy. In addition, as the Mn/Mg ratio in HL-111 is 1.73 ～ 1.89, the crystallization law of microstructure in HL-111 will change. The distance between the primary phase and the secondary phase of α-Al decreases, and the grains are regularly and evenly distributed, to better improve the mechanical properties of the alloy. Moreover, Mg_2Si will precipitate in HL-111 alloy after T5 heat treatment at 165℃ for 510 min and distribute on the grain boundary, which will produce a pinning effect to improve the metal strength, and slightly reduce the elongation. The tensile strength, yield strength, and elongation of HL-111 alloy after T5 heat treatment with 2.7 mm wall thickness can reach 302.36 MPa, 190.32 MPa, and 8.42%.

Author Contributions: YH put forward the experimental idea and designed the experiment, analyzed the data, and finally wrote the draft of the article. GX and XY also implemented some experimental tests and revised the original draft. All authors read and approved the final manuscript.

Conflict of Interest: The authors declare that there is no conflict of interest regarding the publication of this paper.

References

[1] Cai Z, Zhang C, Wang R, et al., Preparation of Al－Si alloys by a rapid solidification and powder metallurgy route. Mater. Des, 2015(87): 996-1002.

[2] Dash S S, Li D J, Zeng X Q, et al., Heterogeneous microstructure and deformation behavior of an automotive grade aluminum alloy. Alloys Compd, 2021, 870: 159413.

[3] Meschut G, Matzke M, Hoerhold R, et al., Hybrid Technologies for Joining Ultra-high-strength Boron Steels with Aluminum Alloys for Lightweight Car Body Structures. Procedia CIRP, 2014(23): 19-23.

[4] Jiao X Y, Zhang Y F, Wang J, et al., Characterization of externally solidified crystals in a high-pressure die-cast AlSi10MnMg alloy and their effect on porosities and mechanical properties. J Mater Sci Technol 2021, 298: 117299.

[5] Dou K, Lordan E, Zhang Y, et al., A novel approach to optimize mechanical properties for aluminium alloy in High pressure die casting (HPDC) process combining experiment and modelling. J Mater Sci Technol, 2021, 296: 117193.

[6] Liu R, Zheng J, Godlewski L, et al., Influence of pore characteristics and eutectic particles on the tensile properties of Al–Si–Mn–Mg high pressure die casting alloy. Mater. Sci. Eng. A, 2020, 783: 139280.

[7] Qiu K, Wang R C., Peng C Q, et al., Effect of individual and combined additions of Al–5Ti–B, Mn and Sn on sliding wear behavior of A356 alloy. Trans. Nonferrous Met. Soc. China 2015, 25, 3886-3892.

[8] Tan P , Yang Y, Sui Y, et al., The influence of Al–10Sr or/and Al－5Ti–1B on microstructure and mechanical properties of Al–12Si–4Cu–2Ni–0.8 Mg alloys. J.Alloys Compd, 2019, 809: 151856.

[9] Li P, Liu S, Zhang L, Liu X. Grain refinement of A356 alloy by Al–Ti–B–C master alloy and its effect on mechanical properties. Mater. Des 2013, 47, 522-528.

[10] Zhao K, Gao T, Yang H, et al., Influence of a new AlTiC–B master alloy on the casting and extruding behaviors of 7050 alloys. J. Alloys Compd 2020, 820: 153089.

[11] Wang J, Guo Z, Song J L, et al., On the growth mechanism of the primary silicon particle in a hypereutectic Al-20 wt%Si alloy using synchrotron X-ray tomography. Mater. Des 2018, 137, 176-183.

[12] Wang S R, Ma R, Wang Y Z, et al., Growth mechanism of primary silicon in cast hypoeutectic Al-Si alloys. Trans. Nonferrous Met. Soc. China 2012, 22, 1264-1269.

[13] Fang N, Zou C, Wei Z, et al., Microstructural evolution and mechanical properties of Al–Si–Cu–(Ge)–(Mg) alloy solidified under high pressure. Mater. Sci. Eng. A 2021, 827: 142065.

[14] Xiao Y, Hu Y. Numerical and Experimental Fracture Study for 7003 Aluminum Alloy at Different Triaxialities. Met.Mater. Int 2020, 27, 2499-2511.

[15] Naik S N, Walley S M. The Hall–Petch and inverse Hall–Petch relations and the hardness of nanocrystalline metals. J. Mater. Sci 2019, 55, 2661-2681.

[16] Loucif A, Figueiredo R B, Baudin T, et al., Ultrafine grains and the Hall–Petch relationship in an Al–Mg–Si alloy processed by high-pressure torsion. Mater. Sci. Eng. A 2012, 532, 139-145.

[17] Liu L, Zhang Y, Han J, et al., Nanoprecipitate-Strengthened High-Entropy Alloys. Adv Sci (Weinh) 2021, 8: e2100870.

[18] Suryanarayana C, Al-Aqeeli N. Mechanically alloyed nanocomposites. Prog. Mater. Sci. 2013, 58, 383-502.

Viser Technology Pte. Ltd.
Research and Application of Materials Science
DOI: 10.33142/rams.v3i2.6731

Research Article Open Access

An Effective Way to Prepare Submicron MoO_2 Anodes for High- Stability Lithium-Ion Batteries

Xiu-Lan LI, Jian LIN, Cui-Yan TONG*, Hai-Zhu SUN*

National & Local United Engineering Laboratory for Power Battery, College of Chemistry, Northeast Normal University, Changchun, China

***Corresponding Author:** *Hai-Zhu SUN and Cui-Yan TONG, 5268 Renmin Street, Changchun, 130024, P. R. China; sunhz335@nenu.edu.cn;tongcy959@nenu.edu.cn*

Abstract:
Herein, MoO_2-based submicrons (named MoO_2@C) are synthesized through an effective one-step hydrothermal process. The prepared MoO_2 submicrons wrapped in carbonouse layer are uniformly produced and can be applied to the anodes in lithium-ion batteries (LIBs). The novel MoO_2@C electrodes demonstrate attractive lithium storage ability. Moreover, compared with the commercial pure MoO_2, the MoO_2@C delivers a superior electrochemical capacity (e.g, 760.83 mAh g^{-1} capacity in long-life test at high rate of 1 A g^{-1}) with outstanding capacity retention ratio and stability as well as rate capability. The superior lithium storage capabilities result from plenty of the Li^+ sites and adequate electrolyte infiltration effect, which allows the fast transport of electrons and ions, and well-dispersed MoO_2 submicrons in carbon-based layers that effectively prevents aggregation of nano size particles.

Keywords: *submicrons; MoO_2; Carbon coating; Lithium-ion battery*

1 Introduction

Increasing of environmental and energy problems has triggered strong research interests in the use of sustainable and renewable energy storage devices [1-4]. As a new emerging Mo-based material applying in LIBs, potential MoO_2 equips with the intrinsic metallic nature (bulk electrical conductivity up to $1.1 \times 10^6\ \Omega^{-1}\ m^{-1}$ at 300 K) and the low electrical resistivity with one-dimensional (1D) tunnel structure, which can significantly facilitate Li^+ and electron transport kinetics [5-7]. Moreover, MoO_2 with the high density of 6.5 g cm^{-3}, which is about 3.25 times compared with commercial graphite (2 g cm^{-3}), makes it possible to obtain 7.3 times capacity of graphite under similar volume condition [8-11]. Therefore, MoO_2 anodes have been given great interests to the field of lithium-ion batteries (LIBs). However, the three major bottlenecks limit its practical full cell application. (i) The pulverization results in poor cyclic capacity and capacity faded phenomenon because of the fully conversion reaction possesses [12-13]. (ii) The unsatisfying rate performance results from relatively low conductivity [14-15] (iii) The sluggish kinetics limit lithium-ion transportation in bulk MoO_2. Therefore, it is great challenge to prepare MoO_2 based electrode materials.

Preparing the nano-sized MoO_2@C is an effective solution to the bottlenecks. Usually, MoO_2 is prepared by the reduction of MoO_3[16-18]. In the synthesis process, MoO_3 is treated under a hydrogen atmosphere at high temperature, followed by the formation of large particles. For example, Song et al. adopted the ultrasonic spray pyrolysis to make spherical molybdenum dioxide materials. The precursor solution was prepared using aqueous ammonium molybdate and sucrose as the reducing agent and carbon source, and the ultrasonic spray pyrolysis was carried out at 550-650℃ under 5% H_2 / Ar atmosphere. Spheres with diameters of 2-6 μm were obtained[19]. Zhang et al. used ammonium hepta-molybdate tetrahydrate as a precursor and polyvinylpyrrolidone as a modifier to first prepare molybdenum trioxide nanoparticles by hydrothermal synthesis, and then obtained molybdenum dioxide nanoparticle by high temperature reduction at 420 ℃ under argon-hydrogen atmosphere, with nanoparticle size around 300 nm[20].

In this work, a nano-spherical MoO_2@C material with an average particle size of ～200 nm is prepared by the simple hydrothermal method without any impurities, which is a very competitive way for large scale production. Besides, for the green chemical concept, the biomass gelatin is selected as carbon source. The structure, morphology, and electrochemical properties of the MoO_2@C composite are investigated using various analytical techniques. Particularly, the MoO_2@C anode shows the better long-term stability compared with pure MoO_2. The rate-capability and capacity retention of the synthesized material are significantly improved compared with the commercial pure MoO_2 (5

Received on September 28, 2021; Accepted on December 17, 2021

times capacity enhancement at 1 A g^{-1} in the cycling test). The experimental results show that the uniform carbon distribution and nano-sized particle offer more adsorption sites to shorten the ion transport pathway resulting from the effective routine. Furthermore, the analysis tests indicate that there is no damage for the structure of MoO_2@C after working 1000 cycles. Therefore, this work may offer a novel strategy for design of nano-size particles electrode materials with high-performance for Li^+ based energy storage devices.

2 Experimental Section

2.1 Materials

Ammonium molybdate tetrahydrate ($(NH_4)_6Mo_7O_{24}\cdot 4H_2O$), gelatin and sodium hydroxide (NaOH) were purchased from Aladdin company. All chemical reagents are used without purify.

2.2 Preparation of MoO_2@C.

Typically, 0.50 g $(NH_4)_6Mo_7O_{24}\cdot 4H_2O$ was stirred for 30 min in 25 mL deionized water. Then, gelatin (0.76 g) was added and stirred for 30 min (80℃). After that, 1 mL NaOH (1 M) solution was injected into it with ultra-stir for 15 min. Finally, the uniform solution was transferred in Teflon reactor (capacity: 50 mL). After reacting at the 200℃ for 24 h, the product was washed with water and ethanol two times, respectively. The prepared black powder was transferred in tube furnace with the heating process at the 500℃.

2.3 Material characterizations

The powder X-ray diffraction using Cu Kα radiation (XRD, Smartlab 2200PC) was implemented to identify the phase of MoO_2@C. To figure out the size, morphology and the element distribution in MoO_2@C, field-emission scanning electron microscopy (SEM)and energy dispersive X-ray spectroscopy (EDX) were performed (HITACHI SU8010).

2.4 Electrochemical measurements

Blade-coating method was adopted to prepare the working electrodes. The materials weighted at the ratio of 7:2:1 (MoO_2@C / carbon black / polyvinyl difluoride) in proper amount of N-methylpyrrolidone (NMP). After stirred for one day, the slurry was rapidly bladed onto the copper foils and dried in the 80℃ condition.

The typical LIBs were assembled as followings in Ar-filled glovebox (SUniversal 2440/750). The pure lithium foil was used as counter electrode while MoO_2@C as the working electrodes, and 150 μL electrolyte (1.0 mol/L $LiPF_6$ in ethylene carbonate / dimethyl carbonate) as the electrolyte. The current density and capacity were calculated ～1 mg as the benchmark.

To value the electrochemical reaction, galvanostatic discharge/charge curves (GCD) and cyclic voltammetry (CV) were tested (LAND CT2001A). The electrochemical impedance spectra (EIS) was carried out on electrochemistry workstation (CHI750E) with a ±5 mV ac signal amplitude and a frequency ranged from 10 kHz to 0.01 Hz.

All the electrochemical tests were conducted at ～25℃.

3 Results and Discussion

Figure 1 schematically illustrates the formation of MoO_2@C submicrons. MoO_2@C was first synthesized by employing a hydrothermal process with $(NH_4)_6Mo_7O_{24}\cdot 4H_2O$ and gelatin, and then annealed to form nanostructured MoO_2@C. Nanostructured MoO_2@C will have a large surface area and more active sites, thus improving the kinetics of Li^+.

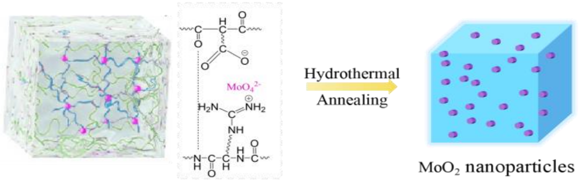

Figure 1 Schematic of the synthesis of the MoO_2@C.

The phase composition and crystal structure of MoO_2@C is further obtained by XRD. As shown in Figure 2a, the obtained composites are in good agreement with the space group p63/mmc (JCPDS: 37-1492) of pure MnO_2. The distinct diffraction peaks at 36.52°, 38.10°, 41.37°, 53.80° and 65.73° correspond to the (100), (002), (101), (102) and (110) planes, respectively. Moreover, the peak width at half width of diffraction peaks with strongly intensity suggests a small particle size and high crystallinity of MoO_2, consistent with the characteristics of pure MoO_2. Besides, the baseline of the XRD pattern increases considerably during 20-30°, which proves the occurrence of an amorphous carbon. All of these characterizations further confirm the successful preparation of the highly crystalline pure phase MoO_2@C sample.

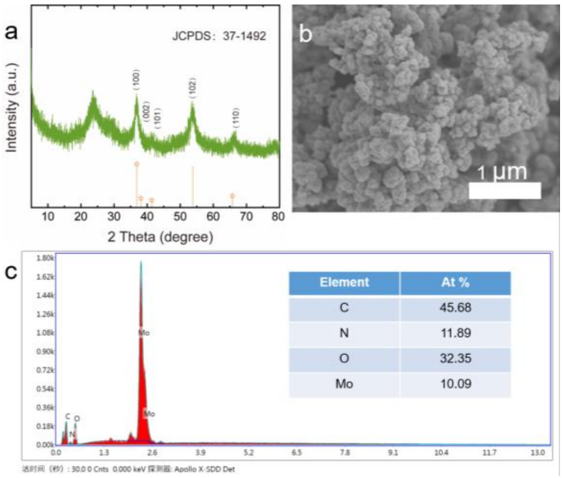

Element	At %
C	45.68
N	11.89
O	32.35
Mo	10.09

Figure 2 The characterizations of MoO_2@C (a) The XRD pattern. (b) The SEM image showing the average particle size with ～200 nm. (c) The EDX results of Mo, O, C and N

To further determine the structure, several tools were used to analyze the nanostructures and characterize the distribution of elements in the nanostructures. MoO_2@C is studied by SEM. SEM image shows the morphology and microstructure of MoO_2@C. It clearly presents uniform and smooth solid sphere with an average particle radius of about 200 nm (Figure 2b). After high temperature annealing treatment, the spheres still preserve its structure, indicating the stable structure.

Furthermore, as shown in Figure 2c, the EDX image shows the existence of Mo, O, N and C species with 10.09%, 32.35%, 11.89% and 45.68%. It is noticeable that gelatin plays a double functional role, as a reducing agent and a carbon source at the same time in the composite. On the grounds of the above results, it is confirmed the successful preparation of spherical MoO_2@C with nanoscale size.

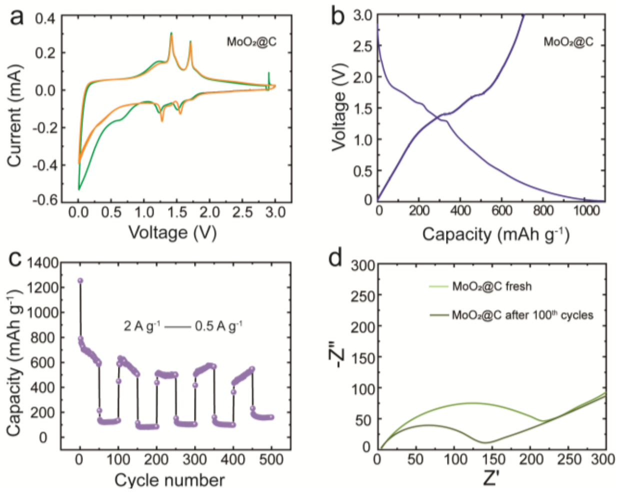

Figure 3 The electrochemical performances of MoO_2@C. (a) The first three cycles of CV curves. (b) The GCD curves. (c) The rate performances with 2 A g^{-1} charge and 0.5 A g^{-1} discharge. (d) The EIS image of MoO_2@C fresh and MoO_2@C after 100 cycles

To further explore the potential applicability of MoO_2@C as an anode material in LIBs, the typical button cells were assembled in the glove box and tested. As illustrated in Figure 3a, the CV of the MoO_2@C electrode is monitored over a voltage range in 0.01-3.0 V with a scan rate of 0.1 mV s^{-1}. In the first cycle, two cathodic of peaks are clearly observed at 1.25 V and 1.52 V. This mechanism of lithium ion insertion and de-insertion reaction is the same as that already reported in the paper[21]. The two cathodic peaks are in relation to the phase transition from monoclinic to orthoclinic of MoO_2 during Li^+ insertion. In accordance with the study of Dahn and McKinnon, the two oxidation peaks located at 1.47 V and 1.7 V are shown in the lithium extraction process[22]. The reduction peak that is located at ～0.6 V can be attributed to the formation of a solid electrolyte interphase (SEI) film between the MoO_2 submicrons and the electrolyte. The second cycle, the CV curve remains stable; meanwhile, its redox peaks are basically the same as the first cycle, located at 1.25V/1.47V and 1.52V/1.7V, respectively. This indicates that an irrecoverable reaction occurs during the initial Li^+ insertion, and then, no noticeable changes are observed in the subsequent cycles. The obtained potential shows that the material has good reversibility. At the same time, the polarization of the electrode material can be alleviated.

The GCD was valued in the potential range of 0.01-3 V, which is the area where the insertion/extraction reaction is known. Figure 3b reveals the voltage curves of the nanoscale MoO_2@C composite electrode. The first discharge and charge capacities are approximately 1363.51 mAh g^{-1} and 937.09 mAh g^{-1}, and the initial Coulombic efficiency (ICE) is 68.73%, which is mainly attributed to the irreversible lithium intercalation into the carbon. This is well coordinated with the broad peak observed in the CV curve. Other irreversible processes such as some lithium trapped in the MoO_2 lattice, the formation of SEI, and the pyrolysis of electrolyte can also affect the ICE. The reversible discharge capacity of the MoO_2@C compound is higher than its theoretical capacity, which can be attributed to the better Li^+ occupancy in the near-surface environment due to the nanoscale native particles of MoO_2[23]. Meanwhile, in the first cycle, two different discharge plateaus (0.5-1.0 V and 1.0-1.5 V) and charging plateaus (1.0-1.5 V and 1.5-2.0 V) can be observed, which is in good agreement with the oxidation and reduction peaks in the CV curves.

Besides, the MoO_2@C composition also shows a remarkably high-rate capability (Figure 3c). A high current charge is first set and cycled for 50 turns with an approximate specific capacity of ～120 mAh g-1; then a low current discharge is set and cycled for 50 turns with a specific capacity of ～510 mAh g-1, and continues to circulate 500 cycles. It is observed that the specific capacity of the electrode basically remains stable, indicating that the electrode material structure is stable.

To further understand the electrochemical reaction kinetics of MoO_2@C, EIS measurements were performed. Figure 3d shows the Nyquist plots of MoO_2@C in fresh and after 100 cycles. SEM image after cycling is shown in the inset. It is shown that each Nyquist plot consists of a depressed semicircle at high frequencies, a semicircle at medium frequencies, and a tilted line at low frequencies. They correspond to the migration resistance of lithium ions in the SEI interface layer, the charge transfer resistance, and the solid diffusion resistance of lithium ions in the active material, respectively. By comparing the two Nyquist plots, the diameter of the semicircle decreases significantly after cycling, which is attributed to electrochemical activation. It is worth noting that the tilt lines remain parallel throughout the cycling process, indicating that the solid diffusion of lithium ions is always stable. The EIS results indicate that the composite has relatively low impedance and fast Faraday reaction kinetics, consistent with its superior rate performance.

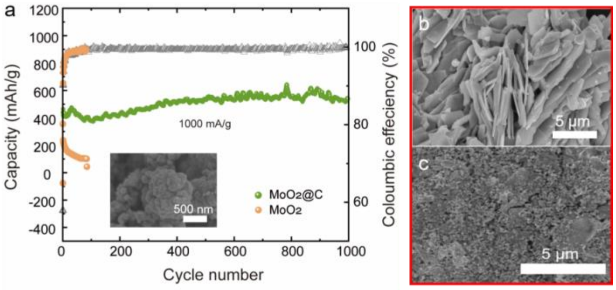

Figure 4 (a) The electrochemical cycling performances comparison of MoO_2@C and commercial MoO_2 and the inset image is the SEM image of MoO_2@C nanocomposites after cycling. (b, c) The SEM images of commercial MoO_2 before and after cycling

Remarkably, the long-term cycling stability tests at high current densities (1 A g^{-1}) show a discharge capacity of 760.83 mAh g^{-1} with capacity retention of ～69.75% (Figure 4a). During the cycles, all capacities show a tendency to increase and then smooth. This is due to the slow activation of the material makes the infiltration of the electrolyte after a period of time. As a point of comparison, the plain MoO_2 electrode display a much lower capacity of 231.00 mAh g^{-1} after the 84 loops at 1 A g^{-1} and an obvious decrease trend during electrochemical process. By comparing the SEM image of the MoO_2@C nanocomposites inside the Figure 4a, the SEM images of pure MoO_2 before and after cycling indicating that the structure of MoO_2 submicrons seriously break and collapse (Figure 4b, c). For the MoO_2@C, the structure still maintained a stable microstructure after cycling (the inset image in Figure 4a). Because the carbon coating can effectively mitigate the volume expansion of MoO_2 submicrons during the charge/discharge process and avoid the fragmentation of the electrode material.

4 Conclusion

In summary, a green and simply hydrothermal assisted method is adopted to synthesize MoO_2@C nanocomposites. As anode materials for Li-ion batteries, MoO_2@C nanocomposites demonstrate higher specific capacitance and more stable cycling ability than pure MoO_2. Besides, the MoO_2 submicrons that are embedded in amorphous carbon effectively improve the electrical conductivity and decrease the cycling resistance. Combined with lithium metal to aggregate the LIBs, the MoO_2@C anode displays a high initial discharge capacity of 760.83 mAh g^{-1} at 1 A g^{-1} and a long-time cycling stability of ～69.75% after performing 1000 cycles. All these results indicate that the MoO_2@C nanocomposites synthesized in this work have potential application in LIBs.

Author Contributions: X.L. Li and J. Lin were contributed this work equally. X.L. Li, J. Lin, and H. Z. Sun are contributors in this work. X.L. Li performed the whole experiment including samples preparation, electrode preparation, the cell assembly in a glove box and the measurement of electrochemical properties of the cycling and rate performance, the CV curves, the EIS test. J. Lin helped to characterize the morphology features such as SEM, TEM and XRD measurements and analyse the obtained results. Professor H.Z. Sun. supervised the project, wrote and revised the whole manuscript.

Conflict of Interest: No conflict of interest was reported by the authors.

Fund Project: Financial supports from the NSFC (22035001, 21574018, and 51433003), the Fundamental Research Funds for the Central Universities (2412019ZD002).

References

[1] Gu Z Y, Guo J Z, Sun Z H, et al., Air/water/temperature-stable cathode for all-climate sodium-ion batteries. Cell Reports Physical Science 2021, 2: 100665.

[2] Liang H J, Gu Z Y, Zhao X X, et al., Ether-based electrolyte chemistry towards high-voltage and long-life Na-ion full batteries. Angewandte Chemie International Edition 2021, 60: 26837.

[3] Zhao C D, Guo J Z, et al., Flexible quasi-solid-state sodium-ion full battery with ultralong cycle life, high energy density and high-rate capability. Nano Research 2022, 15: 925.

[4] Heng Y, Gu Z, et al., Research Progresses on Vanadium-based Cathode Materials for Aqueous Zinc-Ion Batteries. Acta Physico-Chimica Sinica 2021, 37: 2005013.

[5] Zhang H J, Shu J, et al., Lithiation mechanism of hierarchical porous MoO_2 nanotubes fabricated through one-step carbothermal reduction. Journal of Materials Chemistry A 2014, 2: 80-86.

[6] Y Wang, L Yu, et al., Formation of Triple-Shelled Molybdenum－Polydopamine Hollow Spheres and Their Conversion into MoO_2/Carbon Composite Hollow Spheres for Lithium-Ion Batteries. Angewandte Chemie International Edition 2016, 55: 14668-14672.

[7] Nithyadharseni P, Reddy M V, et al., Sn-based intermetallic alloy anode materials for the application of lithium ion batteries. Electrochim Acta 2015, 161: 261-268.

[8] Chen Z, Yang T, et al., Single Nozzle Electrospinning Synthesized MoO_2@C Core Shell Nanofibers with High Capacity and Long-Term Stability for Lithium-Ion Storage. Advanced Materials Interfaces 2017, 4: 1600816.

[9] Sun Y, Hu X, et al., Ultrafine MoO_2 nanoparticles embedded in a carbon matrix as a high-capacity and long-life anode for lithium-ion batteries. Journal of Materials Chemistry 2012, 22: 425-431.

[10] Yang L, Li X, Gao Q, et al., Hierarchical MoO_2/Mo_2C/C Hybrid Nanowires as High-Rate and Long-Life Anodes for Lithium-Ion Batteries. ACS Applied Materials and Interfaces 2016, 8: 19987-19993.

[11] Yang S, Feng X, et al., Fabrication of graphene-encapsulated oxide nanoparticles: towards high-performance anode materials for lithium storage. Angew. Chem. Int. Ed 2010, 49: 8408-8411.

[12] Zhang W M, Hu J S, et al., Tin-nanoparticles encapsulated in elastic hollow carbon spheres for high-performance anode material in lithium-ion batteries. Adv. Mater 2008, 20: 1160-1165.

[13] Qu Q, Gao T, et al., Strong surface-Bound Sulfur in Conductive MoO_2 Matrix for Enhancing Li-S Batterery Performance.Advanced Materials Interfaces 2015, 2(7): 150201-150206.

[14] Lu P, Xue D, et al., Hollow Nanostructured MoO_2 Electrode Materials for Supercapacitors. Materials Focus 2012, 1(2): 131-135.

[15] Palanisamy K, Kim Y, et al. Self-assembled Porous MoO_2/giaphene Microspheres towards High Performance Anodes for Lithium Ion Batteries. Journal of Power Sources 2015, 275: 351-360.

[16] Zhang R H, Hao Z H, et al., Mechanism of Non-Contact Reduction of MoO_3 to Prepare MoO_2. JOM 2022, 10: 22-24.

[17] Wang L, Zheng L X, et al., Mechanism and Kinetic Study of Reducing MoO_3 to MoO_2 with CO–15 vol % CO_2 Mixed Gases. ACS Omega 2019, 10: 1021-1030.

[18] Sun G D, Zhang G H, et al., Study on the reduction of commercial MoO3 with carbon black to prepare MoO_2 and Mo_2C nanoparticles. International Journal of Applied Ceramic Technology 2020, 10: 13473-13476.

[19] Song J H, Kang H J, et al., Electrochemical Characteristics of MoO_2 Anode Materials with Various Morphologies for LIB Applications. ECS Meeting Abstracts 2009, 2: 479.

[20] Zhang X Q, Hou Z G, et al., MoO_2 nanoparticles as high capacity intercalation anode material for long-cycle lithium ion battery. Electrochimica Acta 2016, 213: 416-422.

[21] Zhang X ,Ren H J, Xie B, et al., MoX_2 (X = O, S) Hierarchical Nanosheets Confined in Carbon Frameworks for Enhanced Lithium-Ion Storage. ACS Appl. Nano Mater. 2021, 4(5): 4615 – 4622.

[22] Wang Z, Chen J S, et al., ChemInform abstract: one-pot synthesis of uniform carbon-coated MoO_2, nanospheres for high-rate reversible lithium storage. Chem Commun 2010, 41(50): 6906 – 6908.

[23] Borghols W J H,Wagemaker M, et al., Size Effects in the $Li_{4+x}Ti_5O_{12}$ Spinel. J Am Chem Soc 2009, 131: 17786-17792.

Viser Technology Pte. Ltd.
Research and Application of Materials Science
DOI: 10.33142/rams.v3i2.6732

Research Article Open Access

Oxidation Resistance of Magnesium Alloyed by Different Elements: a Brief Review

Zhihui LIU[1], Zhuosong XIAO[1], Qi SUN[1], Guojun LIU[1*], S. Lippmann[2], Yongfu ZHU[1]

1 Key Laboratory of Automobile Materials, Ministry of Education (Jilin University), School of Materials Science and Engineering, Jilin University, 5988# Renmin Street, Changchun 130022, China
2 Otto Schott Institute of Materials Research, Friedrich Schiller University Jena, Löbdergraben 32, 07743 Jena, Germany

***Corresponding Author:** Guojun LIU, liuguojun@jlu.edu.cn*

Abstract:
The application of magnesium (Mg) and its alloys in automotive and aerospace industry is promoted gradually because of its outstanding properties, such as light weight, high specific strength and excellent castability. However, as a chemically active metal, Mg and its alloys generally possess low oxidation resistance in air at high temperatures because of the high affinity of Mg for O. This has caused a lot of industrial waste and a short service life. In the present work, according to the relevant mechanism of Mg alloy oxidation in air at high temperature, the effect of alloying elements on the oxidation of pure Mg and Mg alloys as well as the research progress of oxidation resistant Mg alloys are briefly reviewed.

Keywords: *Magnesium; Magnesium alloy; High temperature; Oxidation; Alloying elements*

1 Introduction

Magnesium (Mg) and its alloys, as the lightest metallic structure materials, has been widely employed in industries from aerospace to automotive products due to their low density, high specific strength and stiffness, wonderful machinability and excellent castability[1-3]. However, Mg alloys are prone to fire in the process of casting and processing due to their high activity and strong affinity with oxygen, which poses a potential danger to the safe operation of equipment and further limit its widespread applications. Therefore, most commercial magnesium alloys cannot be used in aircraft cabins [4-6].

The oxidation behaviors of Mg alloys will be effected by many factors, such as grain size, the quantity and the distribution of the intermetallic compounds, the content and distribution of alloying elements, the impurity and the texture or twin for the wrought Mg alloys. Both coating and ion implantation also can improve the corrosion resistance of alloys, however, these methods have a single function, i.e., only oxidation resistance at high temperature or corrosion resistance in NaCl solution and they are more complex in contrast to the alloying for Mg alloys. Thus, among of these, alloying is an effective manner to improve the mechanical properties and corrosion resistances. The added alloying elements will modified the microstructure of the alloys, including grain size of α-Mg, the secondary phases and the distribution of alloying elements dependent on the fabrication processes. Thus, review the effect of alloying elements on the oxidation behaviors of Mg alloys at high temperature is critical to enlarge their application.

Usually, the alloying elements added in Mg alloys can be classified into two categories: common elements (Al, Zn, Ca) and rare earth (RE) elements (La, Ce, Nd, Y, Er and Gd). When Mg and its alloys are exposed to air at room temperature, they easily react with oxygen to form oxide films. The structure of oxide divided into three layers as shown in Figure 1[7]. It is well known that MgO, as the dominant oxidation product of pure Mg and Mg alloys, has a low Pilling-Bedworth ratio (PBR) of 0.81 less than unity and plays non-protective roles at the temperature above 450℃ [8-9].

The growth rate of Mg oxide is dependent on the outward migration of Mg ions at a certain temperature for the same alloys [10]. The higher the oxidation temperature, the faster the lattice diffusion of Mg ions. This results in the thickening of oxide film. At the same time, the holes will be produced at the matrix/oxide film interface by the accumulation and segregation of these defects, then lead to the cracks at the critical thickness, which further accelerate the diffusion of Mg ions and promote oxidation [11].

Meanwhile, the microstructure and the physical

Received on October 24, 2021; Accepted on December 10, 2021

properties of oxide film formed on the surfaces of Mg alloys during oxidation also affect the oxidation resistance of the alloys oxidized at high temperature. If the oxide films are compact with few defects, i.e., voids and cracks, the oxidation resistance will be improved. When the alloying elements are added in the Mg alloys, the oxides layer on the surfaces should contain the oxides of alloying elements besides MgO as mentioned.

It is well known that the processing of Mg alloy parts has to be experienced of heat-treatment processing, such as casting and deformation (extrusion and rolling), considered the difficult deformation ability at ambient temperature because of few independent slip systems in Mg alloys. So, understanding of alloying elements – oxidation resistance relationships, and the establishment of the database are all very important for the widespread application of Mg alloys.

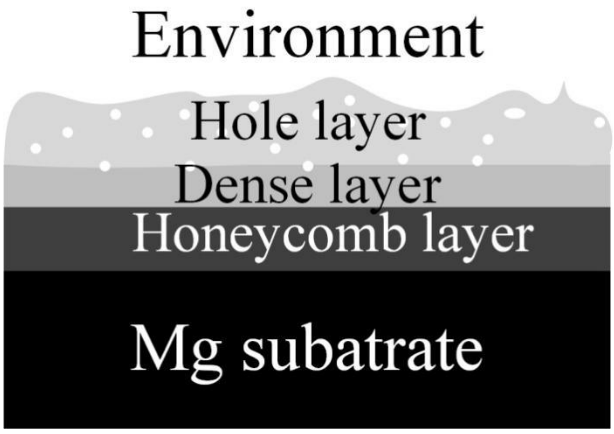

Figure 1 Natural oxide film structure formed on the surface of Mg alloy after oxidation [7]

Hence, the effect of common alloying elements and rare earth elements on the oxidation behaviors of Mg alloys and the research progress of antioxidant Mg alloys are briefly reviewed in this paper.

2 Common Alloying Elements Affect the Oxidation Resistance of Mg Alloys

2.1 Al

Mg-Al serials alloys with good castability, high strength and low price are the most commonly used casting Mg alloys [12-13]. Since the PBR of Al is larger than unity unlike that of Mg aforementioned, the compactness of Al_2O_3 oxide film is better than that of MgO oxide film against the high temperature oxidation [14]. However, it was reported that the oxidation resistance of pure Mg is better than that of Mg-Al alloy at high temperature above the eutectic temperature of Mg-Al alloys mainly due to the low melting point of β-$Mg_{17}Al_{12}$ eutectic phase, in which the β phase is very easy to be evaporated and oxidized therefore caused the poor oxidation resistance [15-16].

The high evaporation rate of Mg described by $K_{evap} = 0.6\ \exp(-25{,}000/RT)\ g/cm^2s$, meaning that the higher the reaction temperature, the more evaporation beats oxidation kinetically. [16] In case of AZ91D alloy, the oxide layers are comprised of the dominant MgO and few of $MgAl_2O_4$. The oxidation mechanism of AZ91D alloy is different at different oxidation temperatures. At temperatures of solid state, the spheroidization and dissolution of second phases take place simultaneously with Al preferential oxidation near the areas enriched in Al, resulting in the high oxidation resistance. However, at the semi-solid temperatures, the incipient melting of the Al-rich fraction, selective evaporation of Mg from liquid islands and condensation within the scale pores and cracks are superimposed on the reaction with oxygen, leading to the weak oxidation resistance.

Barrena [17] reported that weight gain of AZ91 Mg alloys is always higher than that of AM60 through the cyclic oxidation tests at 500-700℃ for 60 min and 540-590℃ for 10 min (Figure 2). This suggests that the oxidation resistance of Mg-Al based alloys is not dependent on only the Al content but the other alloying element addition (Mn and Zn). Conversely, Leontis and Rhines [18] reported that exceeding Al (＞ 1.1 wt.%) addition will accelerate the oxidation rates of Mg not as expected that the addition of Al lower the oxidation rates of Mg alloys. Even at 400℃, over 10 wt.% Al also decrease the oxidation resistance of Mg alloys probably related to the thicker oxide layer [18].

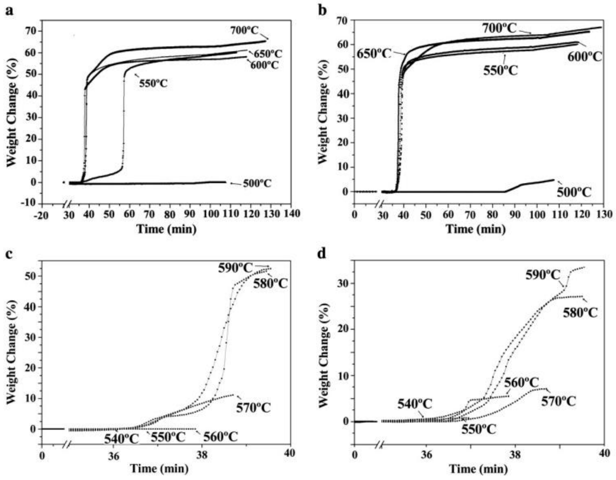

Figure 2 Curves of weight gain versus time for AM60 and AZ91 alloys in air for two different isothermal times: a) AM60 for 1 h, b) AZ91for 1 h, c) AM60 for 10 min and d) AZ91 for 10 min [18]

2.2 Zn

Zn is a useful alloying element in Mg alloys, such as AZ, ZK and Mg-Zn-Y serials alloys, can improve the mechanical properties of Mg alloys by refining the microstructures. However, Zn addition will also reduce the oxidation resistance of pure Mg at high temperature predominantly owing to the following reasons [18]. Firstly, as the melting temperature of Mg-Zn phases is low, a large amount of Mg will evaporate and produce selective oxidation at high temperature [19]; Secondly, Zn is easy to sublimate at high temperature and to penetrate the alloy substrate and oxide film results in the formation of holes at the oxide/alloy interface, which causes the defective oxide films and therefore accelerates the oxidation rate. Although binary Mg-Zn alloy is rarely used because of its instability at high temperature, it has attracted much attention because of its good mechanical properties for the alloys with the other alloying elements additions, such as Mg-Y-Zn alloys, where the oxidation resistance of Mg-Zn alloys was enhanced with the increasing addition of Y (Figure 3) [20].

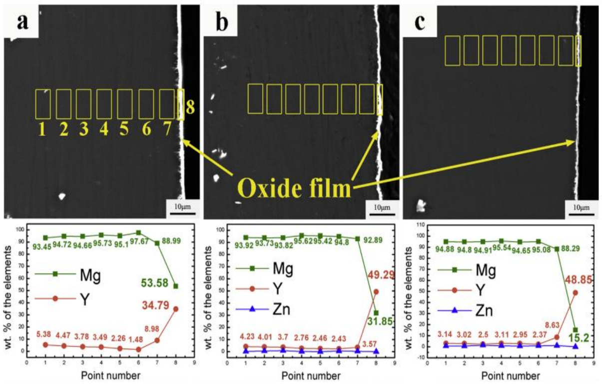

Figure 3 Backscattered electron images of the cross-sectional micrographs of the oxide films of (a) Mg-3Y, (b) Mg-3Y-0.5Zn and (c) Mg-3Y-1Zn alloys with their corresponding EDS analyses of Mg, Y and Zn elements [20]

2.3 Ca

It was found that Ca addition in Mg can lower the oxidation rate at high temperature [21-22]. Small amounts of Ca addition (0.5、1.5 and 3.0 wt.%) decreases the oxidation rates of pure Mg oxidized at 440℃ and 500℃ by thermo-gravimetric experiments, indicating that the addition of Ca is beneficial to the oxidation resistance of pure Mg [21]. However, the oxidation rate of Mg-3Ca alloy is higher than that of Mg-0.5Ca alloy at all tested temperatures. It was explained by the low melting point Mg-Mg_2Ca eutectic structure formed in Mg-Ca alloys with Ca content exceeding 0.5 wt.%, which will be melt leading to a liquid island structure at a higher temperature. Meanwhile, the mass gain results suggested that these liquid islands promote the evaporation of Mg [21]. Further investigation by Auger electron spectroscopy (AES) on the element distribution in the surface layer of alloys after oxidation at 440℃ and 500℃ showed that only MgO layer formed on pure Mg with uniform distribution of Mg and O. However, the element of Ca has been detected on the surface for Mg-3Ca alloy except for MgO. It is also noted that the composition of the oxide layer changed with the different oxidation temperatures. At 440℃, the surface layer consists of the outer Mg oxide layer and the relative inner oxide layer containing Ca. However, when the oxidation temperature reached 500℃, the outer oxide layer is CaO, followed by the mixed oxide layer containing Mg and CaO.

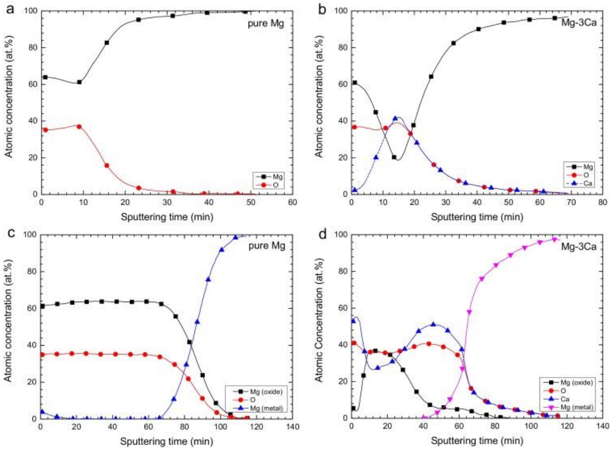

Figure 4 AES depth profiles sputtered from the surface of (a) pure Mg at 440℃; (b) Mg-3Ca at 440℃; (c) pure Mg at 500℃ and (d) Mg-3Ca at 500℃ for 1 h[21]

The improvement in the oxidation resistance of pure Mg by small amounts of Ca addition is possibly related to the following reasons: (1) during the oxidation process, a thin, dense and composite oxide layer composing of CaO and MgO is formed, which plays a good protection roles by hindering the diffusion of O and Mg; (2) the addition of Ca will partially replace Mg in MgO during oxidation process, which increases the density of MgO in the oxide film; (3) The highly thermal-stable second phase formed. Pure Mg alloyed with Ca will produce Mg_2Ca eutectic structure along the grain boundaries. When the oxidation temperature is lower than the melting temperature of Mg-Mg_2Ca eutectic structure, Mg^{2+} ions are difficult to diffuse along the dendritic grain boundaries and therefore inhibit the oxidation.

2.4 Sr

The different ignition temperatures of various Mg-Sr alloys are dependent on the amount of Sr, which is easily segregated to the surface prior to ignition because of its high activity. The ignition temperature of pure Mg is increased by 214℃ from 640℃ of pure Mg to 854 ℃ of Mg-6 wt% Sr alloys. [23] For the high temperature oxidation behavior of Mg–Sr hypoeutectic alloys, a non-uniform two-phase structure oxide scale formed over the interdendritics after oxidation at 500 °C in dry air flow for 12 h.

Note that the secondary phases oxidize primarily causing the formation of MgO and SrO on the surface and continued, which is related to Sr surface activity affecting the initial oxidation sequence. [24] It is highlighted that 75 ppm Sr addition exhibits the similar oxidation resistance of 9 ppm (wt) Be addition in molten AZ91 alloys at 680℃ for 300 min [25], suggesting that Sr could substitute the toxic element of beryllium (Be) usually used in casting of Mg alloys.

3 Oxidation Resistance of Mg Alloyed with Rare Earth Elements

In the past decade, the effect of rare earth (RE) elements on the microstructure, mechanical performance, creep resistance and corrosion resistance of pure Mg has been studied extensively. The addition of RE could enhance the mechanical properties, formability and creep resistance of Mg alloys at high temperature. Furthermore, the addition of RE can improve the oxidation resistance of Mg alloys. Note that the rare earth elements are divided into two subgroups, light rare earth elements and heavy rare earth elements. We will review the effects of light rare earth elements of La, Ce and Nd, heavy metal elements of Gd, Y and Er on the oxidation resistance of Mg alloys.

3.1 Light RE elements

3.1.1 La

As the P-B ratio of La_2O_3 (1.11) is larger than that of Mg [26], the dense oxide layer will be formed on pure Mg by adding of La compared to that of pure Mg, and this can improve the oxidation resistance of Mg alloys. The addition of not only La but La_2O_3 could improve the oxidation resistance of AZ31 Mg alloys, in which the addition of 0.9 wt.% La alloy exhibits the best oxidation resistance of all samples (Figure5) [27]. When the practical La content over 0.9 wt.%, the oxidation resistance of AZ31 is worsened due to the loose and porous oxide film formed and the reduced adhesion to the substrate. As a RE element, the addition of a trace amount of La has a very positive role in improving the oxidation resistance of Mg alloys.

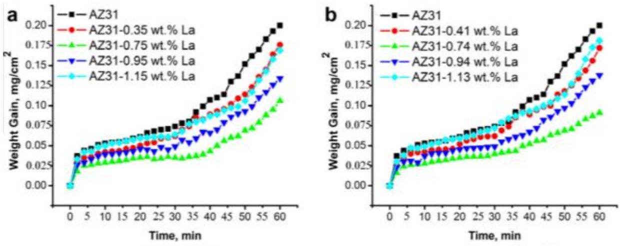

a. AZ31 with La　　b. AZ31 with La_2O_3

Figure 5 Oxidation kinetic curves of AZ31 with both additions. (a) AZ31 with La addition. (b) AZ31 with La_2O_3[24]

3.1.2 Ce

Cerium (Ce) is one kind of light RE elements usually as the alloying elements in Mg alloys. Wang pointed that the Ce addition lowered the mass gained of AZ31 alloy oxidized at 500℃ compared to that of AZ31 alloys [28]. It was found the addition of 0.25 wt.% Ce could increase the ignition points of AZ91 and AM50 alloys by 50℃ primarily ascribed to the dense Ce_2O_3 layer formed [29]. Once this layer is mixed with MgO, the composite oxide film will be denser and be free of defects [30]. However, if the addition of Ce exceeds 0.25 wt.%, the oxidation rate will increase related to the limited solid solubility of Ce in both alloys. The surface morphologies of AM50 alloys with and without Ce addition after oxidation at 500℃ for 1 h were examined shown in Figure 6, where the loose and porous oxide film could be observed on the base alloy. When 0.25 wt.% Ce was added, the surfaces of oxidized alloys were relative smooth with very few holes and defects. Further increasing addition of Ce to 0.45 wt.%, the distinct holes and defects can be seen on the surface of the alloy again (Figure 5C). Thus, a small amount of Ce addition can improve the oxidation resistance of Mg alloy. These dense Ce oxide layer on the surface can protect the substrate from further oxidation. In addition, the existence of Ce in Mg alloy has no adverse effect on mechanical properties. Consequently, from a technical point of view, Ce-containing Mg alloys are worthy of further study.

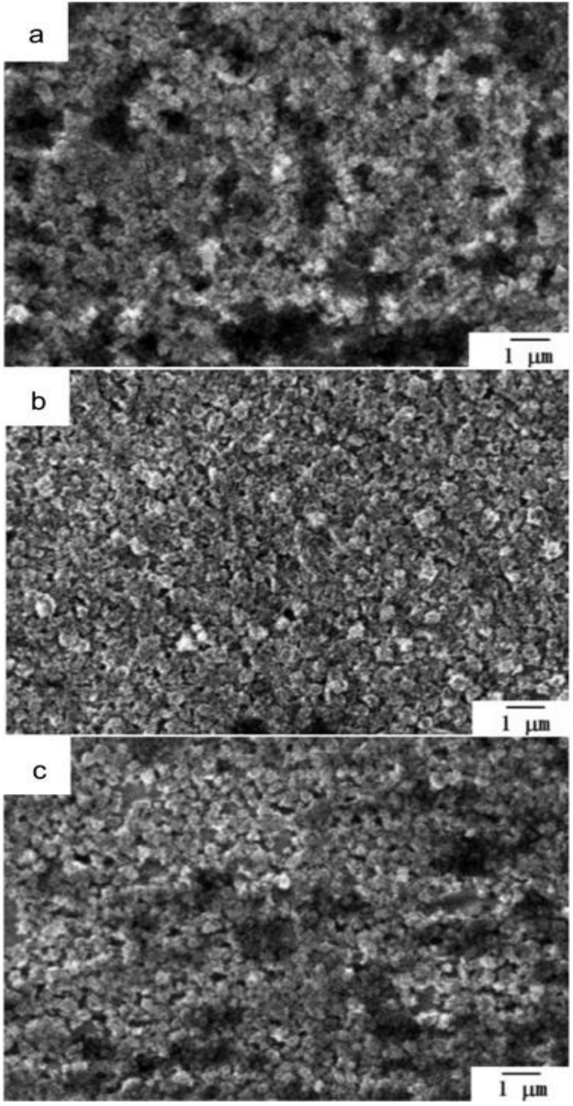

Figure 6 SEM micrographs on the surface of the AM50 Mg alloy after isothermal oxidation in air at 500℃ for 60 min: (a) 0 wt.% Ce with high porosity; (b) 0.25 wt.% Ce showing dense oxide layer; (c) 0.45 wt.% Ce showing porous oxide layer[29]

3.1.3 Nd

To improve the oxidation resistance of alloys, alloying element of Nd could be considered. Small addition (2.87 and 4.5 wt.%) of Nd can improve oxidation resistance of Mg oxidized at 500℃, while the oxidation resistance decreased significantly when Nd content is 11.2 wt.% and 25 wt.%, which are related to the cracks or pores on the surfaces of alloys during oxidation (Figure7) [31-32]. Moreover, MgO will be formed prior to Nd_2O_3 at the initial stage during oxidation via thermodynamic calculation. The initially formed MgO reduces the content of Mg elements on the surface of α-Mg as shown in Figure 8. Correspondingly, the surface activity of Nd increases leading to the formation of Nd_2O_3 [33]. As the PBR ratio of Nd_2O_3 is 1.13 [34], the dense composite oxide film can effectively protect the alloy matrix from further oxidation.

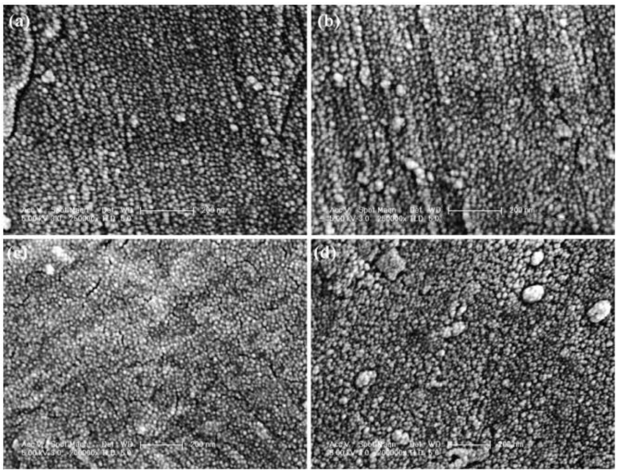

Figure 7 Surface morphologies of MgNd alloys (Nd = 25 wt.%) oxidized in pure O_2 up to 90 min at (a) 723 K, (b) 773 K, (c) 823 K and (d) 873 K[33]

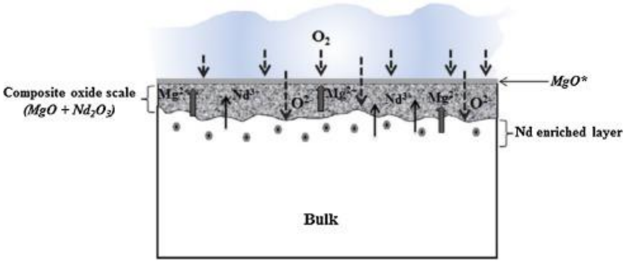

Figure 8 The schematic depiction of the oxidation in dilute Mg–Nd alloys at 500℃ for 12 h in dry air [33]

The oxidation mechanism of Nd in ternary Mg alloy is very complex. Arrabal highlighted that 1.4 wt.% Nd addition could improve the oxidation resistance of AZ91D alloys at 410℃, where the oxidation rate of Nd-containing alloy is 72% compared to the base alloy [35-36]. The improvement can be interpreted by the increasing volume of Al-Nd intermetallic compounds and the decreasing of $Mg_{17}Al_{12}$ phase by Nd addition as shown in Figure 9 (a) and (b). Compared with other rare earth elements, Nd is an ideal addition element that can protect Mg alloy from oxidation. The oxidation kinetics curves of Mg-Nd (Nd = 25 wt.%) alloy follow the parabolic oxidation at 723-873K. [31] The oxide layers show a triplex structure: the outer layer is composed of MgO, Nd_2O_3 and $Nd(OH)_3$, the middle layer chiefly consists of MgO and Nd_2O_3, and the inner layer is made of MgO, Nd_2O_3 and the content of the substrate, where the Nd_2O_3/MgO layer contributed to the high oxidation resistance of Mg-Nd alloys acted as a barrier to retard the outward Mg^{2+} diffusion.

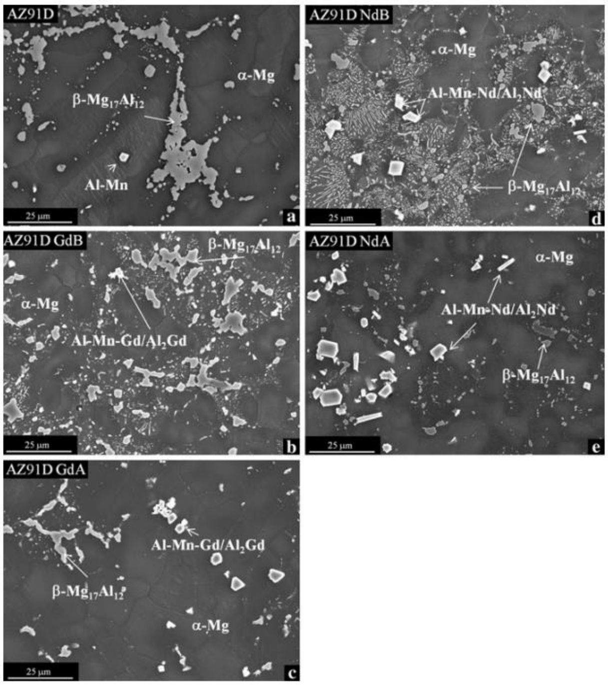

Figure 9 SEM micrograph of AZ91D (a) AZ91D, (b) AZ91D-0.2Gd, (c) AZ91D-0.7Gd, (d) AZ91D-0.7Nd and (e) AZ91D-1.4Nd[36]

3.2 Heavy RE elements

3.2.1 Gd

Gd is one kind of heavy RE elements, which often was used as an alloying element in improving mechanical properties of Mg alloys. Moreover, it can also improve the oxidation resistance of Mg alloys [18]. Arrabal [37] concluded that the 0.7 wt.% Gd addition can improve the oxidation resistance of AZ91 alloy because the addition of Gd could effectively suppress the formation of unstable $Mg_{17}Al_{12}$ phase during casting. Liu et al. [38] studied the oxidation resistance of Mg-Gd-Y-Zr alloy in oxygen or mixed gas of oxygen and water vapor in the temperature range of 230℃ to 300℃. It was found that weight gain is negligible after exposure to the atmospheres for 10 h, meaning that the oxidation rate of Mg alloy containing Gd and Y is low in contrast with the matrix.

The good oxidation resistance is that the surface is composed of MgO, Y_2O_3 and Gd_2O_3, which hinders the diffusion of Mg and further protects the alloy from further oxidation. Wang et al. [39] studied the high temperature oxidation behaviors of Mg-10Gd-3Y alloy. The oxidation kinetics curves follow the parabolic law but not linear even oxidation at 600℃ for 90 min as shown in Figure 10, indicating that this protection is also applicable to semi-molten alloys due to the protective effect of Y and Gd additions.

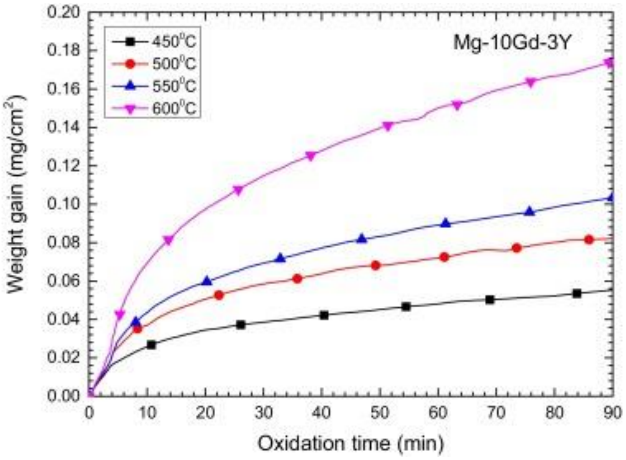

Figure 10 Weight gain curves of the Mg–10Gd–3Y alloys oxidized at 450-600℃ for 90 min [39]

Kim [36] attributed the better oxidation resistance of Gd-containing Mg alloys to its high solid solubility (23.5 wt.%) in Mg. With the increasing temperature, the solute concentration in the matrix increases due to the dissolution of the intermetallic phases. Moreover, the high solid solubility of Gd in Mg promotes the formation of dense layer during the oxidation process, and therefore improves the oxidation resistance. Thus, it is an effective method to develop a new Mg alloys via Gd addition. And these alloys show the desirable oxidation and flame resistance, which can be used at high temperature in future.

3.2.2 Y

The effect of various addition of Y on the Mg alloys has been studied [40-42]. For Y containing Mg alloys during oxidation, the following reactions are possible occur. [43]

$$2Mg + O_2\,(g) = 2MgO \qquad (1)$$

$$2Y + 3/2\,O_2\,(g) = 2Y_2O_3 \qquad (2)$$

$$2Y + 3MgO = Y_2O_3 + 3Mg \qquad (3)$$

The calculated results show that the element Y is much more active than Mg, the selection oxidation of Y is very possible due to the larger affinity of Y with O, and the outward diffusion of Y accelerating with the increasing temperature based on reaction (3), that makes MgO deoxidize associated with the formation of Y_2O_3 as the outer layer oxide film. Yu attributed the improved oxidation resistance of Mg with 3.7 wt.% Y addition to a composite oxide film of Y_2O_3 and MgO (Figure 11). Further investigation by XPS shows that Y_2O_3 is mainly concentrated in the inner layer (Figure12). However, 8 wt.% Y addition cause the significant embrittlement [43-44]. For $Mg_{3.08}Y_{0.68}Ce$ alloy oxidized at 673 and 773 K, The oxidation dynamics curve follow the parabolic-line law, which can be fitted as:

$x^2 + 3.38308\,x = -2.92579 + 0.02548\,t$, R-square = 0.99963, for T= 673 K, and

$x^2 + 1.08078\,x = -1.03408 + 0.03089\,t$, R-square = 0.99920, for T= 773K, where t and x represent the time and mass gained, respectively. [43]

Except single Y addition, combination Y and Al addition in Mg alloys demonstrates that the addition of Al exceeds 2.5 wt.% could improve the oxidation resistance of Mg-2.5Y alloys. For low Al addition (＜ 2.5 wt.%), the oxidation resistance of alloys is weak due to the high-melting-point Al_2Y formed during casting that inhibits the formation of Y_2O_3 on the surface [43]. While for high Al addition (＞ 2.5 wt.%), the oxidation resistance is better owing to the compact Al_2O_3 films formed on the surface by the reaction between the remaining Al and oxygen during oxidation, and hindered the diffusion of Mg and O ions.

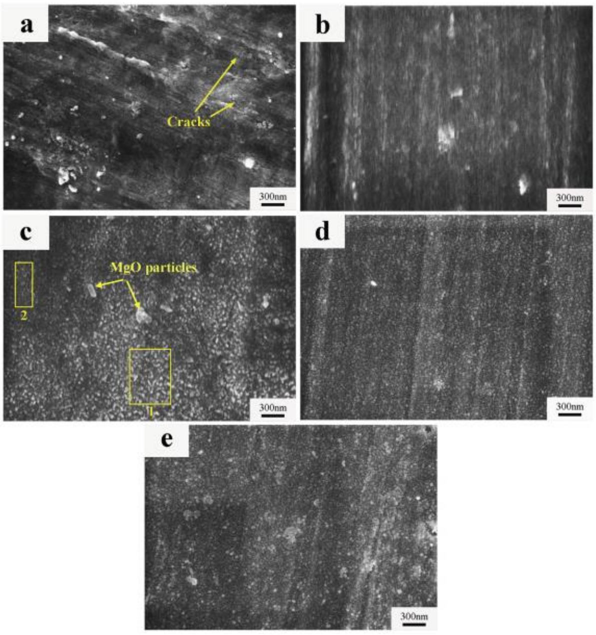

Figure 11 Surface morphologies of (a) Mg-0.5Y, (b) Mg-1.0Y, (c) Mg-1.7Y, (d) Mg-3.7Y and (e) Mg-5.5Y alloys oxidized at 550℃ for 6 h in dry air [40]

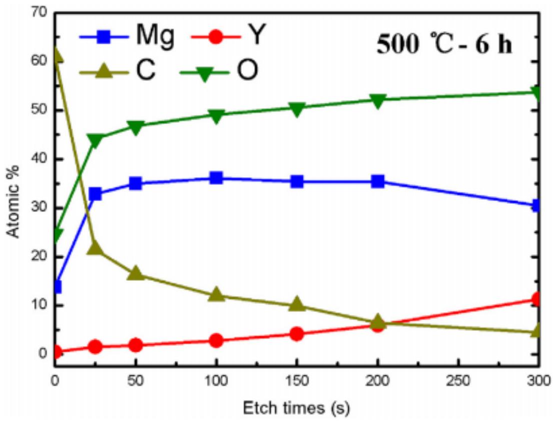

Figure 12 The variation in the atomic contents of elemental Mg, O, Y, and C along the depth direction in the oxide film of Mg-3.7Y alloy [40]

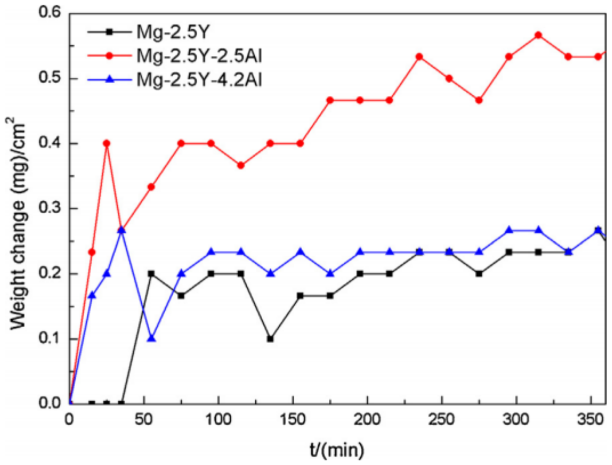

Figure 13 The weight gain curves of Mg–2.5Y, Mg–2.5Y–2.5Al and Mg–2.5Y–4.2Al alloys oxidized at 500℃ for 360 min in the dry air [43]

3.2.3 Er

Few studies evaluated the oxidation behaviors of Mg-Er Mg alloys at high temperature compared to Mg-Al and Mg-Y alloys. The Er_2O_3 in the intermediate layer and the dense fine-grained Er_2O_3 in the inner layer dominantly improve the oxidation resistance of Mg alloys. Additionally, the impurities Ca in the matrix generated the discontinuous CaO in the outer layer hardly affect the oxidation resistance of alloys. And the schematic diagram of the multi-layer oxide film structure shown in Figure 14 (a)～(d).

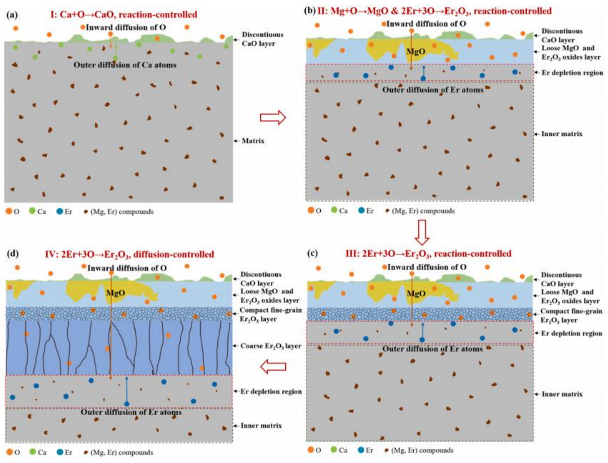

Figure 14 Schematic diagrams of multi-layered oxide film structures formed on the Mg-8Er alloys at 500℃ in air[44]

4 Conclusions

Oxidation resistance is a critical issue for Mg alloys because the oxidation is not inevitable during fabricating and processing of these alloys due to its high affinity with O. Alloying is an effective manner to improve the oxidation resistance of Mg and its alloys. Hence, the effect of alloying elements (Al, Zn, Ca, Sr, La, Ce, Nd, Y, Gd and Er) on the oxidation resistance of Mg and Mg alloys was addressed. The conclusion and the future development were given as follows.

(1) For common alloying elements, the proper addition of Al, Ca and Sr is beneficial to improve the oxidation resistance of Mg alloys, while the addition Zn will decrease the oxidation resistance.

(2) With respect to the rare earth elements X (X: La, Ce, Nd, Gd, Y and Er), small amounts of addition of X enhance the oxidation resistance of Mg alloys related to their solubility in Mg, the relative large PBR compared to that of Mg and the compact X_2O_3 film formed on the surface. These factors work together to improve the oxidation resistance of Mg alloys.

(3) Combination additions of common alloying elements with rare earth elements can further enhance the oxidation resistance of Mg alloys compared to those of binary Mg alloys.

(4) Tailoring the alloying elements added in Mg alloys should be careful because these elements are favorable to strengthen the mechanical properties, the formability and the corrosion resistance in ambient surroundings. How to coordinate these factors among the alloying elements should be further studied as well as the other alloying elements, such as Sr, Mn, Sm and Sn and so on, also should be further investigated to enlarge the applications of Mg alloys.

References

[1] CD. Barrett, A. Imandoust, AL. Oppedal. Effect of grain boundaries on texture formation during dynamic recrystallization of magnesium alloys, Acta Mater. 2017 (128): 270–283.

[2] J. Buha. Mechanical properties of naturally aged Mg–Zn–Cu–Mn alloy, Mater. Sci. Eng. A 2008 (489): 127–137.

[3] J. J. Jeon, S. W. Lee, B. H. Kim. Effect of Sb and Sr addition on corrosion properties of Mg–5Al–2Si alloy, Korean J. Met. Mater. 2008 (46): 304–309.

[4] S. Tekumalla, M. Gupta. An insight into ignition factors and mechanisms of magnesium based materials: a review, Mater. Design. 2017 (113): 84–98.

[5] M. Gobara, M. Shamekh, R. Akid. Improving the corrosion resistance of AZ91Dmagnesium alloy through reinforcement with titanium carbides and borides, J. Magn. Alloys 2015 (3): 112–120.

[6] A. Atrens, G. L. Song, M. Liu. Review of recent developments in the field of magnesium corrosion, Adv. Eng. Mater. 2015 (17): 400–453.

[7] G.L. Makar, J. Kruger. Corrosion of magnesium, Int. Mater. Rev. 1993 (38): 138–153.

[8] Q. Y. Tan, A. AtrensTan, N. Mo. Oxidation of magnesium alloys at elevated temperatures in air: A revie, Corros. Sci. 2016 (112): 734–759.

[9] F. Czerwinski. The reactive element effect on high-temperature oxidation of magnesium, Int. Mater. Rev. 2015 (60): 264–296.

[10] P. Kofstad. High temperature corrosion, Elsevier Applied Science Publisher Ltd., 1988

[11] F. Czerwinski. Z. Kedzierski. On the mechanism of

microcrack formation in nanocrystalline Fe-Ni electrodeposits, J. Mater. Sci. 1997 (32): 2957-2961.

[12] I.J. Polmear, Light Alloys, third ed., Arnold, London, 1995.

[13] A. Luo, M.O. Pekguleryuz. Cast magnesium alloys for elevated temperature applications, J. Mater. Sci. 1994 (29): 5259–5271.

[14] J. Jedlinski, G. Borchardt. On the oxidation mechanism of alumina formers, Oxid. Met. 1991 (36): 317–337.

[15] J. Medved, P. Mrvar, M. Vonˇcina. Oxidation resistance of cast magnesium alloys, Oxid. Met. 2009 (71): 257–270.

[16] F. Czerwinski. The oxidation behaviour of an AZ91D magnesium alloy at high temperatures, Acta Mater. 2002 (50): 2639–2654.

[17] M. Barrena, J. Gomez de Salazar, L. Matesanz, A. Soria. Effect of heat treatment on oxidation kinetics in AZ91 and AM60 magnesium alloys, Mater. Charact. 2011 (62): 982–986.

[18] T. Leontis , F. Rhines. Rates of high temperature oxidation of magnesium and magnesium alloys, Trans. Amer. Inst. Min. (matall.) Engrs. 1946 (166): 265–294.

[19] Huang H, Yuan G Y, Chu Z H, et al., Microstructure and mechanical properties of double continuously extruded Mg-Zn-Gd-based magnesium alloys, Mater. Sci. Eng.: A 2013 (560): 241–248.

[20] Yu X, Jiang B, He J,et al., Effect of Zn addition on the oxidation property of Mg-Y alloy at high temperatures, J. Alloy. Compd. 2016 (687): 252–262.

[21] You B S, Park W.W, Chung I S. The effect of calcium additions on the oxidation behavior in magnesium alloys, Scr. Mater. 2000 (42): 1089–1094.

[22] Cheng s, Yang G, Fan J, et al., Effect of Ca and Y additions on oxidation behavior of AZ91 alloy at elevated, T. Nonferr. Metal. Soc. 2009 (19): 299–304.

[23] D.S. Aydin, Z. Bayindir, M.O. Pekguleryuz. High temperature oxidation behavior of hypoeutectic Mg-Sr binary alloys: the role of the two-Phase microstructure and the surface activity of Sr, Adv. Eng. Mater. 2015 (17): 697–708.

[24] D.S. Aydin, Z. Bayindir, M.O. Pekguleryuz. The effect of strontium (Sr) on the ignition temperature of magnesium (Mg): a look at the pre-ignition stage of Mg–6 wt% Sr, J. Mater. Sci. 2013 (48): 8117–8132.

[25] M. Pekguleryuz, P. Vermette. Strontium for melt oxidation reduction ofmagnesium and a method for adding strontium to magnesium, US Patent Application, US20040159188 A1, 2004.

[26] H.S. Kim, Y.M. Kim, C.D. Yim, et al., Key factor influencing the ignition resistance of magnesium alloys at elevated temperatures, Scripta Mater. 2011 (65): 958–961.

[27] Zhao S, Zhou H, Zhou T, et al., The oxidation resistance and ignition temperature of AZ31 magnesium alloy with additions of La2O3 and La, Corros. Sci. 2013 (67): 75–81.

[28] Wang X.M, Zeng X Q ,Wu G S, et al., The effects of cerium implantation on the oxidation behavior of AZ31 magnesium alloys, J. Alloys Compd. 2008 (456): 384–389.

[29] Lin P, Zhou H, Li W, et al., Interactive effect of cerium and aluminum on the ignition point and the oxidation resistance of magnesium alloy, Corros. Sci. 2008 (50): 2669–2675.

[30] Li W P, Li W, Zhou H, et al., Effect of cooling rate on ignition point of AZ91D-0.98 wt.% Ce magnesium alloy, Mater. Lett. 2007 (61): 2772–2774.

[31] Wang X.M, Zeng X Q ,Wu G S, et al., Surface oxidation behavior of MgNd alloys, Appl. Surf. Sci. 2007 (253): 9017–9023.

[32] D.S. Aydin, Z. Bayindir, M. Hoseini, et al., The high temperature oxidation and ignition behavior of Mg–Nd alloys part I: the oxidation of dilute alloys, J. Alloys Compd. 2013 (569): 35–44.

[33] D.S. Aydin, Z. Bayindir, M.O. Pekguleryuz. The high temperature oxidationbehavior of Mg–Nd alloys. Part II: the effect of the two-phase microstructureon the on-set of oxidation and on oxide morphology, J. Alloys Compd. 2014(584): 558–565.

[34] N.B. Pilling, R.E. Bedworth. The oxidation of metals at high temperatures, J. Inst. Met. 1923 (29): 529–591.

[35] G.L. Makar, J. Kruger. Corrosion of magnesium, Int. Mater. Rev. 1993 (38): 138–153.

[36] R. Arrabal, A. Pardo, M.C. Merino, et al., Oxidation behavior of AZ91D magnesium alloy containing Nd or Gd, Oxid. Met. 2011 (76): 433–450.

[37] D.S. Aydin, M. Hoseini, M.O. Pekguleryuz. Understanding the hightemperature oxidation and ignition behaviour of two-phase Mg-Nd alloysand a comparison to single phase Mg-Nd, Philos. Mag. 2015 (95): 259–274.

[38] Liu J, Li Y, Wang F. The high temperature oxidation behavior of Mg–Gd–Y–Zr alloy, Oxid. Met. 2009 (71): 319–334.

[39] Wang X, Wu W, Tang Y, et al., Early high temperature oxidation behaviors of Mg–10Gd–3Y alloys, J. Alloys Compd. 2009 (474): 499–504.

[40] Yu X W, Jiang B ,He J J, et,al., Oxidation resistance of Mg-Y alloys at elevated temperatures and the protection performance of the oxide films, J. Alloy Compd. 2018 (749): 1054–1062.

[41] Fan J F, Cheng S.L, Xie H, et al., Surface oxidation behavior of Mg-Y-Ce alloys at high temperature, Metall. Mater. Trans. A 2005 (36): 235-239.

[42] Fan J F, Yang G C, Chen S L,et al, Effect of rare earths (Y, Ce) additions on the ignition points of magnesium alloys, J. Mater. Sci. 2004 (39): 6375-6377.

[43] Yu X, Shen S, Jiang B, et al., The effect of the existing state of Y on high temperature oxidation properties of magnesium alloys, Appl. Surf. Sci. 2016 (370): 357–363.

[44] Wu J J, Yuan Y, Yang L, et al., The oxidation behavior of Mg-Er binary alloys at 500℃, Corros. Sci. 2022 (195): 109961.

Viser Technology Pte. Ltd.
Research and Application of Materials Science
DOI: 10.33142/rams.v3i2.6733

Research Article Open Access

Role of Heat Treatment Temperatures on Mechanical Properties and Corrosion Resistance Properties of Mg-10.16Li-8.14Al-1.46Er alloy

Shuhao LIU, Xiaoyang QIAN, Yun ZOU*

School of Mechanical and Power Engineering, Zhengzhou University, Zhengzhou, China

***Corresponding Author:** *Yun ZOU, No. 100, Science Avenue, High-tech Zone, Zhengzhou City, Henan Province, Zhengzhou 450001, China; yunzou@zzu.edu.cn*

Abstract:
The microstructure and phase evolution of Mg-10.16Li-8.14Al-1.46Er alloy of as-cast, 250℃+12 h, 300℃+12 h, and 400℃+12 h were studied by optical microscopy, scanning electron microscope, and X-ray diffraction. The mechanical properties of Mg-10.16Li-8.14Al-1.46Er alloy in different states were tested by microhardness tester and tension tester. The corrosion resistance of Mg-10.16Li-8.14Al-1.46Er alloy in different states was measured by electrochemical workstation combined with hydrogen evolution and mass loss tests. The results show that the microstructure of as-cast Mg-10.16Li-8.14Al-1.46Er alloy consists of α, β, AlLi, Al_3Er and $MgAlLi_2$ phases. Changes of microstructure are morphology and quantity of α phase, and second phases of $MgAlLi_2$ and AlLi by heat treatments at different temperatures. The best comprehensive tensile properties of Mg-10.16Li-8.14Al-1.46Er at 400℃ are attributed to the α phase structure, solution strengthening and second phase strengthening. After heat treatments at different temperatures, the corrosion resistance of Mg-10.16Li-8.14Al-1.46Er was improved compared with as-cast samples. The Mg-10.16Li-8.14Al-1.46Er alloy has the best corrosion resistance at 250℃ due to the best homogenization at this temperature.

Keywords: *Ultralight Mg-Li alloy; Microstructure; Heat treatments; Mechanical properties; Corrosion resistance properties*

1 Introduction

In the 21st century, with the energy crisis and the environmental crisis, energy conservation and emission reduction have become the universally recognized way of development. Lightweight has become one of the main development ways of energy conservation and emission reduction. It is essential to refer to the lightweight of materials. Mg alloys are the lightest of all structural metals ($\rho \sim 1.74$ g cm^{-2}). Adding lithium (Li) to magnesium (Mg) can form ultralight Mg-Li alloy to further reduce the density of Mg alloys [1-3]. Meanwhile, the problem of difficult deformation of Mg alloys is solved, so Mg-Li alloys are widely used in 3C, medical treatment, automotive electronics and aerospace [4-5]. However, poor corrosion resistance and low strength are still the main problems hindering its large-scale application [6-9]. It is urgent to improve the mechanical and corrosion resistance properties of Mg-Li alloys.

Microstructure determines the properties of materials. To improve the properties of Mg-Li alloy, the most basic is to design the alloy from the angle of alloy casting, so as to obtain the desired microstructure composition. Therefore alloying is a traditional method used to improve the properties of Mg-Li alloy. The addition of Al in Mg-Li alloy can improve the strength of Mg-Li alloy through solution strengthening and dispersion strengthening [10-11]. As for its influence on corrosion resistance, it is reported that the addition of Al will reduce the polarization resistance of Mg-Li alloy, which is detrimental to the corrosion resistance [10]. However, our previous study found that the alloying element Al formed in the Mg-Li alloy presents a refined distribution AlLi phase, which is beneficial to the corrosion resistance of Mg-9Li-6Al alloy [12]. Rare earth elements can significantly improve the strength of Mg-Li alloy through solid solution strengthening and second phase strengthening of forming intermetallic compounds [13-16]. The addition of rare earth element Er can effectively reduce grain size, and appropriate rare earth element Er content makes Mg-10Li-5Zn-0.5Er alloy exhibit the best mechanical properties [17].

Alloying endows the material with a set structure and composition. On the basis of alloying, appropriate heat treatment is applied to adjust the grain size and phase structure and distribution, which can significantly affect

Received on October 2, 2021; Accepted on December 19, 2021

its mechanical and corrosion resistance [18-21]. This is also an important reason why heat treatment is applied in the field of various metal materials. On the other hand, the deformation process of Mg-Li alloy is one of the main strategies applied to improve the performance of Mg-Li alloy [22]. Due to the difficulty of Mg alloys deformation, large deformation will lead to the cracking and micro-cracking of Mg alloy after processing, and seriously affect its service life. Therefore, before the deformation strengthening of Mg-Li alloy, proper heat treatment of the as-cast Mg-Li alloy is needed to improve its machining properties by homogenizing the structure composition, so as to effectively carry out deformation strengthening. Different heat temperatures have different effects on heating treatments. So it is necessary to study the properties and mechanism of properties change of Mg-Li alloy caused by different heat temperatures.

In this paper, as-cast Mg-10.16Li-8.14Al-1.46Er alloy is taken as the research object. For controlling the same heating time, the effects of different heating temperatures on the microstructure, mechanical properties and corrosion resistance properties of Mg-Li alloy are studied. On the one hand, it is expected to improve the properties of Mg-Li alloy through different heating temperatures. On the other hand, it is expected to be a reference for the selection of homogenizing heat treatment temperature of Mg-Li alloy before deformation processing.

2 Material and Methods

2.1 Specimen preparation

The cast Mg-10.16Li-8.14Al-1.46Er ingots were fabricated at the Zhengzhou Light Metals Research Institute of Aluminum Corporation of China Limited (Henan, China). In order to avoid the risk of oxidation at high temperature, the samples were wrapped in tinfoil paper. The heating temperatures were set at 250℃, 300℃, and 400℃, and the heating time was set as 12 h. Water quenching was carried out immediately after the heat treatment.

2.2 Material characterization

2.2.1 Microstructure characterization

After mechanical polishing and washing, samples were etched using a 4 vol.% nitric acid alcohol solution. Then, the microstructure was observed by VHX-2000 optical microscopy (OM) (Keyence, Osaka, Japan) or an Auriga-bu scanning electron microscopy (SEM) (Zeiss, Jena, GER) with the acceleration voltage of 5 kV. The phase evolution was analyzed by Empyrean X-ray diffraction (XRD) technology (Malvenpanako, NL, USA). The voltage and current were 45 kV and 40 mA, respectively. The diffraction angle (2θ) ranged from 20° to 80 °.

2.2.2 Mechanical properties characterization

The hardness test force of samples in different heat treatment states is 0.5 N, and the load time is maintained for 10 s by HV-1000 Vickers microhardness tester (Beijing Times Mountain Peak Technology, Beijing, CN) with the size of samples was 10×10×2 mm. The tensile test was carried out on a MTS370.25 tension tester (MTS Systems Corporation, Minnesota, USA) with a displacement rate of 1.5 mm/min. The gauge length, width, and thickness of the tensile specimens were 25, 10 and 2 mm, respectively.

2.2.3 Corrosion resistance characterization

The corrosion resistance of the samples was characterized by polarization curve test, hydrogen evolution test and mass loss test. The polarization curve test was tested using an RST5200F electrochemical workstation (Zhengzhou SRIS Instrument Technology, Zhengzhou, CN), in which the working electrode was the test samples, the platinum plate was the counter electrode, and the saturated calomel electrode was the reference electrode. The samples were immersed in 3.5 wt. % NaCl solution with an exposure area of 1 cm^2. The polarization measurements started from −0.15 V to 0.15 V (relative to the open circuit potential) with a scanning rate of 0.5 mV/s. In order to directly compare the corrosion rate measured by electrochemical test with hydrogen evolution test and mass loss test, the results were characterized by annual corrosion rate.

The corrosion current density i_{corr} (mA cm^{-2}) is related to the corrosion rate P_i (mm y^{-1}) and the conversion equation [18,23,24]:

$$P_i = 22.85 i_{corr} \tag{1}$$

For hydrogen evolution test, the samples were immersed in 3.5wt. % NaCl solution (exposure area was 2 cm^2) for 72 h. The mass W_1 of the sample was recorded before the test, and the volume change was recorded every hour during the test. After the immersing, the samples were immersed in 180 g/L CrO_3 solution for 5 min and cleaned by ultrasound. Weigh and record W_2 after removing corrosion products. The hydrogen evolution volume rate V_H (mm cm^{-2} d^{-1}) was converted to corrosion rate P_H (mm y^{-1}), and the conversion equation was obtained [18,23,24]:

$$P_H = 2.279 V_H \tag{2}$$

Mass loss rate $\triangle W_m$ (mg cm^{-2} d^{-1}) is converted to corrosion rate P_W (mm y^{-1}), the conversion equation [18,23,24]:

$$P_W = 2.10 \Delta W_m \tag{3}$$

3 Results

3.1 Microstructure

The microstructures of Mg-10.16Li-8.14Al-1.46Er before and after different heat treatments were shown in Figure 1. The microstructures of all samples were characterised by the α phase, β matrix phase and black second phase particles, which the composition of the main phases does not change.However, it is observed that the α phase changes to a smaller and elongated direction at 250℃ compared with the as-cast sample. Changes of α phase are more obvious at 300℃, and the distribution of α phase is fine at grain boundaries (GBs). The second black phase particles are decreased obviously. When heating temperatures at 400℃, the microstructure changes particularly obvious as showed in Figure 1d. The α phase distributed at the GBs shows a trend of spheroidization increasing along the GBs, while the number of α phase decreases. Then the α phase on the β phase matrix shows a relatively fine distribution. The second black phase particles are basically disappeared.

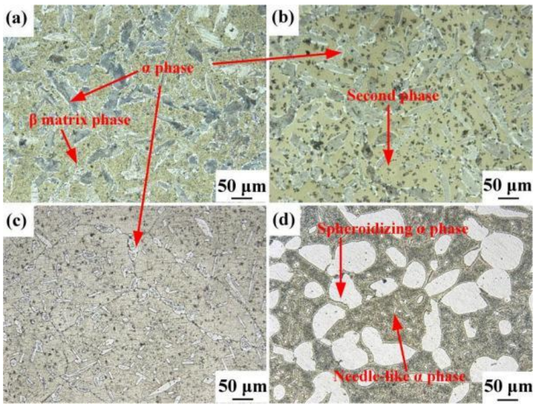

Figure 1 The microstructure of Mg-10.16Li-8.14Al-1.46Er alloy (a) As-cast, (b) 250℃, (c) 300℃, and (d) 400℃

Figure 2 shows the XRD patterns of Mg-10.16Li-8.14Al-1.46Er alloy before and after different heat treatments. The diffraction peaks of as-cast Mg-10.16Li-8.14Al-1.46Er alloy includes α phase, β phase, AlLi phase, Al_3Er and $MgAlLi_2$ phase. When the heating temperature is 250℃, the composition of the main phase does not change, but the diffraction peaks of the $MgAlLi_2$ phase almost disappear, which is consistent with the results of microstructure. However, diffraction peaks of $MgAlLi_2$ phase were reappeared again at 300℃, and the intensity of $MgAlLi_2$ phase diffraction peak increases at 400℃, the diffraction peaks of AlLi phase were disappeared. In other words, the changes of Mg-10.16Li-8.14Al-1.46Er alloy after different heat treatments were mainly the second phases.

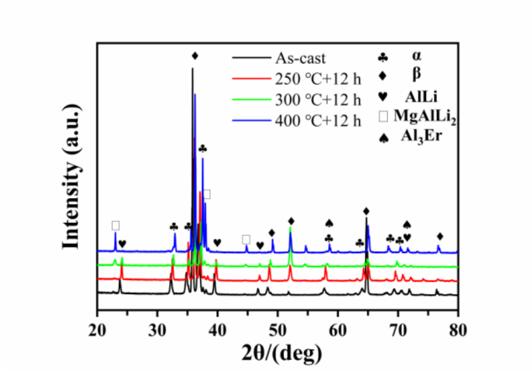

Figure 2 XRD patterns of Mg-10.16Li-8.14Al-1.46Er alloy

3.2 Mechanical properties

3.2.2 Microhardness

The hardness of Mg-10.16Li-8.14Al-1.46Er alloy before and after different heat treatments was shown in Figure 3. The hardness of Mg-10.16Li-8.14Al-1.46Er alloy was increased by different heat treatments and the changes of hardness value were attributed to microstructure. Combined with the analysis of microstructure and XRD patterns, the $MgAlLi_2$ phase disappears at 250℃, while the $MgAlLi_2$ phase is a metastable precipitation phase, which is easy to decompose and produce AlLi phase, thus resulting in softening effect [25-26]. However, the hardness value increased significantly at 250℃, and the peak strength of AlLi at 250℃ did not increase, which indicating that part of AlLi phases were solidly dissolved into the matrix, thus producing a solid solution strengthening effect. The hardness value of samples at 300℃ was 15% higher than as-cast samples. However, hardness value of 300℃ was lower than hardness value of 250℃. This is likely due to the refinement of α phase, which increases the proportion of the softer β matrix phase, resulting in a decrease in hardness. XRD patterns show that $MgAlLi_2$ phase is precipitated again, diffraction intensity of AlLi phase decreased. Therefore, the strengthening effect was attributed to precipitation strengthening and solid solution strengthening. The hardness of samples at 400℃ was 23.8% higher than as-cast samples. In this condition, the diffraction peak intensity of $MgAlLi_2$ phase was further enhanced and the diffraction peaks of AlLi phases disappear, which means that stronger precipitation strengthening and solid solution strengthening occur at this temperature. Therefore, the hardness values increases remarkably.

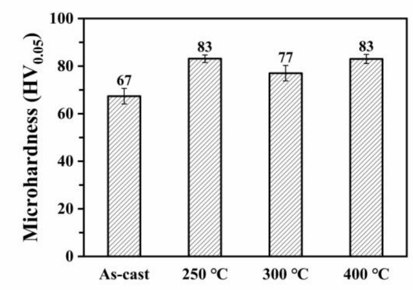

Figure 3 Microhardness of the Mg-10.16Li-8.14Al-1.46Er alloy

3.2.2 Tensile properties

Figure 4 is the engineering stress-strain curves of the Mg-10.16Li-8.14Al-1.46Er alloy before and after different heat treatments, and the tensile mechanical related parameters are summarized in Table 1. The tensile strength (UTS) of Mg-10.16Li-8.14Al-1.46Er alloy of as-cast, 250℃, 300℃ and 400℃ was 180, 221, 237 and 226 MPa, respectively. The yield strength (YTS) was 151, 180, 225 and 198 MPa, respectively. The fracture elongation (E_f) was 3.0, 3.1, 1.4 and 4.8%, respectively. The UTS of Mg-10.16Li-8.14Al-1.46Er alloy at 250℃

was 22.8% higher than as-cast samples. However, the E_f does not change significantly compared to the strength. The UTS of Mg-10.16Li-8.14Al-1.46Er alloy at 300℃ was 31.7 % higher than as-cast samples, but the plastic loss is serious. The UTS of samples at 400℃ was 25.6% higher than as-cast samples and the E_f was highest.

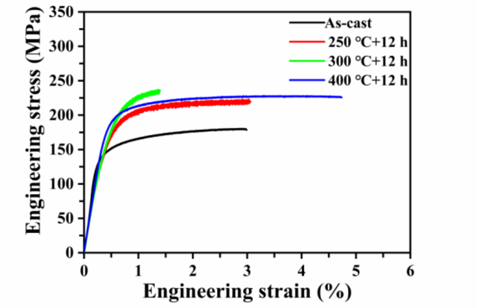

Figure 4 Engineering stress-strain curve of Mg-10.16Li-8.14Al-1.46Er alloy

Table 1 Tensile mechanical properties of Mg-10.16Li-8.14Al-1.46Er alloy

Sample	As-cast	250℃	300℃	400℃
TYS (MPa)	151	180	225	198
UTS (MPa)	180	221	237	226
E_f (%)	3.0	3.1	1.4	4.8

3.3 Corrosion resistance

Figure 5 is the polarization curves of Mg-10.16Li-8.14Al-1.46Er alloy. The corrosion potentials of samples of as-cast, 250℃, 300℃ and 400℃ were −1.61 V, −1.62 V, −1.58 V and −1.57V, respectively as showing in Figure 5b. The corrosion potential reflects the corrosion tendency of samples, which the more negative of the corrosion potential, the greater of the corrosion tendency. According to the corrosion potential value, the samples at 300℃ had the smallest corrosion tendency. However, the corrosion tendency represented by corrosion potential has no relation with the actual corrosion rate, and the corrosion current density determines the corrosion rate of the samples. The corrosion current density of Mg-10.16Li-8.14Al-1.46Er alloy of as-cast, 250℃, 300℃ and 400℃ was 1.25×10^{-1}, 1.19×10^{-1}, 0.79×10^{-1} and 0.6×10^{-1} mA • cm^{-2}, respectively. Then the order of corrosion rates from low to high was: 400℃＜300℃＜ 250 ℃＜ as cast. This means that the corrosion resistance of as-cast Mg-10.16Li-8.14Al-1.46Er alloy was improved by different heat treatments.

According to the corrosion current density value substituted into formula (1) for calculation, the corrosion rate P_i (mm y^{-1}) of Mg-10.16Li-8.14Al-1.46Er alloy in different states was 2.86, 2.72, 1.80 and 1.37 mm y^{-1}, respectively. The corrosion current density measured by the polarization curve reflects the transient measurement. The actual corrosion rates of different Mg-Li alloys need to analyze in combination with long-term immersion corrosion tests.

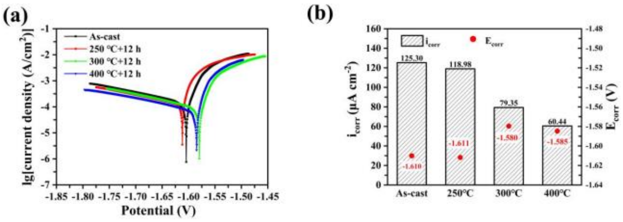

Figure 5 Polarization curves of the Mg-10.16Li-8.14Al-1.46Er alloy (a) and corrosion potential and current density (b)

Figure 6 is the immersion test results of Mg-10.16Li-8.14Al-1.46Er alloy. It can be seen from Figure 6a that the volume of hydrogen evolution of as-cast and at 300℃ samples was significantly higher than the other two heat treatment status samples at the initial stage. The hydrogen evolution of the samples at 400℃ was always lower until the immersion time of 45 h. The volume of hydrogen evolution of samples at 400℃ exceeds the samples at 250℃ after 45 h, then exceeds the samples at 300℃ after 63 h. The final volume of hydrogen evolution was as follows: as cast ＞ 400 ℃ ＞ 300℃ ＞ 250℃. This means that the corrosion resistance of the samples immersed in 3.5 wt. % NaCl solution for a long time after heat treatment at 400℃ was only higher than the as-cast alloy. The hydrogen evolution rate V_H (mm cm^{-2} d^{-1}) of Mg-10.16Li-8.14Al-1.46Er of as-cast, 250℃, 300℃ and 400 ℃ was 8.70, 4.35, 4.95 and 5.56 mm cm^{-2} d^{-1}, respectively. According to formula (2), the V_H converted to corrosion rate P_H (mm y^{-1}) and the hydrogen evolution corrosion rate was: 19.83, 9.91, 11.28 and 12.67 mm y^{-1}, respectively.

Figure 6b is the mass loss of Mg-10.16Li-8.14Al-1.46Er alloy. The mass loss of samples of as-cast, 250℃, 300℃ and 400℃ was 9.8, 3.5, 4.9 and 5.8 mg cm^{-2} d^{-1}, respectively. The corrosion rate of samples was as follows: as-cast ＞ 400℃ ＞ 300℃ ＞ 250℃. The results of hydrogen evolution test consistent with the results of mass loss test. According to formula (3), the corrosion rates P_W (mm y^{-1}) was 20.85, 7.35, 10.29 and 12.18 mm y^{-1}, respectively.

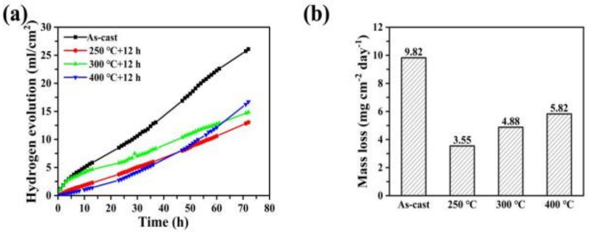

Figure 6 Hydrogen evolution curves (a) and mass loss (b) of the Mg-10.16Li-8.14Al-1.46Er alloy immersed in 3.5 wt. % NaCl solution for 72 h.

4 Discussion

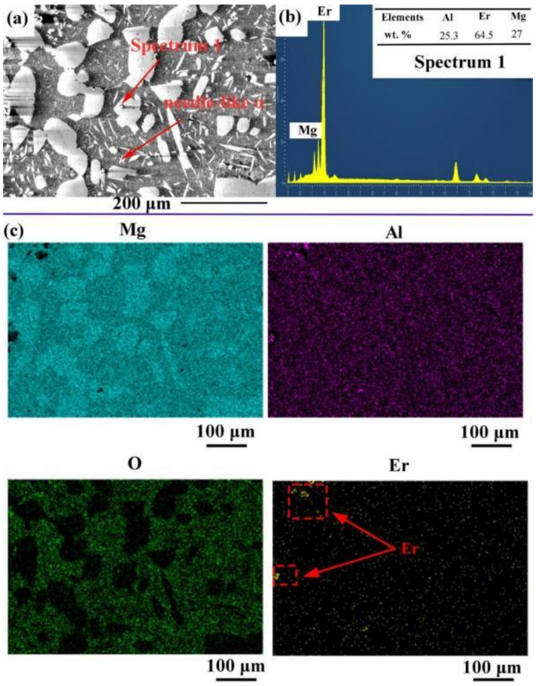

Figure 7 SEM and EDS of Mg-10.16Li-8.14Al-1.46Er alloy by heat treatment at 400℃. (a) microstructure. (b) point scan map. (c) surface scan map

The properties of the alloys are determined by the microstructure. Through the analysis of the observation results in Figure 1, the main phase of α was not obviously changed by heat treatment at the relatively lower temperature. This is due to there was no supersaturated solid solution formation, while no phase was precipitated during the water quenching. With the increase of temperature for 300℃, according to XRD analysis in Figure 2, AlLi phase was the main phase that disappeared and the $MgAlLi_2$ phase diffraction peak appears. $MgAlLi_2$ phase is a metastable phase and it is decomposed at 250℃, part of which is dissolved into α phase, and the other part is transformed into AlLi phase. With the increase of temperature to 300℃, supersaturated solid solution will be formed and $MgAlLi_2$ will precipitate again during water cooling. At 400℃, the diffraction peak of $MgAlLi_2$ phase is further strengthened. Moreover the α phase decreases obviously, while the α phase at GBs becomes larger than the α phase in matrix at 300℃. In order to further analyze the morphology distribution and elemental composition of α phase at 400℃, the SEM and energy spectrum analysis (EDS) was used to observe the microstructure at this temperature, and the results were shown in Figure 7. It can be seen from Figure 7a that bright white particles were distributed in the α phase, which is Al_3Er phase by point scanning element analysis in Figure 7b. This is further confirmed by the plane sweep diagram in Figure 7c, which the Er element was distributed on the α phase. The results show that the supersaturated solid solution was formed at higher temperature. During water quenching, part of α phases precipitates from the matrix phase and presents a fine needle-like distribution [27]. However, abnormal growth of α phase at the GBs may be related to the heterogeneous nucleation (such as Al_3Er). Changes of α phase and second phase caused by different heat treatments will result in different mechanical properties and corrosion resistance properties.

4.1 Analysis of tensile properties

The tensile properties of Mg-10.16Li-8.14Al-1.46Er alloy by different heat treatments were obviously different. Figure 8 is the SEM of tensile fractures of Mg-10.16Li-8.14Al-1.46Er alloy before and after different heat treatments. It can be seen on the fracture surface of Mg-10.16Li-8.14Al-1.46Er alloy in different states was not only composed of dimples, and there are still many cleavage planes on the surface. According to the tensile test results, the heat treatment temperature of 300℃ has the highest strength and the worst plasticity. It can be seen from Figure 8b and c that the dimples on the fracture surfaces of Mg-10.16Li-8.14Al-1.46Er alloy at 250℃ and 300℃ are small and shallow, but the cleavage plane of a hexagon appears on the surface of Mg-10.16Li-8.14Al-1.46Er alloy at 300℃, indicating that a poor plasticity. According to XRD results, strengthening phase of $MgAlLi_2$ appears in this state, and softened phase of AlLi is partially solute, which is also a reason for its plasticity deterioration. At the same time, bright white inclusions were found on the fracture surface of Mg-10.16Li-8.14Al-1.46Er alloy at 400℃ in Figure 8d. EDS results show that the atomic ratio of Er element to Al element is about 2.7. It means that bright white inclusion was Al_3Er phase. The above tensile test results show that the strength of Mg-10.16Li-8.14Al-1.46Er alloy at 400℃ was relatively higher, which the higher strength may be related to solid solution strengthening and second phase strengthening. Figure 9 is the optical microstructure of the fracture surface of Mg-10.16Li-8.14Al-1.46Er alloy before and after different heat treatments. The tensile test results show that Mg-10.16Li-8.14Al-1.46Er alloy at 400℃ has higher strength and the best plasticity, while the Mg-10.16Li-8.14Al-1.46Er alloy at 300 ℃ has the highest strength. According to the observation of microstructure on the fracture surface, there were bigger spheroidizing α phases distributed along the fracture surface in Figure 9d. As for duplex phases Mg-Li alloy, α phase can coordinate strength and β phase coordinate plastic. So the distribution of fewer but larger α phases increased the strength, and more β phases proportion improved the plasticity. However, the surface of the fracture shows a tearing zigzag shape at 300℃ in Figure 9c, which indicates that the fracture was sudden. The fracture plane passes through the α phase, and part of the α phases was torn. These torn α phases were rod-shaped, which contributing strong but decreasing plasticity. Morphology and distribution of α phase and the formation of intermetallic compounds are important factors affecting the mechanical properties of samples.

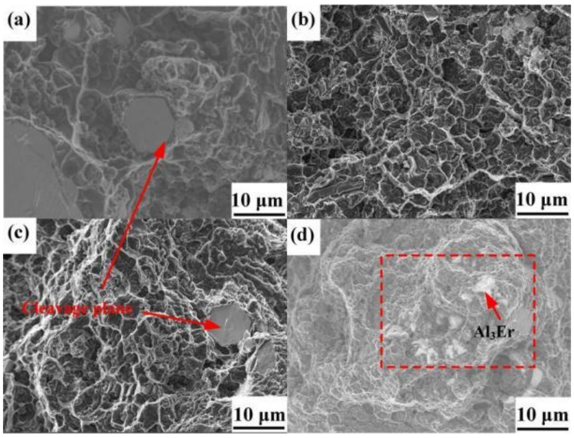

Figure 8 SEM of fracture surface of Mg-10.16Li-8.14Al-1.46Er alloy. (a) as-cast. (b) 250℃. (c) 300℃. (d) 400℃

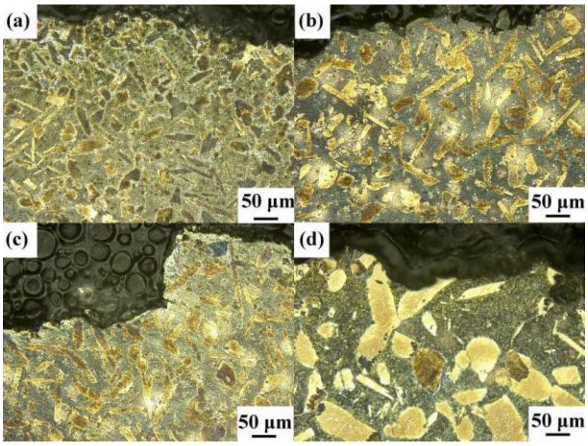

Figure 9 Optical microstructures of fracture surface of Mg-10.16Li-8.14Al-1.46Er alloy. (a) as-cast. (b) 250℃. (c) 300℃. (d) 400℃

4.2 Analysis of corrosion resistance properties

The results of three kinds of corrosion resistance tests show that the corrosion resistance of Mg-10.16Li-8.14Al-1.46Er alloy after heat treatments was improved compared with as-cast alloys. While the corrosion resistance of Mg-10.16Li-8.14Al-1.46Er alloy by different heat treatments was different. On the one hand, it is related to the type of corrosion products, on the other hand, it is related to the phase structure of Mg-Li alloy. Figure 10 is the surface morphology of Mg-10.16Li-8.14Al-1.46Er alloy before and after different heat treatments immersed in 3.5 wt. % NaCl solution for 72 h. According to the macroscopic corrosion morphology of Figure 10a,c,e,g, the corrosion surface of Mg-10.16Li-8.14Al-1.46Er alloy was distributed at corrosion pits. From microscopic corrosion morphology of Figure b,d,f,h, the corrosion not only corroded the β phase, but also corroded the α phase in a large area. The results show that pitting corrosion is the main corrosion type of different samples. This indicates that samples in different states have experienced serious corrosion during immersion. For Mg-Li alloy, the main protective film components are Li_2CO_3 and $MgCO_3$. However, with the progress of immersion test, corrosion occurs preferentially in the β phase, and the corrosion products are mainly $Mg(OH)_2$ and LiOH, which are porous and not protective, unable to resist the erosion of Cl^-. As corrosion progresses, the α phase is corroded. But compared with as-cast Mg-10.16Li-8.14Al-1.46Er alloy, heat treatment improves the corrosion resistance of Mg-10.16Li-8.14Al-1.46Er alloy. Figure 11 is the corrosion section morphology along the depth direction of Mg-10.16Li-8.14Al-1.46Er alloy before and after different heat treatments. Mg-10.16Li-8.14Al-1.46Er alloy is mainly composed of α and β phases, which is consistent with the microstructure analysis. The top of the section morphology is uneven in Figure 11a,c,d, which corrosion occurs on the surface and gradually corroded in the direction of depth after a long time immersion. According to Figure 1 and 2, the microstructure changes of Mg-10.16Li-8.14Al-1.46Er alloy at 300℃ lies in the refinement of α phase, $MgAlLi_2$ phase and AlLi phase. The refinement of α phase exposes more β phases to immersion corrosion medium, resulting in the outstanding hydrogen evolution of in the early stage of hydrogen evolution as showed in Figure 11c. Uniform corrosion in Figure 11b proves that the samples at 250℃ have the best corrosion resistance from the long time immersion. It can be seen from Figure 6a that the hydrogen evolution range of Mg-10.16Li-8.14Al-1.46Er alloy at 250 ℃ shows a relatively consistent linear change with time, which means that it has a good homogenization effect. While the polarization curve test combined with the preliminary analysis of hydrogen evolution test shows the best corrosion resistance in a short time at 400℃. At the same time, it is also found that no matter what the state of samples is, it preferentially corrodes the β phase when the corrosion occurs. With corrosion of β phase leads to falling off α phase. The best corrosion resistance in a short time at 400℃ due to inhibitory effect of α phase. The microstructure changes of Mg-10.16Li-8.14Al-1.46Er alloy at 400℃ not only on α phase but also the second phases. That is AlLi phase was solidly dissolved into the matrix and precipitation $MgAlLi_2$ phase. Immersing in the early stage of the samples at 400℃, corrosion resistant performance was outstanding due to the distribution of spheroidizing α phase and needle-like α phase. However, with the process of immersion, corrosion takes place preferentially in β phase. At the same time, AlLi phase distributed in α/β phase boundary plays the role of corrosion barrier [12-28]. But AlLi phase was solidly dissolved after heat treatment at 400℃, which means that its barrier effect disappears. Therefore, the β phase matrix corrosion is serious with the progress of corrosion, while the α phase loses protection. Then the volume of hydrogen evolution was increasing.

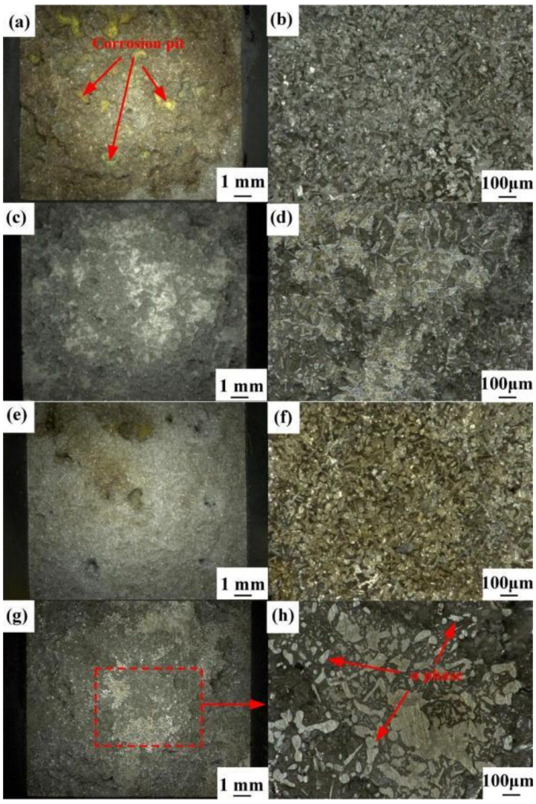

Figure 10 Surface morphology of Mg-10.16Li-8.14Al-1.46Er alloy immersed in 3.5 wt. % NaCl solution for 72 h. (a, b) as-cast. (b, c) 250℃. (e, f) 300℃. (g, h) 400℃

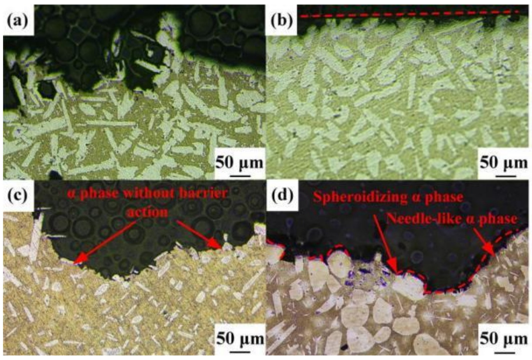

Figure 11 Section morphology of Mg-10.16Li-8.14Al-1.46Er alloy immersed in 3.5 wt. % NaCl solution for 72 h. (a) as-cast. (b) 250℃. (c) 300℃. (d) 400℃

5 Conclusions

The comprehensive mechanical and corrosion properties of Mg-10.16Li-8.14Al-1.46Er were investigated before and after heat treatments. The main conclusions are summarized as following:

(1) The microstructure of as-cast Mg-10.16Li-8.14Al-1.46Er includes α, β, $MgAlLi_2$, Al_3Er and AlLi. After heat treatments at different temperatures, the microstructure changes are the morphology and quantity of α phase, the second phases of $MgAlLi_2$ and AlLi.

(2) After heat treatments at different temperatures, the hardness and strength of Mg-10.16Li-8.14Al-1.46Er alloy were improved compared with the as-cast samples. At 400℃, Mg-10.16Li-8.14Al-1.46Er alloy has the best comprehensive mechanical properties due to its α phase structure, solution strengthening and second phase strengthening.

(3) After heat treatments at different temperatures, the corrosion resistance of Mg-10.16Li-8.14Al-1.46Er was improved compared with the as-cast samples. The Mg-10.16Li-8.14Al-1.46Er alloy has the best corrosion resistance at 250℃ due to the best homogenization at this temperature.

Author Contributions: Shuhao Liu: Investigation, Methodology, Data curation, Validation, Writing – original draft preparation. Xiaoyang Qian: Methodology, Validation, Visualization. Yun Zou: Methodology, Validation, Writing – review & editing, Supervision, Funding acquisition. All authors have read and agreed to the published version of the manuscript.

Conflict of Interest: The authors declare that there is no conflict of interest regarding the publication of this paper.

Acknowledgments: This research was funded by the National Natural Science Foundation of China (No. 51801185); Key Research Project of the Higher Education Institutions of Henan Province, Henan Provincial Department of Education, China (No. 19A460007); and Training Program for Young Backbone Teachers of the Higher Education Institutions of Henan Province, China. The authors would like to thank the experimental equipment support by Center of Advanced Analysis & Gene Sequencing, Zhengzhou University, China.

References

[1] Xu W Q, Birbilis N. A high-specific-strength and corrosion-resistant magnesium alloy. Nature 2015, 14: 1229–1235.

[2] Zhao J, Zhang J. Effect of Y content on microstructure and mechanical properties of as-cast Mg-8Li-3Al-2Zn alloy with duplex structure. Mater. Sci. Eng. A 2016, 650: 240–247.

[3] Mineta T, Sato H. Simultaneously improved mechanical properties and corrosion resistance of Mg-Li-Al alloy produced by severe plastic deformation. Mater. Sci. Eng. A 2018, 735: 418–422.

[4] Liu T, Yang Q. Stability of twins in Mg alloys – A short review. J. Magnes. Alloy. 2020, 8: 66–77.

[5] Pu Z, Yang S. Ultrafine-grained surface layer on Mg-Al-Zn alloy produced by cryogenic burnishing for enhanced corrosion resistance. Scr. Mater. 2011, 65: 520–523.

[6] Li R G, Li H R. Achieving exceptionally high strength in binary Mg-13Gd alloy by strong texture and substantial precipitates. Scr. Mater. 2021, 193: 142–146.

[7] Pugazhendhi B S, Kar A. Effect of aluminium on microstructure, mechanical property and texture evolution of dual phase Mg-8Li alloy in different processing conditions. Arch. Civ. Mech. Eng. 2018, 18: 1332–1344.

[8] He Y, Peng C. Effects of alloying elements on the microstructure and corrosion behavior of Mg-Li-Al-Y alloys. J. Alloys Compd. 2020, 834.

[9] Sun Y H, Wang R C. Corrosion behavior and surface treatment of superlight Mg-Li alloys. T. Nonferr. Metal. Soc. 2017, 27: 1455–1475.

[10] Guo J, Chang L L. Effect of Sn and Y addition on the microstructural evolution and mechanical properties of hot-extruded Mg-9Li-3Al alloy. Mater. Charact. 2019, 148: 35–42.

[11] Morishige T, Obata Y. Effect of Al composition on the corrosion resistance of Mg-14 mass% Li system alloy. Mater. Trans. 2016, 57: 1853–1856.

[12] Zou Y, Zhang L. Improvement of mechanical behaviors of a superlight Mg-Li base alloy by duplex phases and fine precipitates. J. Alloys Compd. 2018, 735: 2625–2633.

[13] Cao D, Wu L. Electrochemical behavior of Mg-Li, Mg-Li-Al and Mg-Li-Al-Ce in sodium chloride solution. J. Power Sources 2008, 177: 624–630.

[14] Sun Y, Wang R. Microstructure and corrosion behavior of as-extruded Mg-xLi-3Al-2Zn-0.2Zr alloys (x = 5, 8, 11 wt.%). Corros. Sci. 2020, 167.

[15] Sun Y, Wang R. Hot deformation behavior of Mg-8Li-3Al-2Zn-0.2Zr alloy based on constitutive analysis, dynamic recrystallization kinetics, and processing map. Mech. Mater. 2019, 131: 158–168.

[16] Cao F, Zhang J. Mechanical properties and microstructural evolution in a superlight Mg-6.4Li-3.6Zn-0.37Al-0.36Y alloy processed by multidirectional forging and rolling. Mater. Sci. Eng. A 2019, 760: 377–393.

[17] Ji H, Liu W. Influence of Er addition on microstructure and mechanical properties of as-cast Mg-10Li-5Zn alloy. Mater. Sci. Eng. A 2019, 739: 395–403.

[18] Wang G W, Song D. Developing improved mechanical property and corrosion resistance of Mg-9Li Alloy via solid-solution treatment. Metals 2019, 9.

[19] Li J, An J. Effects of solution heat treatment on the microstructure and hardness of Mg-5Li-3Al-2Zn-2Cu alloy. Mater. Sci. Eng. A 2010, 527: 7138–7142.

[20] Pradeep Kumar P, Raj Bharat A. Role of microstructure and secondary phase on corrosion behavior of heat treated AZ series magnesium alloys. Mater. Today 2019, 18: 175-181.

[21] Maurya R, Mittal D. Effect of heat-treatment on microstructure, mechanical and tribological properties of Mg-Li-Al based alloy. J. Mater. Res. Technol. 2020, 9: 4749–4762.

[22] Wang B, Xu K. Anisotropic corrosion behavior of hot-rolled Mg-8 wt.%Li alloy. J. Mater. Sci. Technol. 2020, 53: 102–111.

[23] Shi Z, Liu M. Measurement of the corrosion rate of magnesium alloys using Tafel extrapolation. Corros. Sci. 2010, 52: 579–588.

[24] Shi Z, Atrens A. An innovative specimen configuration for the study of Mg corrosion. Corros. Sci. 2011, 53: 226–246.

[25] Wu R, Zhang M. Microstructure, mechanical properties and aging behavior of Mg-5Li-3Al-2Zn-xAg. Mater. Sci. Eng. A 2009, 520: 36–39.

[26] Guo X, Wu R. Influences of solid solution parameters on the microstrucuture and hardness of Mg-9Li-6Al and Mg-9Li-6Al-2Y. Mater. Des. 2014, 53: 528-533.

[27] Kral M V, Muddle B C. Crystallography of the bcc/hcp transformation in a Mg-8Li alloy. Mater. Sci. Eng. A 2007, 460–461.

[28] Song G S, Staiger M. Some new characteristics of the strengthening phase in β-phase magnesium-lithium alloys containing aluminum and beryllium. Mater. Sci. Eng. A 2004, 371: 371–376.

Viser Technology Pte. Ltd.
Research and Application of Materials Science
DOI: 10.33142/rams.v3i2.6734

Research Article Open Access

Preparation and Electrochemical Performance of Si@void@NC Composite with a Tunable Nitrogen Doping Content in the Carbon Layer

Yuan QIN[1], Renzhong HUANG[2], Yan DONG[1], Liufen XIA[1], Haoran YU[1], Guodong JIANG[1*]

1 Hubei Collaborative Innovation Center for High-efficiency Utilization of Solar Energy, School of Materials and Chemical Engineering, Hubei University of Technology, Wuhan, 430068, China
2 Qingyuan Jiazhi New Materials Research Institute Co. Ltd., Qingyuan, 511517, China

***Corresponding Author:** Guodong JIANG, Hubei University of Technology, Wuhan, 430068, China, jianggd@hbut.edu.cn*

Abstract:
A strategy for the preparation nitrogen-doped carbon encapsulated Si nanocomposite with a void layer (Si@void@NC) is proposed, in which the nitrogen doping content in the carbon layer is tunable. Aniline and ortho-phenylenediamine are both selected as the nitrogen, carbon sources and co-polymerized on Si@SiO_2, in which SiO_2 is functionalized as a void template. SEM and TEM observation show that Si nanoparticles are encapsulated in a hollow and interconnected carbon cages with a thickness of less than 10 nm, which is inclined to agglomerate together to form larger particles in micrometer scale. The variation of mole ratio of aniline and ortho-phenylenediamine will enable the change of nitrogen doping level in the carbon layer and ranges from 3.2% to 8.4%. The nitrogen is doped into the carbon framework in the form of pyridinic, pyrrolic and graphitic nitrogen. Electrochemical tests indicate that the nitrogen content influences the SEI formation and the lithiation of Si nanoparticles. The potential for the decomposition of electrolyte to form SEI film and the alloying of Si-Li negatively shift when the nitrogen doping content is increased. Furthermore, the cycling performance of Si@void@NC is improved when raising the nitrogen content in the carbon. And the optimal nitrogen content is 7.5%, which is corresponding to the mole ratio of aniline to ortho-phenylenediamine is 5:5.

***Keywords:** Silicon anode; Nitrogen doping; Lithium-ion batteries*

1 Introduction

Lithium-ion batteries (LIBs) is one of the most promising energy storage devices for various applications such as portable electronics, electric vehicles, and grid scale energy storage. To satisfy the increasing demand for higher energy and power density, enormous effects have been devoted to explore advanced materials for LIBs. Among the various existing anode materials, silicon (Si), delivering the exceptional high specific capacity of 4200 $mAh \cdot g^{-1}$ (in the form of $Li_{4.4}Si$) is considered to be a promising alternative to commercial graphite (about 370 $mAh \cdot g^{-1}$) [1]. Furthermore, its other advantages, including high abundance in earth and low discharge potential (ca. 0.5 V versus Li^+/Li) also make it attractive anode materials for LIBs. Nevertheless, the commercial application of Si-based anode has been hindered by the huge volume expansion (＞300%), the instability of solid-electrolyte interphase (SEI) film on the Si surface and low electrical conductivity during the lithium ion insertion and extraction processes, which thus cause the degradation of the electrode and a rapid decay of the capacity. To overcome the issues, various strategies have been explored to prepare diverse structures, such as silicon nanotube, silicon nanowire, porous silicon, which enable the accommodation of the volume change [2]. Alternatively, modifying the Si nanoparticles with a carbon layer will contribute to the improvement of the performance of Si-based anode. This is because the carbon can enhance the conductivity of Si nanoparticles as well as prevent the direct contact of Si nanoparticle with the electrolyte. Particularly, it can partially alleviate the huge volume expansion [3]. Therefore, the structure and the composition of carbon will play different effects on the performance of Si nanoparticles. With regard to the further improvement of the electrical conductivity of the Si/C composites, heteroatom doping of carbon has emerged as an effective method. N, S, O and B have already been utilized as dopants to modify the electronic and crystalline structures of carbon, giving rise to the improvement of its electrochemical performance [4-8]. Among the various doping heteroatoms, nitrogen is

Received on October 22, 2021; Accepted on December 9, 2021

considered to be one of most attractive dopant in the carbon matrix, as its atomic size is comparable to that of carbon. Moreover, the high electronegativity as well as additional free electrons will contribute to the conduction band of carbon. It has been reported that the nitrogen atom incorporation increases the surface hydrophilicity of carbon-based electrodes to lithium ion, leading to the additional improvement to the capacity [9-11]. First principles calculations demonstrates that the pyridine-N and the graphite-N local structures in the carbon lattice account for the enhanced lithium storage capacity [9]. A variety of nitrogen-containing carbon sources could be chosen to achieve the nitrogen-doped carbon in Si/C composite anodes, for example, polyaniline [11-12], ethylenediamine [10] polypyrrole [13], polydopamine [14], benzenedinitrile [15], melamine [16], glucosamine[17], et al. However, using these nitrogen-containing carbon source, a certain nitrogen content in the carbon for the resulted Si/C composite is achieved. In particular, as we know, it is difficult to adjust the nitrogen content and the effect of nitrogen doping content on the electrochemical performance of Si/C composites is rarely reported.

Aniline and its derivatives are important industrial raw material used primarily for the synthesis of conducting polymer, pesticide, dye, plastic, rubber. ortho-phenylenediamine containing two amino groups will endow the derived carbon with higher nitrogen content than aniline-derived carbon. It is reported that aniline could be co-polymerized with ortho-pheneneyldiamine in a wide range mole ratio [18]. Herein, poly(ortho-phenylenediamine-co-aniline) is chosen as a nitrogen-containing carbon source for the preparation of nitrogen-doped carbon layer encapsulated silicon composites. In the composite, the nitrogen content in the carbon layer is adjustable by tuning the monomer mole ratio of aniline to ortho-phenylenediamine. The storage of lithium in the nitrogen content-tunable Si/N-doped C composites is evaluated. The results suggest a moderate level of nitrogen in the carbon layer is suitable and the prepared Si-based composites exhibit an optimal electrochemical performance.

2 Experimental Section

2.1 Materials

Nano silicon (powder, crystalline, 50-100 nm, 99%) was provide by Shanghai Chaowei Nanotechnology Co., Ltd. China. 3-aminopropyltriethoxysilane (APTES) and tetraethoxysilane (TEOS) were purchased from Shanghai Chem. Co., Ltd. Aniline (AN), ortho-phenylenediamine (oPD), ammonium peroxydisulfate (APS), and other reagents were purchased from Sinopharm Chemical Reagent Co., Ltd and were used without any purification. Deionized water was used throughout the experiments.

2.2 Synthesis of Si@void@NC composites

Simply, 0.25 g Si powder was ultrosonically dispersed into a mixture of water and alcohol (350 mL, water:alcohol (V:V)=1:4). After adding 4 mL $NH_3 \cdot H_2O$ (14.5mol/L), 0.4 mL of APTES and 3 g of TEOS were slowly dropwise added and were kept stirring for 12 h. The product was subjected to the centrigugation, washing and drying to get Si@SiO_2. To synthsize the copolymer-coated Si@SiO_2, 0.01 mol of mixed AN and oPD with a certain mole ratio was added into Si@SiO_2 dispersion containing 1 mol/L HCl. Then, 10 mL of 1.25 mol/L APS solution was slowly poured and the reaction was kept for 4 h. After washed and dried, Si@SiO_2@poly(aniline-co-ortho-phnylenediamine) composite (denoted by Si@SiO_2@Cp) was achieaved. Afterward, Si@SiO_2@Cp composite was subjected to the carbonization at 800 °C for 2 h in an Ar atomsphere with a ramping rate of 2 °C/min, then Si@SiO_2@nitrogen-doped carbon (Si@SiO_2@NC) composite was obtained. Finally, SiO_2 was ethced by 5 %(wt) HF solution to get Si@void@nitrogen-doped C composites, which was assigned to Si@void@NC. The nitrogen doping content in the carbon of Si@void@NC was tuned by changing the mole ratio of AN to oPD from 10:0, 8:2, 5:5 to 2:8, which were assigned to Si@void@NC-1, Si@void@NC-2, Si@void@NC-3 and Si@void@NC-4, respetively.

2.3 Characterizations

X-ray photoelectron spectroscopy (XPS) spectra were taken on VG Multilab 2000 photoelectron spectrometer. Attenuated total reflection Fourier transform infrared (FT-IR) spectra were collected on Thermo Scientific Nicolet iS 50 with the wavenumber of 4000-600 cm^{-1}. The phase structures were analyzed and identified by X-ray diffractometer (Empyrean B.V. Holland) with a Cu K_α radiation. The morphology and structure were observed on field emission scanning electron microscopy (Hitachi SU8010) and transmission electron microscopy (JOEL 2100F), respectively.

2.4 Cells assemble and electrochemical measurements

A homogeneous slurry consisting of active material, carbon black (Super P) and sodium carboxymethyl cellulose (CMC) with a weight ratio of 8:1:1 to was coated on Cu foil by doctor-blade method. After drying at 60°C in vacuum overnight, the Cu foil was punched into 12 mm diameter discs with an effective mass loading of 0.5-0.7 mg/cm^2. Then the two-electrode coin-type cells (CR2032) were assembled in an Ar-filled glovebox with Li metal foil as counter and reference electrode, 1 M $LiPF_6$ dissolved in the mixture of ethylene carbonate (EC), dimethyl carbonate (DMC) and diethyl carbonate (DEC) (1:1:1 in volume) as the electrolyte and Celgard 2300 membrane as the separator. The galvanostatic charge/discharge tests were carried out on Land CT2001A battery test system in a potential range of 0.01-1.5 V (vs. Li/Li^+). The capacity is calculated based on the mass of

Si@void@NC composite on the electrode. The cyclic voltammetry (CV) and electrochemical impedance spectroscopy (EIS) measurements were conducted on Zahner Zennium (Germany) electrochemical workstation. All the electrochemical measurements were conducted at room temperature.

3 Results and Discussion

The preparation procedure of Si@void@NC composites is schematically illustrated in Figure 1. Firstly, Si nanoparticles is modified by a SiO_2 coating through the hydrolysis of APTES and TEOS, which functions as a void templet between the carbon layer and Si nanoparticles. The addition of APTES favors the uniform cover of the copolymer due to the amino group. After the co-polymerization of AN and o-PD on SiO_2 coating and the carbonization at an inert atmosphere, SiO_2 coating is etched by HF solution. The molar ratio of AN to o-PD is changed to adjust the doping level of nitrogen atoms in the final Si@void@NC composites.

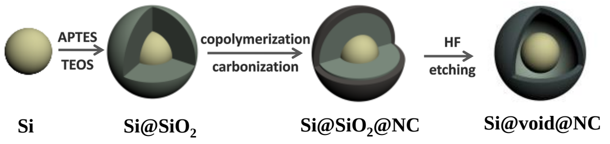

Figure 1 Schematic illustration of the preparation processes of Si@void@NC composites

The molecular structure of different samples is inverstigated to observe the evolution of Si nanoparticles by FT-IR spectroscopy. Figure 2(a). displays FT-IR spectra of samples acquired at the different steps during the preparation of Si@void@NC composites. The pristine Si nanopaticles show several adsorption peaks due to Si-O-Si stretching (1170 cm^{-1} and 1080 cm^{-1}) and bending vibrations (883 cm^{-1} and 830 cm^{-1}) [19]. Contrast to pristine Si nanoparticles, Si@SiO_2@Cp shows several strong absorption bands between 1700 cm^{-1} and 900 cm^{-1}. The peaks at 1537 cm^{-1} and 1486 cm^{-1} are the stretching vabration of the qiunoid and benzenoid rings in polyaniline [20], respectively. The band at 1631 cm^{-1} suggests the existence of oPD in the copolymer [21]. Most importantly, the occurrence of the bands at 1370 cm^{-1}, 1060 cm^{-1} and 892 cm^{-1} proves the phenzaine-like cyclic structure in the copolymer backbone [21-22], which could either be attributed to the presence of poly(ortho-phenylenediamine) blocks or the cyclic formation of the adjacent oPD and AN unit in the copolymeric chain, comfiring the copolymerization of AN and oPD. After the carbonization of Si@SiO_2@Cp in an inert atmosphere, the copolymer will be converted to the nitrogen doped carbon materials. Meamwhile, the typical absorption bands of the copolymer will vanish. It is found that the structure of the composite isn't damaged by HF acid etching besides the removal of SiO_2.

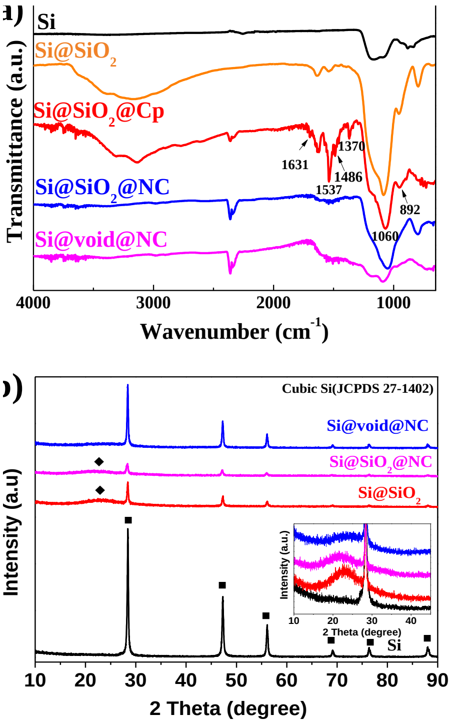

Figure 2 (a) FT-IR spectra and (b) XRD patterns of different samples. The inset in Figure b is the magnification in range of 10 to 45 degree. (■—Si, ◆—SiO_2)

The crystalline structure of different Si-based samples is futher investigated by X-ray diffraction spectroscopy (XRD), as shown in Figure 2(b). The pristine Si nanoparticles are crystalline and show several sharp diffraction peaks at 28.5°,47.3°, 56.1°, 69.0°, 76.3° and 88.0°, which can be indexed to (111), (220), (311), (400), (331) and (422) lattice planes of cubic Si (JCPDS NO. 27-1402), respectively. Once SiO_2 is deposited on the surface of Si nanoparticles, a broad and weak band centred at 23° is observed, which is due to the diffraction of amorphous SiO_2. While the copolymer of AN and oPD is formed and further converted to the nitrogen-doped carbon layer on SiO_2, there is no new peak observed in the diffraction pattern and the diffraction profile almost does not change besides the further decline in the diffraction strenghth. At the same time, the weak and broad peak near 23° still exsits. However, once treated by the HF etching, the diffraction corresponding SiO_2 is weakened and shifted to a higher angle. Additionally, the peak strenghth for Si nanoparticles drastically increases, implying SiO_2 layer is removed and the space between Si and nitrogen-doped carbon is created.

SEM images of pristine Si nanopartilces (Figure 3(a,b)) show that they are predominantly spherical in the shape with a diameter ranging from 50 nm to 100 nm. The modification of Si nanoparticles by SiO_2 results in a slight increase in the size. Meanwhile, some Si@SiO_2 particles aggregate together, as shown in Figure 3(c,d). In contrast, the remarkable change in the morphology and size for the Si@void@NC is observed in Figure 3(e,f).

The agglomeration of $Si@SiO_2@Cp$ during the surface polymerizaton and carbonization may acccount for the structure change for Si@void@NC.

The internal structure of Si@void@NC is investigated by TEM, as displayed in Figure 3(g, h). The agglomerated Si@void@NC is evident, which is in accordance with the results of SEM. It is noted that Si nanoparticles are successfully encapsulated inside the interconnected nitrogen-doped carbon cage.It is seen that the nitrogen-doped carbon cage is very thin and has a thickness of less than 10 nm. Additionally, a void between Si nanoparticle and the thin carbon layer is generated. The void place presented in Si-based composite nanoparticle will accommodate the expansion during the lithiation of Si and stabilize the electrode.

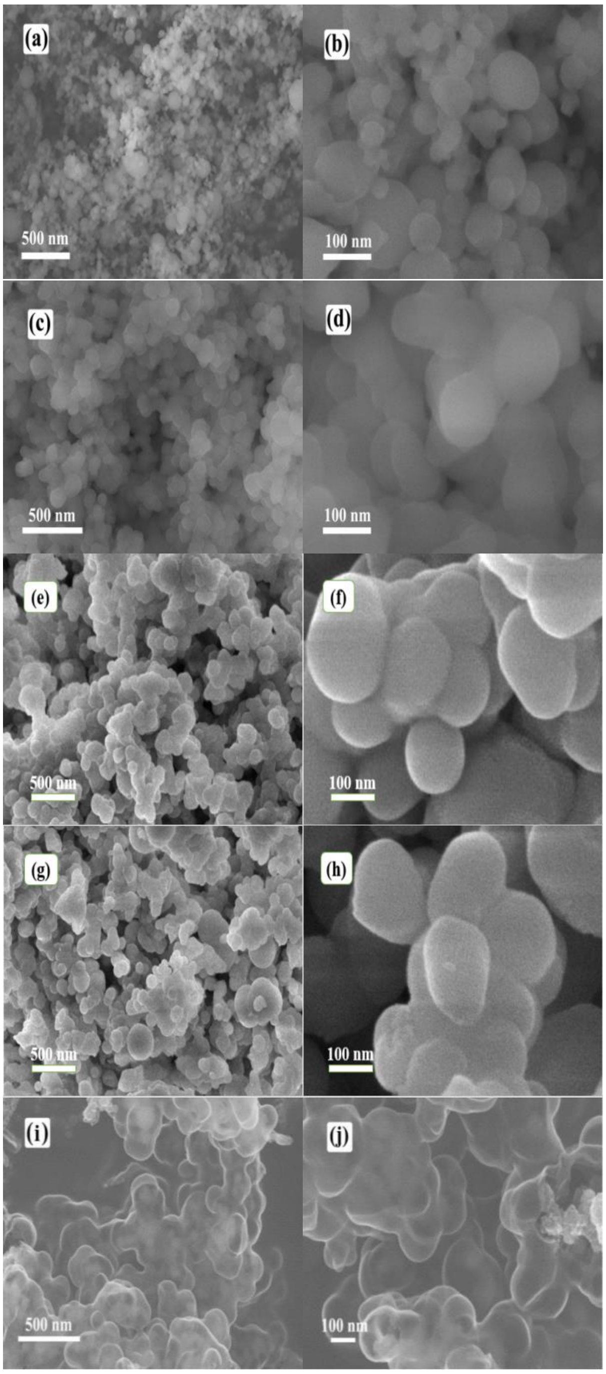

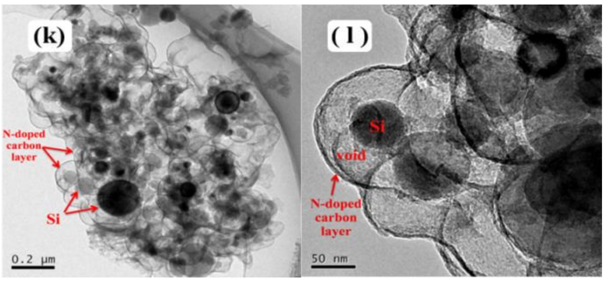

Figure 3 SEM (a-j) and TEM (k-l) images of (a, b) pristine Si, (c,d) $Si@SiO_2$,(e,f) $Si@SiO_2@Cp$, (g,h) $Si@SiO_2@NC$ and (i-l) Si@void@NC

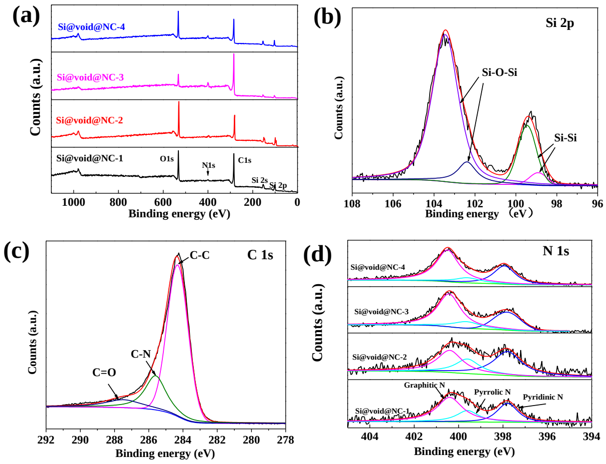

Figure 4 (a) XPS survey spectra of Si@void@NC samples and the high-resolution spectra of (b) Si 2p, (c) C 1s in Si@void@NC-3 and (d) N 1s in different Si@void@NC samples

Table 1 The relative nitrogen contents of Si@void@C in different ratio of An to OPD

Sample	Si@void@NC-1	Si@void@NC-2	Si@void@NC-3	Si@void@NC-4
Nitrogen content (vs. carbon)	3.2%	4.0%	7.5%	8.4%

Figure 4(a) shows the X-ray photoelectron spectroscopy (XPS) survey spectra of Si@void@NC samples. It is confirmed that both the carbon and nitrogen elements exist in all Si@void@NC samples, implying the nitrogen is doped into the carbon lattice. Moreover, the increase in the relative peak strength of nitrogen to carbon with the increase of the mole ratio of o-PD to AN suggests that the nitrogen level in the carbon layer gradually raises. According to the peak area of nitrogen and carbon, the relative atomic content of nitrogen in the carbon layer is calculated and the results are shown in Table 1. The nitrogen content of 3.2% is achieved while only AN is polymerized on $Si@SiO_2$. However, once AN is copolymerized with oPD, the nitrogen content is increased and the content is 4.0%, 7.5% and 8.4% for Si@void@NC-2, Si@void@NC-3, Si@void@NC-4, respectively. Accordingly, the nitrogen doping content in the carbon layer is readily tuned by the copolymerization of AN and o-PD. The chemical state of Si, C and N is studied by their corresponding fine XPS spectra. Figure 4(b) shows the Si 2p spectrum. The peaks with the binding energy of 98.9 eV and 99.5 eV are assigned to Si-Si bond, while the peaks centering at 102.3 eV and 103.1 eV are attributed to SiO_x owing to the sight oxidation of Si nanoparticles [13-23]. The C1s peak in Figure 4(c) consists of three sub-peaks located at 284.4 eV, 285.7 eV and 287.7 eV corresponding to C-C C-N and C=O, respectively. The existence of N-C bond is due to the substitution of N atoms, suggesting the successful N-doping into the carbon framework [10-17]. The N 1s high-resolution XPS spectrum can be deconvoluted into three peaks located at 397.8 eV, 399.7 eV and 400.4 eV, respectively, which are associated with the pyridinic, pyrrolic and graphitic nitrogen atoms doped into the carbon framework [12-17]. The nitrogen doping in the carbon layer is beneficial to achieve high electronic conductivity and provides additional lithium storage sites, boosting the performance of Si anode. Moreover, more oPD seems to cause a high content of graphitic and pyridinic nitrogen, which facilitates the lithium intercalation [9].

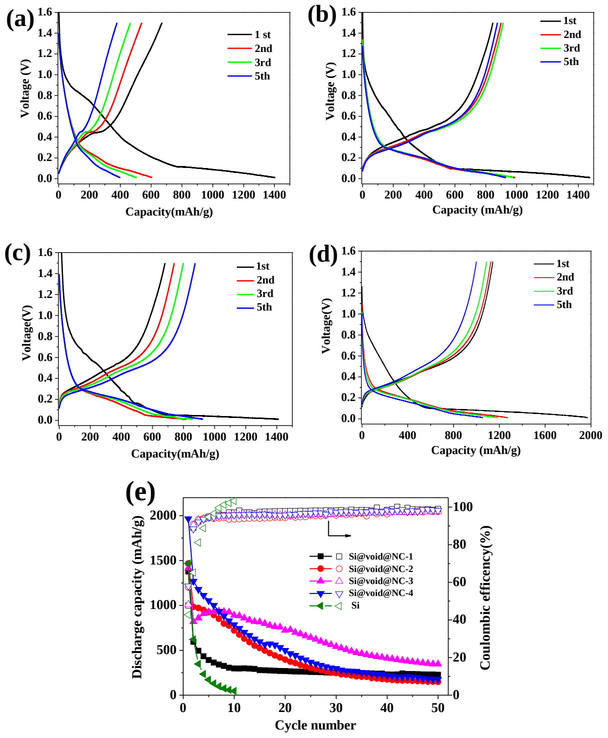

Figure 5 (a-d) The charge-discharge curves of the 1st-3rd, 5th cycles for (a) Si@void@NC-1, (b) Si@void@NC-2, (c) Si@void@NC-3 and (d) Si@void@NC-4 and (e) cycling perfance and coulombic efficency of Si and Si@void@NC at current density of 100 mA/g at a current density of 100 mA/g

The charge and discharge profiles of the four Si@void@NC samples for the 1st, 2nd, 3rd, 5th cycle at a current density of 100 mA/g are displayed in Figure 5. For all the samples, the similarity of their profiles in the first charge/discharge cycle demonstrates that the electrochemical reaction of lithium in these Si@void@NC composites has no distinct difference. A long slope plateau in the charge process from 1.0 to 0.20 V will vanish in the subsequent cycles, resulting in the irreversible consumption of lithium and the formation of the SEI film. The slope profile between 0.1 V and 0.01 V is considered to be the lithiation of Si. All the Si@void@NC samples deliver an initial discharge capacity of over 1400 mAh/g in the first cycle. The discharge capacity gradually decrease during the charge-discharge cycle. When the mole ratio of AN to o-PD is fixed at 5:5, the capacity fading is the slowest. It is noteworthy that a charge plateau is present near 0.4 V for Si@void@NC especially noticeable for the sample Si@void@NC. This is ascribed to the dealloying process of Si nanoparticles [24].

The cycling performance of Si@void@NC has been evaluated using galvanostatic charge-discharge measurements at a current density of 100 mA/g with the lower and upper cutoff voltages of 0.01 V and 1.5 V (Figure 5(e)). Si@void@NC-1 prepared only using polyaniline as carbon and nitrogen sources delivers an initial capacity of 1378 mAh/g, but rapidly reduces to 594 mAh/g for the second cycle. Subsequently, the discharge capacity decays and a low capacity of 227 mAh/g is remained at 50th cycle. However, with the increase of the concentration of o-PD during the polymerization, implying the increase of nitrogen doping content in the carbon layer, the capacity decay becomes slow. It is evident that Si@void@NC-3 manifests the best cycle stability and a capacity of 346 mAh/g is retained, suggesting too high nitrogen content in the carbon layer may deteriorate the performance of Si@void@NC. Besides, the coulombic efficiency of the four samples for the first cycle is about 47%-58%, and quickly reaches above 95%. Nevertheless, the results are not satisfactory in terms of the cycling stability. This may be due to the structure of Si@void@NC, which is needed to optimize further such as the void volume, the thickness of carbon layer.

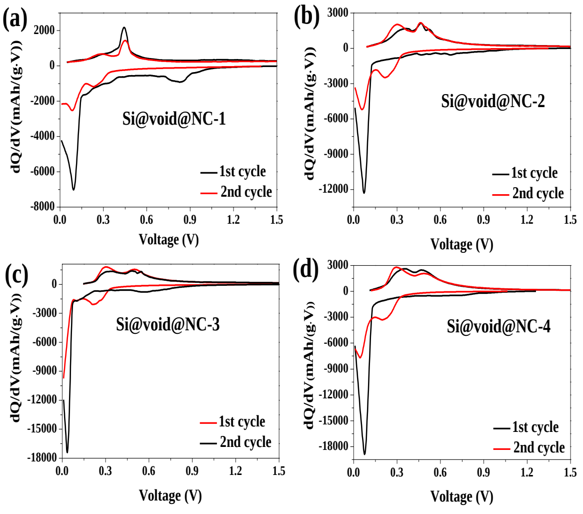

Figure 6 The differential capacity curves of (a) Si@void@NC-1, (b) Si@void@NC-2, (c) Si@void@NC-3 and (d) Si@void@NC-4

The electrochemical lithiation and delithiantion reaction of Si nanoparticles is able to be observed detailly in the differantial capacity curves (dQ/dV) [25]. Figure 6 displays the differential capacity curves of Si@void@NC samples for the first two cycle. During the discharge process, all the samples encounter the SEI formation (between 0.4V and 1.0V) and the lithiation (below 0.1 V). It is notewrothy that SEI formation and lithiation of Si nanoparticle require a lower potential, verified by left shift of the peaks corresponding to SEI formation and lithiation, when oPD is added. This is mightly caused by the increase of nitrogen content in the carbon layer. It is reported that Pyridinic and pyrrolic N species are more active because they can induce defects and edge sites in carbon material, favoring the diffusion and insert into the carbon [26]. In the research, higher oPD will introduce more nitrogen atom in the carbon layer. And there are three type of nitrogen species in the carbon layer, namely pyrrolic N and pyridinic N and graphitc N. As seen in figure 4(e), when nitrogen content in the carbon is increased, the ratio of graphtic N to pyrrolic N and pyridinic N raises. Therefore, low pyridinic and pyrrolic N will reduce the reaction actively of lithium ion, then a lower potential is required for the formation of SEI film. During the discharge, two peaks corresponding to the delithiation of Si-Li alloy are persent. In the second cycle, besides the reaction potential, there is not significatanly difference in the lithiaion and delithiation of amorphous Si converted in the first cycle, demonstating that the nitrogen doping level will affect the lithiantion and delithiation difficulty of Si nanoparticle. In terms of capacity fading during the cycle, the mole ratio of 5:5 for AN to o-PD is optimal.

4 Conclusion

A Si@void@NC nanocomposite with a tunable nitrogen content in the carbon layer is prepared. In the composite, a void between Si core and carbon layer is created through the etching of SiO_2 template. And AN and oPD is co-polymerized and utilized as nitrogen-containing carbon source, in which the mole ratio of AN and oPD can is varied to modulate the nitrogen doping level in the carbon layer. The characterization shows that Si@void@NC is inclined to agglomerate together to form larger particles in micrometer scale the copolymerization and carbonization, in which Si nanoparticles are encapsulated in a hollow and interconnected carbon cages with a thickness of less than 10 nm. It is found that the nitrogen content in the carbon layer varies from 3.2% to 8.4%. Moreover, the nitrogen doping into the carbon are present in the form of pyridinic, pyrrolic and graphitic nitrogen, regardless of its content in the carbon. Electrochemical tests indicate that the SEI formation and the lithiation of Si nanoparticles become difficult as the nitrogen doping content is raised. Additionally, the capacity fading is inhibited for Si@void@NC with a suitable nitrogen content. Compared to a capacity of 227 mAh/g for Si@void@NC-1 derived only from polyaniline, a capacity of 346 mAh/g is remained after 50 charge-discharge cycles for Si@void@NC-3 prepared with the mole ratio of 5:5 for AN and oPD. Nonetheless, the cycling stability is not satisfactory, which may be improved by the optimization of the preparation conditions and the structure of Si@void@NC.

Author Contributions: Y. Qin conducted the preparation and properties of the materials and wrote this manuscript; R. Huang and Y. Dong performed the characterization of the materials; L. Xia performed the data analysis; H. Yu contributed significantly to manuscript preparation; G. Jiang helped perform the analysis with constructive discussions and will be responsible for this article.

Conflict of Interest: The authors declare that there is no conflict of interest regarding the publication of this paper.

Acknowledgments: This work was supported by grants Hubei Province Technology Innovation Project (2018AAA056), Open Fund of Hubei Collaborative Innovation Center for High Efficient Utilization of Solar Energy (HBSKFZD2017006) and Innovative Research and Development Institute of Guangdong (No. 2018B090902009), Innovation and entrepreneurship training program for College Students (No.201710500024).

References

[1] Su X, Wu Q, Li J, et al. Silicon-based nanomaterials for lithium-ion batteries: a review. Adv Energy Mater 2014, 4: 1300882.

[2] Rahman M A, Song G, Bhatt A I, et al. Nanostructured silicon anodes for high-performance lithium-ion batteries. Adv Funct Mater 2016, 26: 647-678.

[3] Fang G, Deng X, Zou J, et al. Amorphous/ordered dual carbon coated silicon nanoparticles as anode to enhance cycle performance in lithium ion batteries. Electrochim Acta 2019, 295: 498-506.

[4] Chen L F, Huang Z H, Liang H W, et al. Three-dimensional heteroatom-doped carbon nanofiber networks derived from bacterial cellulose for supercapacitors. Adv Funct Mater 2014, 24: 5104-5111.

[5] Li Y J, Wang G L, Wei T, et al. Nitrogen and sulfur co-doped porous carbon nanosheets derived from willow catkin for supercapacitors. Nano Energy 2016, 19: 165-175.

[6] Qie L, Chen W M, Xiong X Q, et al. Sulfur-doped carbon with enlarged interlayer distance as a high-performance anode material for sodium-ion batteries. Advanced Science 2015, 2: 1500195.

[7] Liu X H, Zhang L Q, Zhong L, et al. Ultrafast ele° trochemical lithiation of individual si nanowire anodes. Nano Lett 2011, 11: 2251-2258.

[8] Paraknowitsch J P, Thomas A. Doping carbons beyond nitrogen: an overview of advanced heteroatom doped carbons with boron, sulphur and phosphorus for energy

applications. Energ Environ Sci 2013, 6: 2839-2855.

[9] Cho Y J, Kim H S, Im H, et al. Nitrogen-doped graphitic layers deposited on silicon nanowires for efficient lithium-ion battery anodes. J Phys Chem C 2011, 115: 9451-9457.

[10] Jeong M G, Islam M, Du H L, et al. Nitrogen-doped carbon coated porous silicon as high performance anode material for lithium-ion batteries. Electrochim Acta 2016, 209: 299-307.

[11] Tao H C, Huang M, Fan L Z, et al. Effect of nitrogen on the electrochemical performance of core–shell structured Si/C nanocomposites as anode materials for Li-ion batteries. Electrochim Acta 2013, 89: 394-399.

[12] Xu R, Wang G, Zhou T, et al. Rational design of Si@carbon with robust hierarchically porous custard-apple-like structure to boost lithium storage. Nano Energy 2017, 39: 253-261.

[13] Lu B, Ma B, Deng X, et al. Cornlike Ordered mesoporous silicon particles modified by nitrogen-doped carbon layer for the application of li-ion battery. ACS Appl Mater Interfaces 2017, 9: 32829-32839.

[14] Jung C H, Choi J, Kim W S, et al. A nanopore-embedded graphitic carbon shell on silicon anode for high performance lithium ion batteries. J Mate. Chem C 2018, 6: 8013-8020.

[15] Zhu J, Yang J, Xu Z, et al. Silicon anodes protected by a nitrogen-doped porous carbon shell for high-performance lithium-ion batteries. Nanoscale 2017, 9: 8871-8878.

[16] Mu T, Zuo P, Lou S, et al. A two-dimensional nitrogen-rich carbon/silicon composite as high performance anode material for lithium ion batteries. Chem Eng J 2018, 341: 37-46.

[17] Ji D, Wan Y, Yang Z, et al. Nitrogen-doped graphene enwrapped silicon nanoparticles with nitrogen-doped carbon shell: a novel nanocomposite for lithium-ion batteries. Electrochim Acta 2016, 192: 22-29.

[18] Roković M K, Jurišić A, Žic M, et al. Manipulation of polymer layer characteristics by electrochemical polymerization from mixtures of aniline and ortho-phenylenediamine monomers. J Appl Polym Sci 2009, 113: 427-436.

[19] Zhang L, Liu Y, Key B, et al. Silicon Nanoparticles: Stability in Aqueous Slurries and the Optimization of the Oxide Layer Thickness for Optimal Electrochemical Performance. ACS Appl Mater Interfaces 2017, 9: 32727-32736.

[20] Olmedo-Martínez J L, Farías-Mancilla B I, Vega-Rios A, et al. Poly(ortho-phenylenediamine-co-aniline) based copolymer with improved capacitance. J Power Sources 2017, 366: 233-240.

[21] Parsa A., Ab Ghani S. Electrocopolymerization of aniline and ortho-phenylenediamine via facile negative shift of polyaniline redox peaks. Polymer 2008, 49, 3702-3708.

[22] Zhang L, Yuan W, Yan Y. In situ UV–vis spectroeletrochemical studies on the copolymerization of o-phenylenediamine and o-methoxy aniline. Electrochim Acta 2013, 113: 218-228.

[23] Zhang Y C, You Y, Xin S, et al. Rice husk-derived hierarchical silicon/nitrogen-doped carbon/carbon nanotube spheres as low-cost and high-capacity anodes for lithium-ion batteries. Nano Energy 2016, 25: 120-127.

[24] Lin N, Zhou J, Wang L, et al. Polyaniline-assisted synthesis of Si@C/RGO as anode material for rechargeable lithium-ion batteries. ACS Appl Mater Interfaces 2015, 7: 409-414.

[25] Obrovac M N, Krause L J. Reversible cycling of crystalline silicon powder. J Electrochem Soc 2007, 154: A103-A108.

[26] Luan Y, Hu R, Fang Y, et al. Nitrogen and phosphorus dual-doped multilayer graphene as universal anode for full carbon-based lithium and potassium ion capacitors. Nano-Micro Letters, 2019, 11 (1): 30-31.

Publisher: Viser Technology Pte. Ltd.

URL: www.viserdata.com

Add.:21 Woodlands Close, #08-18,
Primz Bizhub SINGAPORE (737854)